uc3m | Universidad Carlos III de Madrid
Escuela Politécnica Superior

Stability of laminar jets and Clarke-Riley flames

Tesis Doctoral

Autor
Daniel Gómez Lendínez

Director
Wilfried Coenen

Co-Director
Alejandro Sevilla Santiago

Tutor
Alejandro Sevilla Santiago

DEPARTAMENTO DE INGENIERÍA TÉRMICA Y DE FLUIDOS

Leganés, Septiembre 2018

TESIS DOCTORAL

STABILITY OF LAMINAR JETS AND CLARKE-RILEY FLAMES

Autor: Daniel Gómez Lendínez

Director de Tesis: Wilfried Coenen

Co-Director: Alejandro Sevilla Santiago

Tutor: Alejandro Sevilla Santiago

Firma del Tribunal Calificador:

Firma

Presidente: Dr.

Vocal: Dr.

Secretario: Dr.

Suplente: Dr.

Calificación:

Leganés, 28 de Septiembre de 2018

DEPARTAMENTO DE INGENIERÍA TÉRMICA Y DE FLUIDOS
Escuela Politécnica Superior

Stability of laminar jets and Clarke-Riley flames

Autor
Daniel Gómez Lendínez

Director
Wilfried Coenen

Co-Director
Alejandro Sevilla Santiago

Tutor
Alejandro Sevilla Santiago

Leganés, Septiembre 2018

To those who support

"You can't say A is made of B
or vice versa.
All mass is interaction"

– Richard P. Feynman
Genius: The Life and Science of Richard Feynman,
by James Gleick, (1992).

Abstract

Open flows like jets and flames are sensitive to perturbations, and experience different instabilities. Submerged laminar axisymmetric jets with density sufficiently smaller than that of the ambient become globally unstable, exhibiting a self-sustained oscillatory behavior, when the Reynolds number is above a critical value that depends on the jet-to-ambient density ratio and on the outlet velocity profile. This phenomenon is analyzed in chapter 2 by direct numerical simulations of the unsteady axisymmetric equations of motion governing the velocity and density fields using the finite element method. It is shown that the unforced space-time propagation of non-linear disturbances defines two different asymptotic states that may be reached at large times: either a globally stable flow where the disturbances vanish, or a globally unstable state in which the jet oscillates with a characteristic intrinsic frequency. In the latter case, the numerical oscillation amplitudes are shown to fit the Stuart-Landau model for a supercritical Hopf bifurcation, and the corresponding neutral curve is in good agreement with experiments and linear stability theory.

Globally stable jets are noise amplifiers, in the sense that they usually respond to harmonic forcing by amplifying the forcing energy. If the energy gain of small disturbances is sufficiently large, the jet undergoes a transition from an asymptotically stable state to a convectively unstable state, where perturbations experience growth downstream of their spatial origin. This is the main topic of chapter 3, devoted to a global linear frequency response analysis of axisymmetric laminar jets for different Reynolds numbers, density ratios, outlet velocity profiles, and azimuthal modes. The study allows to define a critical Reynolds number, and to compute its value for each configuration, discussing its agreement with previous experimental and numerical results. The value of the critical Reynolds number obtained in the present analysis is affected by the geometry and the type of forcing. Thus, we consider both optimal and uniform forcing, and also vary the forcing region. In addition, we consider the effect of the injection geometry, considering that the jet emerges either from a circular injector tube far from any wall, or from a circular orifice on a wall.

Finally, the buoyancy-driven laminar flow associated with the Burke-Schumann diffusion flame that develops from the edge of a semi-infinite horizontal fuel surface, burning in a quiescent oxidizing atmosphere, has a self-similar steady structure. Chapter 4 considers fuels with non-unity Lewis numbers and gas mixtures with a realistic power-law dependence of the different transport properties. The problem is formulated in terms of chemistry-free Shvab-Zel'dovich variables that use linear combinations of the temperature and reactant mass fractions. The resulting self-similar solution is used as a base flow to perform a local stability analysis. A critical local Grashof number is found, above which the flame develops Görtler-like counter-rotating streamwise vortices. The analysis provides the dependence of the critical Grashof number on the relevant flame parameters.

Resumen

Los flujos abiertos, como los chorros y las llamas, son sensibles a las perturbaciones y están sujetos a diversas inestabilidades. Los chorros sumergidos con densidad menor que la del ambiente se vuelven globalmente inestables cuando el número de Reynolds supera cierto valor crítico que depende de la relación de densidad y de la forma del perfil de velocidad a la salida. Este fenómeno se analiza en el capítulo 2 mediante simulaciones numéricas directas de las ecuaciones de conservación que gobiernan los campos de velocidad y densidad, utilizando el método de elementos finitos. Se demuestra que la propagación de perturbaciones no lineales define dos estados posibles a tiempo largo: o bien el flujo es asintóticamente estable, o bien es globalmente inestable, lo que se manifiesta en la aparición de auto-oscilaciones con una frecuencia característica. En este último caso, las amplitudes de oscilación numéricas se ajustan al modelo de Stuart-Landau para bifurcaciones de Hopf supercríticas, y la curva neutra correspondiente muestra un buen acuerdo con los experimentos y la teoría de la estabilidad lineal.

Los chorros globalmente estables son amplificadores de ruido, dado que suelen responder al forzado armónico aumentando su energía. Si la ganancia de energía es suficientemente grande, tiene lugar una transición desde un estado asintóticamente estable a un estado convectivamente inestable, caracterizado por el crecimiento de las perturbaciones aguas abajo de su origen espacial. Este es el tema del capítulo 3, dedicado a un análisis de la respuesta global lineal en frecuencia para diferentes números de Reynolds, relaciones de densidad, perfiles de velocidad a la salida, y modos azimutales. El estudio permite definir un número de Reynolds crítico, y calcular su valor para cada configuración, comparando el resultado con observaciones experimentales y numéricas anteriores. El número de Reynolds crítico predicho se ve afectado por el tipo de forzado y por la geometría. Por tanto, se estudian tanto el forzado óptimo como el uniforme, y dos soportes espaciales distintos para la región de forzado. Además, se tienen en cuenta dos geometrías de inyección distintas, una correspondiente a un inyector alejado de paredes, y otra en la que el chorro emerge de un orificio circular en una pared.

Por último, en el capítulo 4 se estudia el flujo laminar inducido por la flotabilidad de una llama de difusión de Burke-Schumann que se desarrolla desde el borde de una superficie horizontal semi-infinita de combustible, y que se quema en una atmósfera oxidante en reposo, que posee una estructura estacionaria autosemejante. Se consideran combustibles con números de Lewis distintos de la unidad, y mezclas de gases con una dependencia realista de las propiedades de transporte con la temperatura. El problema se formula mediante las variables de Shvab-Zel'dovich, que hacen uso de combinaciones lineales de la temperatura y las fracciones másicas. La solución autosemejante se usa como flujo base para realizar un análisis de estabilidad local, que permite calcular un número de Grashof local crítico como función de los parámetros relevantes, por encima del cual se desarrollan vórtices tipo Görtler.

Contents

CHAPTER

ONE

Introduction

Contents

This chapter presents a brief overview of the kind of flows studied in this thesis, namely jets and buoyant diffusion flames, considering the basic aspects of their phenomenology and behavior. Moreover, several concepts about linear stability will be explained to provide the reader with a summary of the theoretical framework used in the thesis to analyze these flow configurations.

1.1 Jets

Submerged jets are open shear flows, like wakes or boundary layers. These flows are called open because fluid particles enter and leave the domain of interest, in contrast with other flows such as the Rayleigh-Benard or the Taylor-Couette configurations, which are thereby called closed, see the reviews from Chomaz (2005); Huerre & Monkewitz (1990). In particular, jets are injected into an ambient fluid and develop spatially along the streamwise direction, as can be observed in figure 1.1.

Liquid and gaseous jets are familiar flows in engineering applications, prominent examples being fuel injectors, flame burners and pipe flows discharging into reservoirs. In industry, it may be interesting either to maintain the laminar state or to trigger turbulent flow to intensify their mixing with the ambient. In a different context, plasma jets are under intense research for their use in space propulsion (Bhattacharyya & Gauvin, 1975; Matveev *et al.*, 2005). In nature, some maritime currents have jet character, and their modeling is useful in environmental studies and maritime transport efficiency (Doyle & Shapiro, 1999; Pickart *et al.*, 2003).

In most applications jets have high associated Reynold numbers, typically based on the jet density and viscosity, mean velocity and nozzle diameter, $Re = \rho_j U_m D/\mu_j$. In these cases, they display an overall structure like the one depicted in figure 1.1, taken from Crow & Champagne (1971). The image shows a Schlieren picture made visible with CO_2 at $Re = 18,700$. The flow can be divided into three regions downstream of the nozzle: a laminar region in the near field with thin annular shear layers subjected to the Kelvin-Helmholtz instability mechanism, a transition region where the vortical structures develop three-dimensional instabilities, finally leading to a fully developed turbulent region several diameters downstream of the injector.

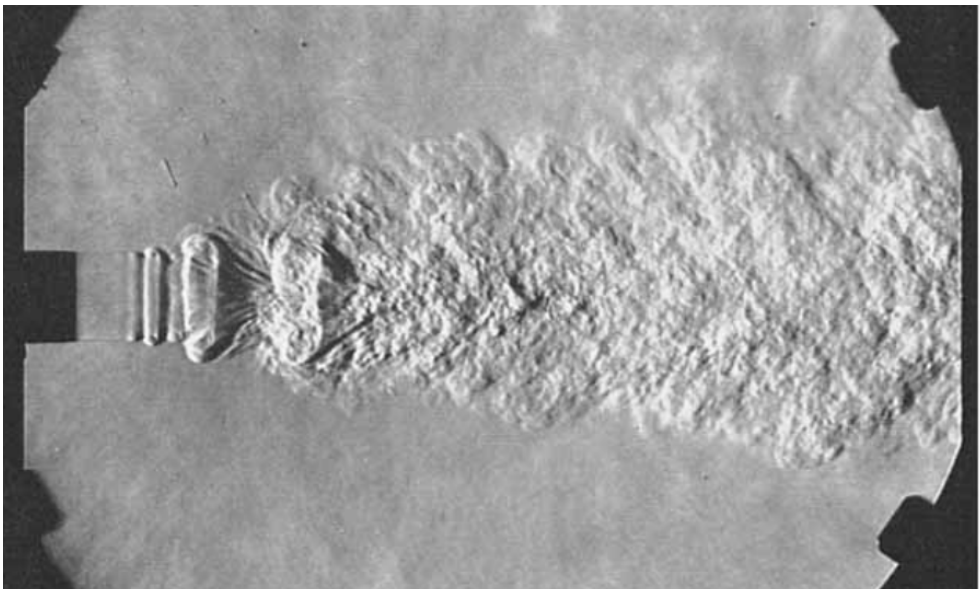

Figure 1.1: Schlieren picture of an air jet, made visible with $C0_2$ injection, at a Reynolds number $Re = 18,700$. Picture taken from Crow & Champagne (1971)

Jets are known to be very sensitive to external perturbations. Two different types of responses have been clearly distinguished in their receptivity. The first type of behavior corresponds to a noise amplifier with large gains within a certain frequency range, featuring a preferred frequency. This is the case of constant-density jets like the one shown in figure 1.1. Historically, Tyndall (1867) had already reported the high receptivity of jets to acoustic disturbances, acting as noise amplifiers. Sound is a prototypical example of external mechanical perturbation that disturbs jet flows. This noise amplifier behavior will be studied in chapter 3.

The second type of behavior consists in the development of self-sustained oscillations at a specific frequency, independent of external forcing for small enough forcing amplitudes. Monkewitz (1996) and Hallberg & Strykowski (2006) demonstrated that the

transition to the self-sustained state is associated with a Hopf bifurcation. This oscillatory behavior resembles the Von Karman vortex street in the wake behind two-dimensional bluff bodies, see for instance Provansal *et al.* (1987) where the existence of a global Hopf bifurcation was clearly shown. This self-excited behavior is observed in low-density jets when the jet-to-ambient density ratio is sufficiently small and the Reynolds number is sufficiently large. For example, figure 1.2(a) shows a Helium-air jet at a Reynolds number $Re = 775$ taken from Hallberg & Strykowski (2006) where we can observe a globally stable slender jet that remains laminar far from the nozzle, although some small-amplitude convective instability waves can be appreciated in the far field. The latter behavior is in marked contrast with figure 1.2(b) for Reynolds number $Re = 833$, where the jet displays a globally unstable state with strong synchronized oscillations close to the injector before it suddenly breaks down into a fully three-dimensional turbulent flow. The transition between these two types of behavior will be analyzed in chapter 2.

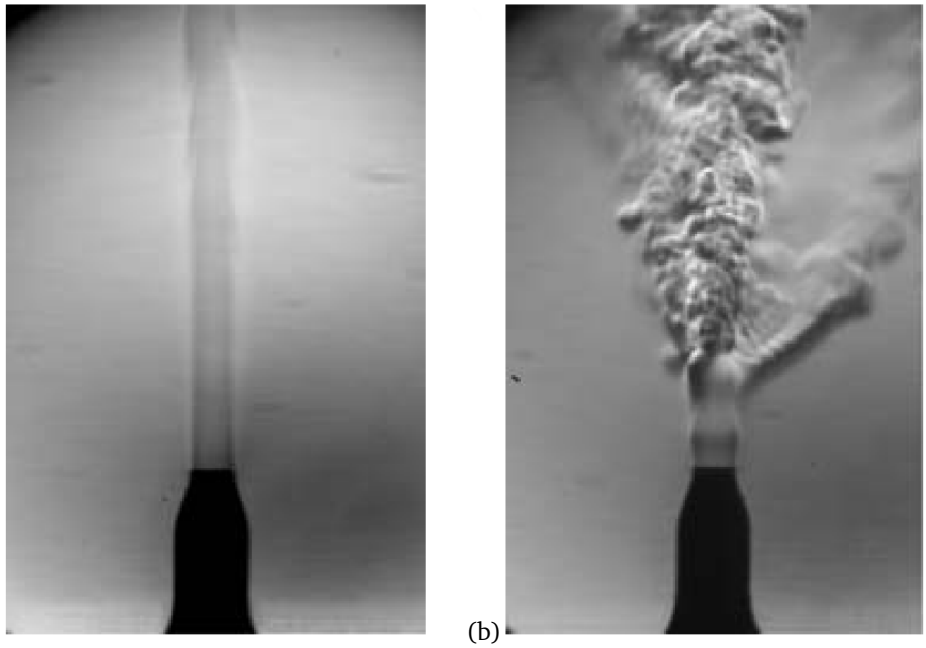

Figure 1.2: Low density jet (helium-nitrogen) experiments at global stable regime $Re = 775$ (a) and global unstable $Re = 833$ (b). Picture from Hallberg & Strykowski (2006)

1.2 Buoyant diffusion flames

Combustion is a phenomenon that has been important for human history. It is a source of energy that once controlled can be used from heating people to industrial applications. Flames are present in combustion chambers for energy production, heavy industry,

Figure 1.3: A fuel spread on a horizontal surface giving rise to a large pool fire. Near the edge "toe vortices" are present, i.e. vortical structures aligned with the radially inward direction of the flow. The buoyancy-driven boundary-layer flow near the edge of the fire and the appearance of these instabilities will be studied in chapter 4 of this dissertation. Picture from Miller *et al.* (2017).

engines, etc. or they may be present by accident due to forest fires or fuel spreading and burning. The first scientific studies on combustion date back to the work of Faraday (1861) in the 19th century.

Combustion is an exothermic reaction, which uses fuel, usually with a high content in carbon C and hydrogen H_2 atoms, and an oxidizer, usually oxygen O_2, to generate heat and products. Some of these products can have no impact to the environment, like water H_2O, but others, such as carbon dioxide CO_2 can contribute to global warming and climate change, or can directly be harmful to health: nitrogen oxides NO_x, sulfur oxides SO_x, etc. (see Gardiner (2000)). A good optimization of combustion processes is useful not only to industrial development, but can also prevent environmental and health issues due to the reduction of undesired products.

Reactive flows, i.e., flows undergoing combustion processes, are generally very prone to instabilities (see, for example, Matalon (2007) for an excellent review). These are often related to the large temperature gradients present near the flame front, the thin layer in which the reaction principally takes place. In diffusion flames such as non-premixed jet flames and pool fires, buoyancy often plays a major role in the appearance of instabilities.

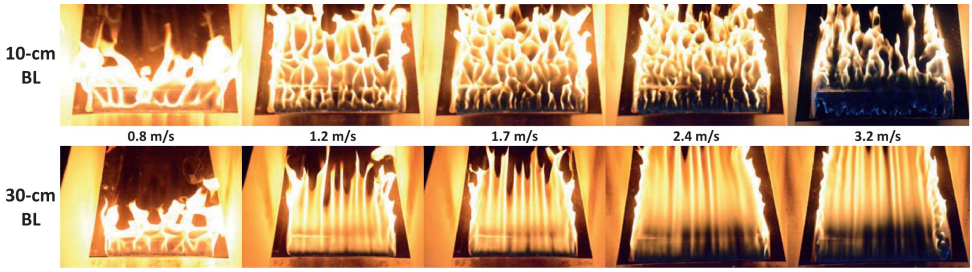

Figure 1.4: The interaction of a flame with a forced boundary layer, for varying wind speed and boundary layer thickness. Picture from Miller *et al.* (2017).

For example, it is the mechanism that causes the well-known "flickering" of a candle flame, or the "puffing" of a pool fire, which is a self-sustained oscillation of the entire flow field that periodically sheds large-scale vortical structures. Recently, the puffing of pool fires has been characterized and quantified as the onset of a global stability of the flow field (Moreno-Boza *et al.*, 2018).

Apart from undergoing a large-scale puffing behavior, pool fires and wild fires in general can exhibit a manifold of other instabilities. One of these is shown in the top view of a large pool fire in figure 1.3. Near the edge of the fire, we can observe finger-like vortical structures, often called "toe vortices" in the literature. These are in fact an instability of the buoyancy-driven boundary-layer flow that forms near the edge of the fire. In chapter 4 of this dissertation, we will study this boundary-layer flow—we name this flow the "Clarke-Riley diffusion flame", in honor of Clarke & Riley (1976), who gave the first formal description of its self-similar structure—and the appearance of instabilities of this type. Note that these instabilities are similar to those encountered in forced convection flows, such as the interaction of a flame with a forced boundary layer, shown in figure 1.4. Nevertheless, in this work only the naturally induced boundary-layer flow will be considered.

1.3 Instabilities

The linear stability of a given steady flow is usually quantified in terms of its response to infinitesimal disturbances. Typically, the perturbed flow is decomposed into a steady base flow plus small unsteady disturbances in the form of time-harmonic components $u = \widehat{u}(x)e^{i\omega t}$, where ω is an eigenvalue and $\widehat{u}$ its associated eigenfunction. This formulation is usually known as global linear stability analysis, see Theofilis (2011).

Linear global stability analysis was pioneered by Zebib (1987) and Jackson (1987), who studied the stability of the flow around bluff bodies such as spheres or cylinders. They were able to accurately compute the critical Reynolds number and the critical oscillation frequency associated with the first bifurcation experienced by the flow for increasing

Reynolds numbers. Thanks to the increase of computational power, together with the development of new numerical techniques, the use of the global linear stability analysis has steadily increased during the last three decades, see Theofilis (2011). It is also interesting to take into account previous reviews of Huerre & Monkewitz (1990), who established the link between local and global instabilities in slender spatially developing flows, and Chomaz (2005), who analyzed the role of non-normality and non-linearity in the development of global instabilities in both slender and non-slender spatially developing flows.

A particularly relevant class of flows are those which have a slender structure with a dominant velocity component. This is the case of many large Reynolds number flows of boundary-layer character. At leading order, these flows can be considered as parallel, thereby simplifying the mathematical analysis of their linear stability properties. This quasi-parallel approach is also known as local linear stability analysis, valid only when the disturbance wavelength is much smaller than the development length of the steady base flow. In the context of local stability analysis, two types of base flow can be distinguished according to their response to an impulsive forcing localized in space. A given locally parallel base flow is convectively unstable if the unstable response to the localized perturbation is swept away from the source. On the other hand, in an absolutely unstable flow perturbations grow both upstream and downstream from their source, thereby contaminating the whole spatial domain. A detailed description of these two kinds of instabilities can be found in Huerre & Monkewitz (1990), and their main features are illustrated in figure 1.5, which shows the differences between (a) stable, (b) convectively unstable and (c) absolutely unstable flows.

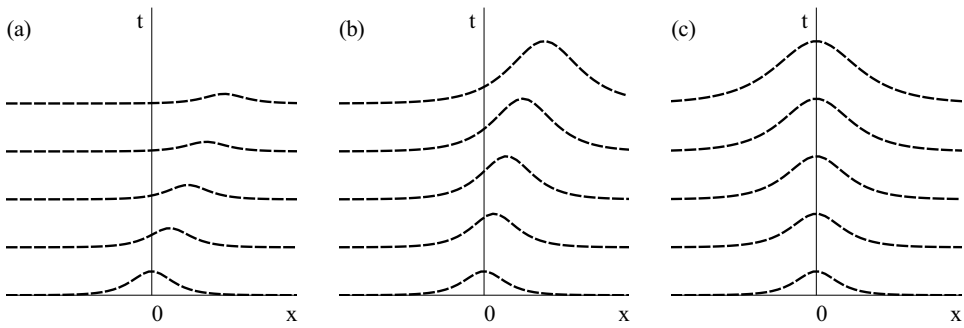

Figure 1.5: Impulse response of a parallel flow in space and time: (a) Stable flow, (b) Convectively unstable flow, (c) Absolutely unstable flow. Based on Huerre & Monkewitz (1990).

Convective instabilities usually rise to noise amplifiers, while absolute instabilities typically lead to globally synchronized and self-sustained oscillatory states. In the local framework, when the frequency ω is defined as a complex number $\omega = \omega_r + i\omega_i$ and it is considered as a function of the real wavenumber k, the analysis is known as temporal.

In this case, there is a functional relationship of the form $\omega(k, P)$ being P a set of flow parameters such as the Reynolds, Prandtl or Schmidt numbers. Periodic perturbations travel with phase velocity $c_r = \omega_r/k$ and their growth rate is ω_i. If $\omega_i > 0$ for some k the flow is linearly unstable, while if $\omega_i < 0$ for all k, all temporal modes are soften and the base flow is linearly stable, which corresponds to figure 1.5(a). If the flow is linearly unstable but the instability waves travel away from their source, the flow is convectively unstable, as depicted in figure 1.5(b). In contrast, if the instability waves grow both downstream and upstream of their spatial origin, the flow if absolutely unstable, as represented in figure 1.5(c).

In convectively unstable open shear flows that act as noise amplifiers, the flow responds to different frequencies. It is then more convenient to perform a spatial stability analysis in which the wavenumber is complex, $k = k_r + ik_i$, and depends on the real frequency and other flow parameters, $k(\omega, P)$.

For spatial instability, we only take the real component of frequency and calculate complex eigenvalues of $k = k_r + ik_i$ developing downstream along the space exponentially except for when the imaginary part is null $k_i = 0$ and it oscillates at $2\pi/k_r$. (see Drazin & Reid (2004)). For a complex frequency ω such that $\omega_i > 0$, some values of k_r will lead to the instability increase when time $t \to \infty$ driven to an unstable flow.

Spatial modes are not convenient for stationary instability, such as Bénard convection or Couette flow instabilities. On contrary, they are adequate for parallel flows where unstable disturbances propagates downstream while they grow. They are considered to emerge as long time solution of a linearized initial value problem.

In chapter 3 the submerged laminar jet configuration is studied using a global linear stability analysis, while in chapter 4 a local temporal approach has been adopted to compute the stability of the Clarke-Riley flame.

1.4 Outline of the dissertation

The present document is organized as follows:

Chapter 2 presents direct numerical simulations of low-density laminar submerged jets emerging from round injectors, with the aim at shedding light on the differences between previous experimental results and global linear stability analyses.

Chapter 3 is devoted to develop a novel approach for the computation of the critical Reynolds number of submerged laminar axisymmetric jets based on a global linear frequency response analysis. The analysis contemplates not only the axisymmetric modes with $m = 0$, but also the helical modes with $m = \pm 1$ and $m = \pm 2$, as well as a systematic comparison between optimal linear gains with those associated with uniform forcing inside the injection pipe. In the proposed approach, jets are stable if the kinetic energy gain is smaller than one, while they are unstable when the gain is larger than one. The

basic jet configuration is the same as that considered in chapter 2. The spatial distribution of the response is also presented and discussed although, to facilitate the reading, several results are shown in appendices B and C. This chapter also contemplates the influence of the geometry and the forcing region, through comparisons between wall-exit and injector geometries, and changing the spatial support of the forcing, either restricted inside the pipe, or including also an outside area.

Chapter 4 reports a theoretical and numerical study of the steady structure and local stability of Clarke-Riley flames, where fuel is burned above a planar surface. In particular, a critical Grashof number for the onset of instability is computed.

Finally, chapter 5 is dedicated to report the overall conclusions, and to point out several research directions for future work.

References

BHATTACHARYYA, D & GAUVIN, WH 1975 Modeling of heterogeneous systems in a plasma jet reactor. *AIChE Journal* **21** (5), 879–885.

CHOMAZ, JEAN-MARC 2005 Global instabilities in spatially developing flows: Non-Normality and Nonlinearity. *Annual Review of Fluid Mechanics* **37** (1), 357–392.

CLARKE, J. F. & RILEY, N. 1976 Free convection and the burning of a horizontal fuel surface. *Journal of Fluid Mechanics* **74** (3), 415–431.

CROW, S. C. & CHAMPAGNE, F. H. 1971 Orderly structure in jet turbulence. *Journal of Fluid Mechanics* **48** (3), 547–591.

DOYLE, JAMES D & SHAPIRO, MELVYN A 1999 Flow response to large-scale topography: The greenland tip jet. *Tellus A: Dynamic Meteorology and Oceanography* **51** (5), 728–748.

DRAZIN, PHILIP G & REID, WILLIAM HILL 2004 *Hydrodynamic stability*. Cambridge university press.

FARADAY, MICHAEL 1861 The Chemical History of a Candle. *A course of lectures delivered before a juvenile audience at the Royal Institution* pp. 194–196.

GARDINER, WILLIAM CECIL 2000 *Gas-phase combustion chemistry*. Springer New York.

HALLBERG, M. P. & STRYKOWSKI, P. J. 2006 On the universality of global modes in low-density axisymmetric jets. *J. Fluid Mech.* **569**, 493–507.

HUERRE, P. & MONKEWITZ, P. A. 1990 Local and global instabilities in spatially developing flows. *Annu. Rev. Fluid Mech.* **22**, 473–537.

JACKSON, C. P. 1987 A finite-element study of the onset of vortex shedding in flow past variously shaped bodies. *Journal of Fluid Mechanics* **182**, 23–45.

MATALON, MOSHE 2007 Intrinsic Flame Instabilities in Premixed and Nonpremixed Combustion. *Annual Review of Fluid Mechanics* **39** (1), 163–191.

MATVEEV, IGOR, MATVEEVA, SVETLANA & GUTSOL, ALEXANDER 2005 Non-equilibrium plasma igniters and pilots for aerospace application. In *43rd AIAA Aerospace Sciences Meeting and Exhibit*, p. 1191.

MILLER, COLIN H., TANG, WEI, FINNEY, MARK A., MCALLISTER, SARA S., FORTHOFER, JASON M. & GOLLNER, MICHAEL J. 2017 An investigation of coherent structures in laminar boundary layer flames. *Combustion and Flame* **181**, 123–135.

MONKEWITZ, PETER A. 1996 Modeling of self-excited wake oscillations by amplitude equationsz. *Experimental Thermal and Fluid Science* **12** (2), 175–183.

MORENO-BOZA, DANIEL, COENEN, WILFRIED, CARPIO, JAIME, SÁNCHEZ, ANTONIO L. & WILLIAMS, FORMAN A. 2018 On the critical conditions for pool-fire puffing. *Combustion and Flame* **192**, 426 – 438.

PICKART, ROBERT S, SPALL, MICHAEL A, RIBERGAARD, MADS HVID, MOORE, GWK & MILLIFF, RALPH F 2003 Deep convection in the irminger sea forced by the greenland tip jet. *Nature* **424** (6945), 152.

PROVANSAL, M, MATHIS, C & BOYER, L 1987 Bénard-von kármán instability: transient and forced regimes. *Journal of Fluid Mechanics* **182**, 1–22.

THEOFILIS, VASSILIOS 2011 Global Linear Instability. *Annual Review of Fluid Mechanics* **43** (1), 319–352.

TYNDALL, F.R.S. 1867 On the action of sonorous vibrations on gaseous and liquid jets. *The London, Edinburgh, and Dublin Philosophical Magazine and Journal of Science* **33** (224), 375–391.

ZEBIB, A. 1987 Stability of viscous flow past a circular cylinder. *Journal of Engineering Mathematics* **21** (2), 155–165.

CHAPTER

TWO

Direct numerical simulation of laminar axisymmetric low-density jets

Contents

This chapter presents a numerical study by Direct Numerical Simulations (DNS) of low-density laminar axisymmetric jets emerging from an injector into a quiescent ambient. In particular, we are concerned with the determination of the critical conditions for the onset of the well-known self-sustained oscillations that characterize these jets, which are a manifestation of an underlying Hopf bifurcation to a globally unstable flow. Our study aims to clarify the discrepancies between experimental observations (Hallberg & Strykowski, 2006) and recent predictions of local and global linear stability theory (Coenen *et al.*, 2017; Coenen & Sevilla, 2012).

To this end, the time dependent non-linear Navier-Stokes equations have been solved using a steady solution as the initial condition. For the numerical integrations, the finite element solver `FreeFEM++` (Hecht, 2012) has been used. Attention is focused on self-sustained axisymmetric perturbations, since these have been shown to prevail in experiments. The study of helical perturbations is postponed to chapter 3 in the context of harmonic forcing.

The chapter starts with a brief literature review, highlighting the key findings that motivate this work. Next, we present the mathematical formulation of the problem, followed by the numerical method employed to solve the equations of motion. Inside this section, steady and unsteady calculations will be explained separately. We proceed with a discussion of the results, before finally presenting conclusions and future developments.

2.1 Introduction

Jets have a broad range of applications in industry (such as fuel injectors, flame burners, plasma jets, and microfluidic applications), and environmental physics (such as maritime currents). Jets, as well as wakes, mixing layers and boundary-layer flows are know as open shear flows, in the sense that fluid particles can freely enter and leave the fluid domain, and that regions of strong shear are present in the flow. These flows are known to be very sensitive to disturbances. In that regard, their behavior can be classified to be of either of the following two types. First, they can act as *noise amplifiers*, amplifying incoming ambient fluctuations, typically exhibiting large amplification gains in a broad band around a certain preferred frequency. This is for example the case of high-Reynolds-number jets of constant density.

The second type of behavior that is possible in free shear flows is that in which the entire flow field undergoes coherent *self-sustained oscillations*, which are independent of low-amplitude external forcing, and which result in intrinsic flow dynamics characterized by a single oscillation frequency. Such behavior typically sets in when a certain control parameter exceeds a certain critical value. This is for example the case of the well-known Von Karman vortex street in the wake behind a cylinder when the Reynolds number based on the diameter exceeds the critical value of 46 (Bénard, 1908; Von Karman, 1908). It can also be the case for the low-density jets under consideration in this chapter when the density-ratio is sufficiently low and the Reynolds number is sufficiently high, as shown in the experiments of Hallberg & Strykowski (2006).

The oldest studies related to jet oscillations date back to the *XIX* century. Leconte (1858), and later Tyndall (1867) investigated the response of a flame when it is subjected to sound perturbations in the form of music. Since then, numerous authors have worked on improving our understanding of the dynamics of these flows.

Batchelor & Gill (1962) presented a mathematical analysis of the local inviscid stability of steady, incompressible, constant-density jets. Uniform velocity profiles were found to be unstable for any kind of perturbations, while smooth velocity profiles corresponding to a developed jet are unstable only for non-axisymmetric (helical) perturbations, in particular for the instability mode $|m| = 1$.

Spatial and temporal stability were studied by Lessen & Singh (1973) both for viscid and inviscid flows, including jets and wakes at their self-similar regions at low Reynolds numbers. Michalke (1970) found that round jets of smaller density than their surroundings show an anomalous behavior in their spatial stability properties. In particular, he found that spatial theory cannot be applied if the density ratio S decreases below a certain critical value S_c. This behavior was later explained as a consequence of the transition from convective to absolute instability (Monkewitz & Sohn, 1988). For incompressible and inviscid jets with uniform velocity profile, Huerre & Monkewitz (1990) showed that $S_c \approx 0.66$.

Monkewitz & Sohn (1988) considered the stability of hot round jets at high Reynolds number. These authors studied the effects of the Mach number and of the velocity ratio between the jet and an outer co-flow, using a parametric representation of the turbulent mean flow as base flow, adapted to fit the experimental data of Brown & Roshko (1974). For small Mach numbers and without outer co-flow, Monkewitz & Sohn (1988) found a critical density ratio $S_c \approx 0.72$ below which a region of absolute instability took place near the injector outlet. This prediction was experimentally checked by Monkewitz *et al.* (1990) for hot round jets.

In the case of top-hat profiles, the axisymmetric mode ($m = 0$) dominates the onset of absolute instability, in the sense that it has the largest associated density ratio, S. Indeed, other azimuthal modes ($m \neq 0$) only become absolute unstable for values of S substantially smaller (Monkewitz & Sohn, 1988). For instance, in the particular case of an inviscid jet with uniform velocity profile, the axisymmetric mode $m = 0$ has a critical density ratio $S_c \approx 0.66$ while the transition occurs at $S_c \approx 0.35$ for $m = \pm 1$.

In an important experimental work, Hallberg & Strykowski (2006) were able to independently modify the jet Reynolds number and the momentum thickness of the outlet velocity profile by means of nozzle extensions with different lengths, allowing them to obtain precise boundaries for the onset of global instability in helium-air jets. Shortly afterwards, Lesshafft & Huerre (2007) performed direct numerical simulations of synthetic jets that used hyperbolic tangent velocity profiles as inlet boundary conditions. The physical origin of the self-excited oscillations was investigated by Lesshafft *et al.* (2007), who concluded that the phenomenon is due to the baroclinic torque acting in the jet's annular mixing layer.

In the context of local stability theory, the works of Lesshafft *et al.* (2006), Coenen *et al.* (2008), Lesshafft & Marquet (2010) and Coenen & Sevilla (2012) studied the origin of the phenomenon with increasing detail, concluding that the presence of absolutely unstable regions in the near field of low-density jets are indeed responsible for the onset of global self-sustained oscillations.

The global linear stability analysis of submerged jets was pioneered by Nichols & Lele (2010) in a compressible setting. Later on, Garnaud *et al.* (2013) analyzed the global linear stability of incompressible constant density jets using a turbulent mean flow based on Monkewitz & Sohn (1988). This work was continued by Coenen *et al.* (2017), who studied the particular case of light jets, including the influence of the spreading rate and the domain length on the global modes of the jet. Recently, Qadri & Schmid (2017) considered the influence of weak nonlinearities on the global frequency response of axisymmetric and non-axisymmetric disturbances.

The objective of the present chapter is to analyze the fully nonlinear dynamics of axisymmetric light jets by means of direct numerical simulations in the laminar regime. In particular, the characteristic oscillation frequency and the critical Reynolds number will be compared with published data obtained both experimentally and with modal stability analysis. Indeed, there is a systematic difference between the critical Reynolds

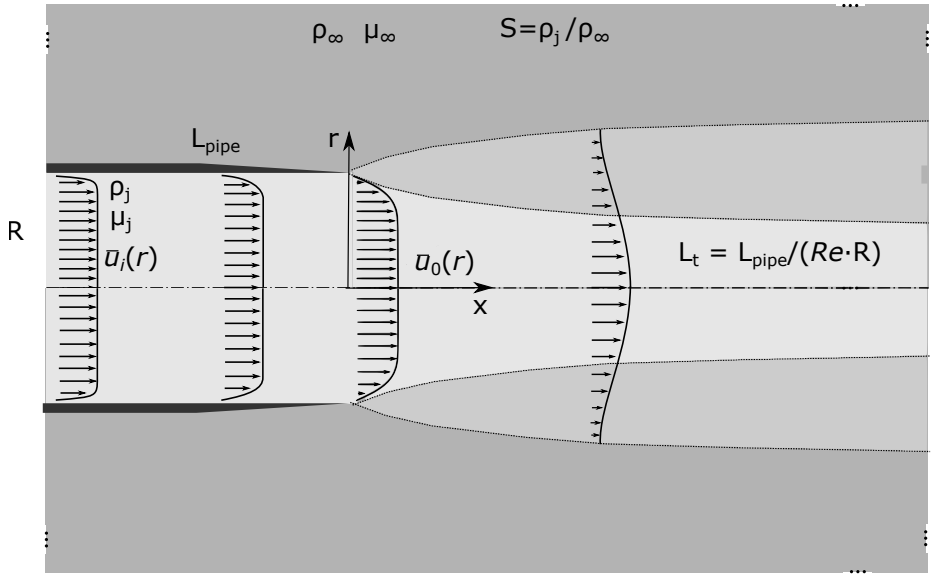

Figure 2.1: Schematic diagram of the flow configuration. Evolution of the velocity profiles in the flow is represented.

numbers obtained in previous experiments and those deduced from global linear theory. A possible explanation of this discrepancy is that experiments always have low level noise that might trigger the globally unstable state at a smaller value of the Reynolds number than predicted by the global stability analysis. Since numerical simulations also have a certain noise level, it is expected that the corresponding results for the critical Reynolds number shed some light on the above mentioned discrepancies.

2.2 Formulation

We consider an axisymmetric laminar low-density gaseous jet that discharges into an infinitely large atmosphere of quiescent air at a constant flow rate Q^* through an injector pipe of radius R^* and length L^*_{pipe}, as depicted in figure 2.1. In the description, a cylindrical coordinate system (x^*, r^*) is employed, the flow being independent of the azimuth φ; the origin $(0,0)$ is located at the center of the injector outlet plane. The velocity is denoted in terms of its axial and radial components as $\boldsymbol{u}^* = (u^*, v^*)$. The jet has density ρ^*_j and viscosity μ^*_j, whereas the ambient has density ρ^*_∞ and viscosity μ^*_∞. In this chapter, we focus attention on jets of pure helium discharging into an ambient of air, fixing in this manner the jet-to-ambient density ratio to the value

$$S = \rho^*_j/\rho^*_\infty = 0.143. \tag{2.1}$$

As the values of the dynamic viscosity of helium and that of air only differ by 10%, see Lide (2001), the variations of the viscosity with the jet composition will not be retained in the present work, so that $\mu_j^* = \mu_\infty^*$. In this regard, in the global stability computations of Coenen *et al.* (2017), the changes in the critical Reynolds numbers between using a constant or a variable viscosity were found to be smaller than 6%.

Upstream, the flow enters the injector pipe with a uniform velocity profile of value $U_m^* = 4Q^*/(\pi R^{*2})$, and discharges from it with a velocity profile $u_0^*(r)$ that has the same mean velocity U_m^*, but a shape that varies with the length L_{pipe}^* of the pipe. For small values of L_{pipe}^*, the exit profile is Blasius-like, whereas for large values of L_{pipe}^*, a parabolic Hagen-Poiseuille profile is recovered. The entire collection of profiles for varying L_{pipe}^* is obtained a priori by solving the laminar boundary-layer equations in the circular pipe numerically using the method of lines (see Coenen *et al.* (2008) or Coenen & Sevilla (2012)), as explained in appendix A. The "steepness" of the jet outlet profiles is measured by the momentum thickness, defined as

$$\theta_0^* = \int_0^\infty \frac{u_0^*(r)}{u_0^*(0)}\left[1 - \frac{u_0^*(r)}{u_0^*(0)}\right] \mathrm{d}r^*. \tag{2.2}$$

Length, velocity, time and density are scaled with the jet radius R^*, the mean velocity U_m^*, the convective time R^*/U_m^*, and the jet exit density ρ_j^*, respectively, yielding the dimensionless coordinates (x, r), flow velocity $\boldsymbol{u}(x, r)$, time t, and density $\rho(x, r)$. The flow is fully characterized by the jet-to-ambient density ratio $S = 0.143$, the Reynolds number

$$Re = \rho_j^* U_m^* R^*/\mu_j^*, \tag{2.3}$$

and the inverse of the dimensionless momentum thickness $D/\theta_0 = 2R^*/\theta_0^*$ of the jet exit velocity profile, based here on the diameter instead of the radius for consistency with the literature. Note that the flow development in the injector pipe, and hence the dimensionless injector outlet velocity profile $u_0(r)$, is uniquely determined by the rescaled dimensionless pipe length $L_t = L_{\text{pipe}}/Re = L_{\text{pipe}}^*/(Re\,R^*)$, which in turn is uniquely related to D/θ_0. Very steep Blasius-like profiles correspond to large values of D/θ_0, whereas the parabolic Hagen-Poiseuille profile has the limiting value $D/\theta_0 = 15$. A deep analysis can be seen in appendix A and figure A.2.

For helium-nitrogen jets, the experimentally measured values of the Reynolds numbers associated with the onset of self-sustained oscillations lie typically in the range $100 \lesssim Re \lesssim 1000$, with the exact value depending on the value of D/θ_0. Since the aim of this chapter is the characterization of this onset by direct numerical simulations, the same range of Reynolds numbers will be considered here. This results in slender flows with typical axial dimensionless development lengths $\mathcal{O}(Re)$.

The Mach number $Ma = U_m^*/c^*$, defined as the ratio of the mean velocity and the speed of sound is assumed to be small, $Ma \approx 0$, in agreement with the typical values encountered in the experiments available in the literature (Hallberg & Strykowski, 2006; Kyle &

Sreenivasan, 1993). Then, some simplifications associated with the low-Mach-number approximation as explained by Nichols *et al.* (2007); Williams (1985) can be applied. Theses simplifications imply that the density variations in the jet are restricted only due to variations in molecular weight, and they are not due to pressure variations. Considering also isothermal in all domain if the jet discharges with the same temperature as the atmosphere, and therefore the energy equation is not needed to be considered in the description. Moreover, with the low-Mach-number approximation, the viscous-stress component in the equations that is proportional to the second coefficient of viscosity can be rewritten in the new definition of the pressure p. This pressure p represents the difference from the unperturbed ambient value, scaled with the characteristic dynamic pressure $\rho_j^* {U_m^*}^2$.

Buoyancy effects are neglected, as the Richardson number $Ri = (\rho_\infty^* - \rho_j^*) g^* R^* / (\rho_j^* {U_m^*}^2)$ has small values. In an effort to improve agreement with the experimental observations of Hallberg & Strykowski (2006), Coenen *et al.* (2017) investigated the effect of realistic values of buoyancy on the critical Reynolds numbers for the onset of global instability in the context of a linear stability analysis. Their results show only a small improvement compared to the nonbuoyant case, hence not explaining the discrepancies between linear theory and experiments. In the present work, we will only consider nonbuoyant configurations.

Under these approximations, the jet is effectively described by the continuity, momentum conservation, and species conservation equations,

$$\frac{\partial \rho}{\partial t} + \nabla \cdot \left(\rho \boldsymbol{u}\right) = 0, \tag{2.4}$$

$$\rho \left(\frac{\partial \boldsymbol{u}}{\partial t} + \boldsymbol{u} \cdot \nabla \boldsymbol{u} \right) = -\nabla p + \frac{1}{Re} \nabla^2 \boldsymbol{u}, \tag{2.5}$$

$$\rho \left(\frac{\partial Y}{\partial t} + \boldsymbol{u} \cdot \nabla Y \right) = \frac{1}{Re\, Sc} \nabla \cdot \left(\rho \nabla Y\right), \tag{2.6}$$

The influence of molecular diffusion is characterized by the Schmidt number Sc, fixed here for the helium/nitrogen jets under consideration to the value

$$Sc = \frac{\mu_j^*}{\rho_j^* \mathscr{D}^*} = 1.69, \tag{2.7}$$

$\mathscr{D}^*$ being the binary molecular diffusion coefficient of helium and nitrogen. The molar mass fraction Y of helium is related to the density field ρ as

$$Y = \frac{1/\rho - S}{1 - S}. \tag{2.8}$$

Equations (2.4)–(2.6) must be supplemented with adequate boundary conditions. For $x = 0$ and $r \leq 1$, the velocity profile is the prescribed injector outlet profile, $u = u_0$, $v = 0$,

which depends on the value of D/θ_0; the density is that of the light gas, $\rho = 1$. In the far field, $x^2 + r^2 \to \infty$, the fluid is at rest, $u \to 0$, and the density is that of the heavy ambient, $\rho \to 1/S$. Finally, no-slip conditions $u = v = 0$ must be imposed on the outside walls of the injector pipe, where $r = 1$ and $x \leq 0$.

2.3 General strategy and expected outcome

The principal goal of this chapter is the numerical solution of the time-dependent governing equations (2.4)–(2.6) with appropriate boundary conditions, in order to establish for varying D/θ_0 the critical Reynolds number $Re_c(D/\theta_0)$ above which the flow becomes globally unstable. Let us anticipate the expected outcome of a direct numerical simulation for a certain value D/θ_0 and Re, starting from a certain initial condition. If the value of the Reynolds number is smaller than the critical value Re_c, the flow is expected to evolve to a steady state with the duration of the transient depending on the exact initial conditions. On the other hand, if the Reynolds number is larger than the critical value, the flow is expected to evolve to a limit cycle in which the entire flow field oscillates in a self-sustained manner. Following the Stuart-Landau theory, (see, for example, Sreenivasan *et al.* (1987)) in the vicinity of the bifurcation, i.e. for Reynolds numbers Re only slightly larger than Re_c, the square of the oscillation amplitude of the limit cycle, A^2, is expected to increase linearly with the distance to the bifurcation, such that $A^2 \sim Re - Re_c$.

In view of the anticipated behavior outlined previously, the procedure that was taken in this work to determine the marginal curve $Re_c(D/\theta_0)$ is as follows. For fixed values of D/θ_0, direct numerical simulations were launched for a discrete set of increasing Reynolds numbers, monitoring the evolution of the oscillations of the flow field. The simulations were carried out until either a steady solution with negligible flow-field oscillations, or a limit cycle with a steady oscillation amplitude was obtained. To minimize the duration of the transients, we used as initial condition a steady solution of the equations of motion. The latter was obtained a priori using a Newton-Raphson algorithm. Finally, with the oscillation amplitudes of the limit cycles for various values of Re, the Stuart-Landau theory was employed to determine the value of Re_c.

In the next section we discuss the numerical methods that were employed in this chapter.

2.4 Numerical methods

For the numerical discretization of the governing equations, the finite element method was used. To this aim, the versatile open source code `FreeFEM++` was employed, which will be briefly discussed next. In the remainder of this section, we present in

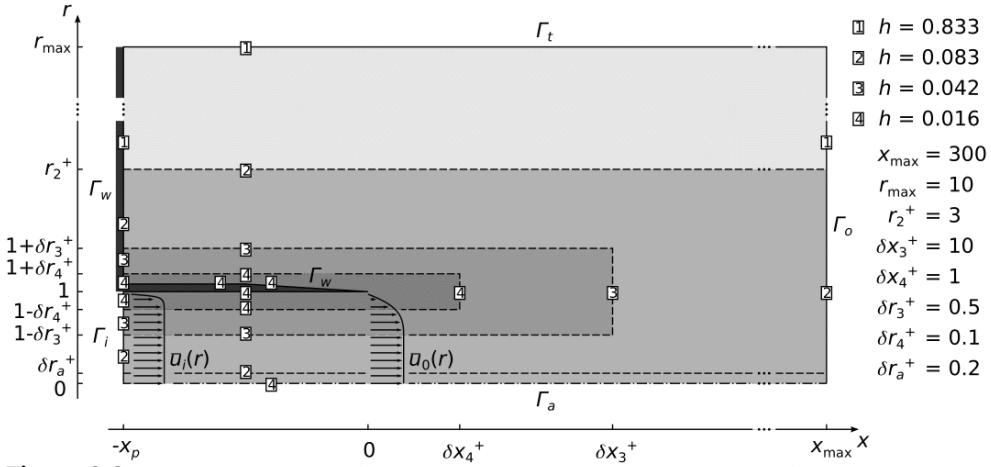

Figure 2.2: Schematic diagram of the computational mesh. Darker shades of gray correspond to smaller cell size. The values of h on the right-hand side indicate the typical cell size of the respective areas in the diagram.

subsection 2.4.2 a description of the computational domain and the computational mesh, followed by a description of how the initial conditions in the form of steady solutions of the governing equations were obtained in subsection 2.4.3. Finally, the time stepping algorithm is explained in detail in subsection 2.4.4.

2.4.1 A few words on FreeFEM++

`FreeFEM++` is a code based on the `C++` language that uses ARPACK libraries (Fortran subroutines for solving large scale eigenvalue problems) and MPI (Message Passing Interface, which is a standard for message-passing in parallel computing architectures, that works with `C++` and Fortran). In essence, it is a partial differential equation solver which has its own programming language, resembling `C++`. The code works in several operative systems such as Windows, UNIX and Mac. Through user-written scripts, a broad range of multi-physics problems can be solved in two- and three-dimensional configurations. It has an automatic mesh generator, and the capability to adapt the mesh to a user-specified metric. Finite element spaces are created on the mesh, with various finite element types to choose from. A detailed description can be found in Hecht (2012) and in the `FreeFEM++` manual. In this chapter, version 3-35 was used.

2.4.2 Computational mesh

Figure 2.2 shows a schematic representation of the computational domain and mesh that was employed for the numerical integrations. The domain includes a fixed part of length $x_p = 2$ of the injector pipe. Note that x_p must not be confused with L_{pipe} introduced in the

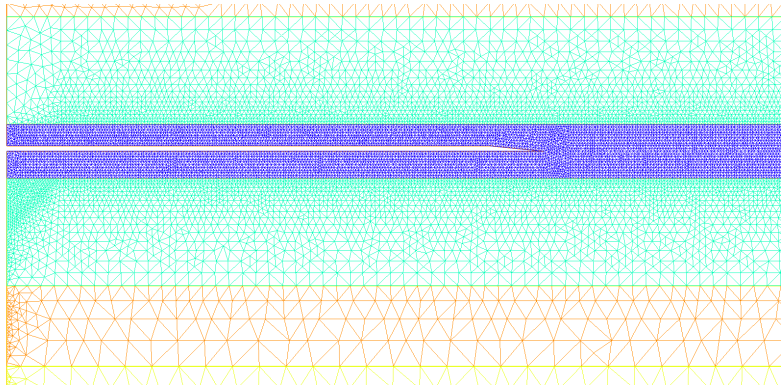

Figure 2.3: An example of the typical mesh refinement around the end of the injector pipe wall.

formulation in section 2.2. To capture correctly the shear layer that forms downstream of the injector exit, the mesh incorporates regions of increasing refinement, as indicated in the figure with darker shades of grey. In the figure, h indicates the typical triangle size. This mesh configuration is similar to that used in Coenen *et al.* (2017). It was ensured that the results were independent on the mesh refinement.

The distances $r_{\max}$ and $x_{\max}$ from the center of the injector outlet to the lateral and downstream boundaries, respectively, were chosen sufficiently large for the results not to depend on their value. In particular, we used $x_{\max} = 300$ and $r_{\max} = 60$. The large downstream extent of the computational domain was essential to describe accurately the onset of the self-sustained oscillations of the jet flow field. The resulting number of triangles in a typical mesh is on the order of 100,000 with approximately 55,000 vertices. Figure 2.3 gives an example of the typical mesh refinement near the end of the injector pipe wall.

The boundary conditions used in the numerical simulations are as follows. At the injector inlet Γ_i, $u = u_i(r)$, $v = 0$ and $\rho = 1$, where $u_i(r)$ is the appropriate inlet velocity profile that results in a velocity profile at the injector outlet with the desired value of D/θ_0. Note that for a given value of D/θ_0, that profile $u_i(r)$ only depends on x_p/Re, and its corresponding momentum thickness D/θ_i can be looked up with the help of figure A.2. Along the axis Γ_a, $\partial u/\partial r = v = \partial \rho/\partial r = 0$. On the walls, Γ_w, no-slip conditions $u = 0$, $v = 0$ are imposed. At the lateral and downstream boundaries, Γ_t and Γ_o, we impose $\rho = 1/S$ and $\partial \rho/\partial x = 0$, respectively. On both these boundaries, stress-free conditions are imposed: $-p\boldsymbol{n} + Re^{-1}\boldsymbol{n} \cdot \nabla \boldsymbol{u} = 0$.

For the unsteady simulation, the mesh is adapted in order to reduce the number of degrees of freedom, thus optimizing the simulation time. This was carried out using the `FreeFEM++` command *adaptmesh* whose performance depends of several parameters. To properly capture the region of instability development, the azimuthal vorticity was selected as the adaptation variable with the following settings: a maximum interpolation

error of 10^{-4} and a smoothing ratio of 1.1 to provide a smooth transition of cells.

2.4.3 Computation of steady solutions

The initial conditions used for the time-dependent numerical simulations are steady solutions of the governing equations of motion. These were obtained with a Newton-Raphson algorithm which, starting from an initial guess, iterates until a desired level of convergence is achieved. This procedure and its implementation are identical to those used by Coenen *et al.* (2017), in which such steady solutions were used as basic flows to perform a linear stability analysis. Note that, for increasing Reynolds numbers, the radius of convergence of the Newton-Raphson algorithm decreases. Therefore, a continuation method was employed in which the Reynolds number was increased in about 6 steps from a value of order unity to its desired final value. In every step, the Newton-Raphson algorithm was initialized with the converged solution of the previous step.

The Newton-Raphson algorithm consists in finding a root of a set of nonlinear algebraic equations, $F(X) = 0$, in the iterative form $X^{n+1} = X^n - J(X^n)^{-1} \cdot F(X^n)$, where the Jacobian $J = \frac{F(X+\delta X)-F(X)}{\delta X}$. Here, the superscript n refers to the iteration level, and δX is a small increment of the vector of unknowns. To achieve convergence an initial value close enough to the root is needed. Thus, the Newton-Raphson algorithm was applied to the problem at hand in combination with a standard continuation method, ensuring convergence. A more detailed description of the Newton-Raphson method can be seen in Ben-Israel (1966).

Since `FreeFEM++` is a finite element solver, the equations needed to compute the Jacobian have to be written in variational or weak form, using test functions q, w_1, w_2, and s_Y for the continuity, momentum conservation and species conservation equations, respectively. Moreover, to avoid singularities, the momentum equations are first multiplied by r. Note that the Laplacian operator is transformed using Green's identity (see Lanczos (1996)). Let ψ and φ be scalar functions defined on some region Ω enclosed by the surface $\partial\Omega$ with normal vector $\boldsymbol{n}$. The Green's identity writes,

$$\int_\Omega \psi \nabla^2 \varphi \, \mathrm{d}V = \oint_{\partial\Omega} \psi \left(\nabla\varphi \cdot \boldsymbol{n}\right) \mathrm{d}S - \int_\Omega \left(\nabla\varphi \cdot \nabla\psi\right) \mathrm{d}V. \tag{2.9}$$

The weak forms of the steady axisymmetric governing equations are integrals over the computational domain in cylindrical coordinates, which have to include the test functions defined above. Denoting by Σ the axisymmetric domain to apply the integrals, the weak form of the mass conservation equation is

$$\int_\Sigma q \left[\rho \frac{\partial u}{\partial x} + \rho \frac{\partial v}{\partial r} + \frac{v}{r}\right] r \, dx \, dr = 0, \tag{2.10}$$

while the axial and radial momentum equations read, respectively,

$$-\int_{\Sigma}\rho w_1\left[u\frac{\partial u}{\partial x}+v\frac{\partial u}{\partial x}\right]r^2\,dx\,dr-\int_{\Sigma}p\frac{\partial w_1}{\partial x}r^2\,dx\,dr$$
$$+\int_{\Sigma}\frac{1}{Re}\left[\frac{\partial w_1}{\partial x}\frac{\partial u}{\partial x}+\frac{\partial w_1}{\partial r}\frac{\partial u}{\partial r}+\frac{1}{3}\frac{\partial w_1}{\partial x}\left(\frac{\partial u}{\partial x}+\frac{\partial v}{\partial r}+\frac{v}{r}\right)\right]r^2\,dx\,dr=0, \quad (2.11)$$

and

$$-\int_{\Sigma}\rho w_2\left[u\frac{\partial v}{\partial r}+v\frac{\partial v}{\partial r}\right]r^2\,dx\,dr-\int_{\Sigma}p\frac{\partial w_2}{\partial r}r^2\,dx\,dr$$
$$+\int_{\Sigma}\frac{1}{Re}\left[\frac{\partial w_2}{\partial r}\frac{\partial v}{\partial r}+\frac{\partial w_2}{\partial r}\frac{\partial v}{\partial r}+\frac{w_2}{r}\frac{\partial v}{\partial r}+\frac{w_2 v}{r^2}\right]r^2\,dx\,dr$$
$$+\int_{\Sigma}\frac{1}{Re}\left(\frac{1}{3}\left[\frac{\partial w_2}{\partial r}+\frac{2w_2}{r}\right)\left(\frac{\partial u}{\partial x}+\frac{\partial v}{\partial r}+\frac{v}{r}\right)\right]r^2\,dx\,dr=0. \quad (2.12)$$

Finally, the species conservation equation writes

$$-\int_{\Sigma}S_y\left[u\frac{\partial Y}{\partial x}+v\frac{\partial Y}{\partial r}\right]r\,dx\,dr+\int_{\Sigma}S_y\frac{1}{Re\,Sc}\left[\frac{\partial\rho}{\partial x}\frac{\partial Y}{\partial x}+\frac{\rho}{r}\frac{\partial Y}{\partial r}\right]r\,dx\,dr=0. \quad (2.13)$$

To apply the Newton-Raphson algorithm all the flow variables appearing in equations (2.10) – (2.13) are decomposed into a base component plus a small variation,

$$(u,v,\rho,p)=(\overline{u},\overline{v},\overline{\rho},\overline{p})+\varepsilon(u',v',\rho',p'), \quad (2.14)$$

where $\varepsilon \ll 1$, and a linearization procedure is applied to obtain the Jacobian. The resulting equations are (2.15) – (2.18).

To reduce the number of variables, a combination of equations (2.10) and (2.13) is introduced in (2.15), where the substitutions $\overline{Y}=Y_j(\overline{\rho}^{\,-1}-S)/(1-S)$ and $Y'=-Y_j\,\rho'/(1-S)\overline{\rho}^{\,-2}$ have been used. Here, $Y_j=(1/S-1)/(W_{He-N_2}-1)$.

$$\int_\Sigma q\left[\frac{\partial\overline{\rho}}{\partial x}u'+\overline{\rho}\frac{\partial u'}{\partial x}+\frac{\partial\rho'}{\partial x}\overline{u}+\rho'\frac{\partial\overline{u}}{\partial x}\right]r\,dx\,dr$$
$$+\int_\Sigma q\left[\frac{\partial\overline{\rho}}{\partial r}v'+\overline{\rho}\frac{\partial v'}{\partial r}+\frac{\partial\rho'}{\partial r}\overline{v}+\rho'\frac{\partial\overline{v}}{\partial r}+\overline{\rho}\frac{v'}{r}+\rho'\frac{\overline{v}}{r}\right]r\,dx\,dr$$
$$+\int_\Sigma q\frac{1-S}{Y_j}\overline{\rho}\left[\overline{u}\frac{\partial Y'}{\partial x}+u'\frac{\partial\overline{Y}}{\partial x}+\overline{v}\frac{\partial Y'}{\partial r}+v'\frac{\partial\overline{Y}}{\partial r}\right]\rho' r\,dx\,dr$$
$$+\int_\Sigma q\frac{1-S}{Y_j}\overline{\rho}\left[\overline{u}\frac{\partial\overline{Y}}{\partial x}+\overline{v}\frac{\partial\overline{Y}}{\partial r}\right]\rho' r\,dx\,dr$$
$$-\int_\Sigma q\frac{1}{Re\,Sc}\left[\frac{1}{\overline{\rho}}\left(\frac{\partial\overline{\rho}}{\partial x}\frac{\partial Y'}{\partial x}+\frac{\partial\rho'}{\partial x}\frac{\partial\overline{Y}}{\partial x}+\rho'\frac{\partial^2\overline{Y}}{\partial x^2}\right)\right]r\,dx\,dr$$
$$-\int_\Sigma q\frac{1}{Re\,Sc}\left[\frac{1}{\overline{\rho}}\left(\overline{\rho}\frac{\partial Y'}{\partial r}+\frac{\partial\overline{\rho}}{\partial r}\frac{\partial Y'}{\partial r}+\rho'\frac{\partial\overline{Y}}{\partial r}+\frac{\partial\rho'}{\partial r}\frac{\partial\overline{Y}}{\partial r}+\rho'\frac{\partial^2\overline{Y}}{\partial r^2}\right)\right]r\,dx\,dr=0, \tag{2.15}$$

$$\int_\Sigma w_1\left[\overline{\rho}\left(\overline{u}\frac{\partial u'}{\partial x}+u'\frac{\partial\overline{u}}{\partial x}+\overline{v}\frac{\partial u'}{\partial r}+v'\frac{\partial\overline{u}}{\partial r}\right)+\rho'\left(\overline{u}\frac{\partial\overline{u}}{\partial x}+\overline{v}\frac{\partial\overline{u}}{\partial r}\right)\right]r^2\,dx\,dr$$
$$+\int_\Sigma w_1 p'\frac{\partial w_1}{\partial x}r^2\,dx\,dr$$
$$-\int_\Sigma\frac{1}{Re}\left[\frac{\partial w_1}{\partial x}\frac{\partial\overline{u}}{\partial x}+\frac{\partial w_1}{\partial r}\frac{\partial\overline{u}}{\partial r}+\frac{1}{3}\frac{\partial w_1}{\partial x}\left(\frac{\partial\overline{u}}{\partial x}+\frac{\partial\overline{v}}{\partial r}+\frac{\overline{v}}{r}\right)\right]r^2\,dx\,dr=0, \tag{2.16}$$

$$\int_\Sigma w_2\left[\overline{\rho}\left(\overline{u}\frac{\partial v'}{\partial x}+u'\frac{\partial\overline{v}}{\partial x}+\overline{v}\frac{\partial v'}{\partial r}+v'\frac{\partial\overline{v}}{\partial r}\right)+\rho'\left(\overline{u}\frac{\partial\overline{v}}{\partial x}+\overline{v}\frac{\partial\overline{v}}{\partial r}\right)\right]r^2\,dx\,dr$$
$$+\int_\Sigma w_2 p'\frac{\partial w_2}{\partial r}r^2\,dx\,dr$$
$$-\int_\Sigma\frac{1}{Re}\left[\frac{\partial w_2}{\partial x}\frac{\partial\overline{u}}{\partial x}+\frac{\partial w_2}{\partial r}\frac{\partial\overline{u}}{\partial r}+w_2\frac{\partial v'}{\partial r}+w_2 v'\right]r^2\,dx\,dr=0$$
$$-\int_\Sigma\frac{1}{3Re}\left[\frac{\partial w_2}{\partial r}\left(\frac{\partial\overline{u}}{\partial r}+\frac{\partial\overline{v}}{\partial r}+\frac{\overline{v}}{r}\right)\right]r^2dxdr=0, \tag{2.17}$$

$$\int_\Sigma qr\frac{1-S}{Y_j}\overline{\rho}\left[\overline{u}\frac{\partial\overline{Y}}{\partial x}+\overline{v}\frac{\partial\overline{Y}}{\partial r}\right]\rho' r\,dx\,dr$$
$$-\int_\Sigma qr\frac{1}{Re\,Sc}\left[\frac{r}{\overline{\rho}}\left(\frac{\partial\overline{\rho}}{\partial x}\frac{\partial Y'}{\partial x}+\frac{\partial\rho'}{\partial x}\frac{\partial\overline{Y}}{\partial x}+\rho'\frac{\partial^2\overline{Y}}{\partial x^2}\right)\right]r\,dx\,dr$$
$$-\int_\Sigma q\frac{1}{Re\,Sc}\left[\frac{1}{\overline{\rho}}\left(\overline{\rho}\frac{\partial Y'}{\partial r}+r\frac{\partial\overline{\rho}}{\partial r}\frac{\partial Y'}{\partial r}+\rho'\frac{\partial\overline{Y}}{\partial r}+\frac{\partial\rho'}{\partial r}\frac{\partial\overline{Y}}{\partial r}+\rho'\frac{\partial^2\overline{Y}}{\partial r^2}\right)\right]r\,dx\,dr=0, \tag{2.18}$$

with boundary conditions

$$B.C.\begin{cases}\partial_r u'=v'=0 \text{ on } \Gamma_a,\\ u'=v'=0 \text{ on } \Gamma_w,\\ u'=v'=\rho'=0 \text{ on } \Gamma_i,\\ -p'\boldsymbol{n}+\boldsymbol{n}/Re\cdot\nabla(u',v')=0 \text{ on } \Gamma_o,\Gamma_t\end{cases}$$

The Newton-Raphson algorithm is applied to find a converged solution with a tolerance of 10^{-15} by first increasing the Reynolds number from $Re=1$ in 6 steps, and then reducing the density ratio from a value $S=0.99$ in another 6 steps. The computational time is approximately 1 hour using one core of Intel® Xeon® CPU E5-2630 v2 at 2.6 GHz. The results obtained are identical to those reported by Coenen *et al.* (2017).

2.4.4 Time-stepping algorithm

Once a steady solution was converged for a given parameter combination, it was used as the initial condition for the numerical simulation of the unsteady governing equations (2.4) – (2.6) subjected to the boundary conditions discussed in section 2.4.2.

To integrate the unsteady term, `FreeFEM++` incorporates an operator called *convect*. Let us illustrate how it works by introducing the hyperbolic equation

$$\partial_t u-\boldsymbol{\alpha}\cdot\nabla u=f, \tag{2.19}$$

for a vector-valued function $\boldsymbol{\alpha}$, time derivative $\partial_t=\frac{\partial}{\partial t}$ and dependent variable u. Using the Characteristic-Galerkin method for convection operators, it can be discretized as follows,

$$\frac{Du}{Dt}=f \text{ i.e. } \frac{du}{dt}\big(X(t),t\big)=f\left(X(t),t\right) \text{ where } \frac{dX}{dt}(t)=\boldsymbol{\alpha}(X(t),t), \tag{2.20}$$

where D is the material derivative. This equation is discretized using a one-step backward

convection called the Characteristic-Galerkin method,

$$\frac{1}{\tau}\left(u^{m+1}(X^{m+1}(x)) - u^m(X^m(x))\right) = f^m(x), \tag{2.21}$$

where $X^m(x)$ is an approximation of the solution at $t = m\tau$. A first order Taylor expansion can now be applied to get

$$u^m\left(X^m(x)\right) \approx convect\left([a_1^m, a_2^m], \tau, u^m\right) \text{ by } x = X((m+1)\tau), \tag{2.22}$$

indicating that the *convect* operator provides a good approximation to the solution. The reader is referred to Hecht (2012) for more details.

A schematic representation of the time stepping algorithm is provided in figure 2.4. Once the program has been started and the variables have been declared, the initial conditions are read under the form of a steady solution of the governing equations of motion on a block-refined mesh, as explained in section 2.4.2. This mesh is then adapted to the solution using the vorticity as a metric. After that, we set up multi-core parallelization—using scotch for mesh partitioning and parallel sparse matrix block ordering—by decomposing the domain into several subdomains, before initiating the time-stepping loop. Inside this loop, the solution is computed separately using different cores on the different mesh subdomains, and when all cores have finished, the complete solution is recomposed and saved.

Note that to avoid both the accumulation of interpolation errors, as well as technical difficulties with the mesh decomposition, it was decided not to adapt the mesh at every time step. Since the mesh was adapted to the steady solution of the governing equations, and the regime of interest in this work lies in the vicinity of the bifurcation to the globally unstable state—hence guaranteeing small oscillation amplitudes—this approach was found adequate. Each time step is solved in approximately 30 seconds using 4 cores of Intel® Xeon® CPU E5-2630 v2 with 2.6 GHz processor speed. The mass conservation equation (2.23) is described using the material derivative and written in cylindrical coordinates with a scale factor in the longitudinal axis.

$$\int_\Sigma q\left[\frac{D\overline{\rho}}{Dt} + \left(\overline{\rho}\frac{\partial \overline{u}}{\partial x} + \overline{\rho}\frac{\partial \overline{v}}{\partial r} + \frac{\overline{v}}{r}\right)\right] r\, dx\, dr = 0. \tag{2.23}$$

Both equations (2.24) and (2.25) are the axial and radial momentum conservation equations, respectively.

$$\begin{aligned}\int_\Sigma w_1\left[\overline{\rho}\frac{D\overline{u}}{Dt}\right] r^2\, dx\, dr = &-\int_\Sigma \overline{p}\frac{\partial w_1}{\partial x} r^2\, dx\, dr \\ &+ \int_\Sigma \frac{1}{Re}\left(\frac{\partial w_1}{\partial x}\frac{\partial \overline{u}}{\partial x} + \frac{\partial w_1}{\partial r}\frac{\partial \overline{u}}{\partial r} + \frac{1}{3}\frac{\partial w_1}{\partial x}\left(\frac{\partial \overline{u}}{\partial x} + \frac{\partial \overline{v}}{\partial r} + \frac{\overline{v}}{r}\right)\right) r^2\, dx\, dr,\end{aligned} \tag{2.24}$$

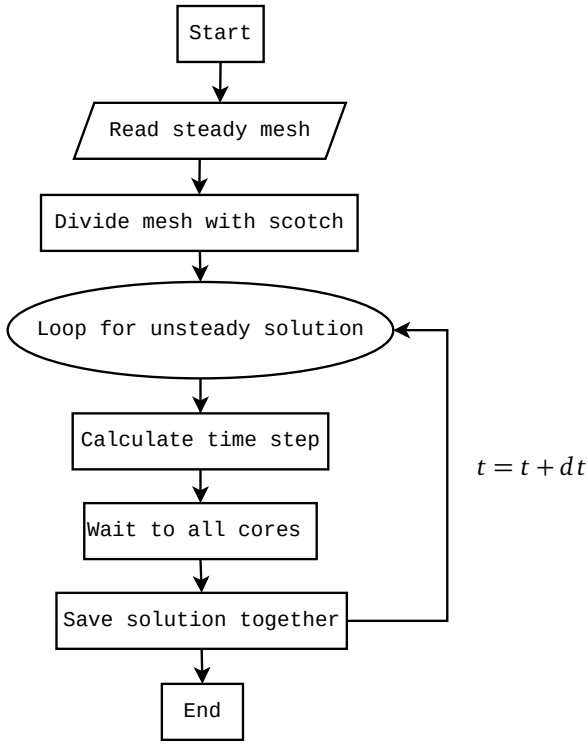

Figure 2.4: Unsteady code flow chart

$$\int_\Sigma w_2 \left[\overline{\rho}\frac{D\overline{v}}{Dt}\right] r^2\, dx\, dr = -\int_\Sigma \overline{p}\frac{\partial w_2}{\partial r} r^2\, dx\, dr + \int_\Sigma \frac{1}{Re}\left(\frac{\partial w_2}{\partial r}\frac{\partial \overline{v}}{\partial r} + \frac{\partial w_2}{\partial r}\frac{\partial \overline{v}}{\partial r} + \frac{w_2}{r}\frac{\partial \overline{v}}{\partial r} + \frac{w_2\overline{v}}{r^2}\right) r^2\, dx\, dr + \int_\Sigma \frac{1}{Re}\left(\frac{1}{3}\left(\frac{\partial w_2}{\partial r} + \frac{2w_2}{r}\right)\left(\frac{\partial \overline{u}}{\partial x} + \frac{\partial \overline{v}}{\partial r} + \frac{\overline{v}}{r}\right)\right) r^2\, dx\, dr, \quad (2.25)$$

Finally, equation (2.26) is the species conservation equation in weak form.

$$\int_\Sigma S_y \left[\overline{\rho}\frac{\partial \overline{Y}}{\partial \overline{\rho}}\frac{D\overline{Y}}{Dt}\right] r\, dx\, dr = \int_\Sigma S_y \frac{1}{Re\, Sc}\left[\frac{\partial \overline{\rho}}{\partial x}\frac{\partial \overline{Y}}{\partial x} + \frac{\overline{\rho}}{r}\frac{\partial \overline{Y}}{\partial r}\right] r\, dx\, dr, \quad (2.26)$$

Simulations were performed to obtain at least 150 oscillation periods, with a time step small enough to fulfill the Courant-Friedrich-Levy number or CFL condition defined in equation (2.27), following Courant *et al.* (1928).

$$C = \frac{u\,\Delta t}{\Delta x} < 1, \quad (2.27)$$

where u is the velocity in the cell, Δt is the time step and Δx is the axial size of the cell.

2.5 Results

We now present results of the direct numerical simulations of helium jets discharging into a quiescent atmosphere of nitrogen ($S = 0.143$) in the range $15 \leq D/\theta_0 \leq 35$, which is the same range that was considered both in the experimental work of Hallberg & Strykowski (2006) and the global stability analysis of Coenen *et al.* (2017). We remind the reader that $D/\theta_0 = 15$ corresponds to the parabolic Hagen-Poiseuille profile, whereas $D/\theta_0 = 35$ can be considered to be of the top-hat kind (see figure A.1). We will present detailed results for these two limiting cases, for different values of the Reynolds number. For the sake of reference, the values of the critical Reynolds number observed in experiments and predicted with global linear theory are respectively 680 and 850 for $D/\theta_0 = 15$, and 190 and 300 for $D/\theta_0 = 35$.

Figures 2.5 and 2.6 show the temporal evolution of the flow field of the jet emerging with a parabolic velocity profile ($D/\theta_0 = 15$) for $Re = 580$, as a series of snapshots of its density and vorticity fields, respectively. For this combination of values of the governing parameters, the jet is found to be globally unstable, exhibiting self-sustained oscillations of the entire flow field. These manifest themselves under the form of a series of vortices in the jet shear layer, generated periodically at small distances $x \simeq 5$ from the injector outlet. In the figures we show approximately one period of oscillation, so that the top and penultimate frame correspond to almost identical states of the flow field. The density contours in figure 2.5 show how the vortical structures enhance mixing. In the figure, the light yellow colors corresponds to the jet outlet density, $\rho = 1$, whereas the dark red color corresponds to the heavier ambient density, $\rho = 1/S = 7$. The periodic nature of the vortices can be more clearly observed in figure 2.6, where colors encode the values of the vorticity, red corresponding to 2, white to 1 and blue to 0. These results are similar to those encountered by Lesshafft *et al.* (2007) in a study of heated jets with hyperbolic-tangent outlet profiles, where the presence of solid boundaries was disregarded. Notice also that there is no indication of vortex pairing for these values of S, D/θ_0 and Re.

To give quantitative information about the dynamics of the flow field, and how it changes for different values of the control parameters, it is more convenient to monitor the temporal evolution of a certain quantity, either at a single spatial position, or along a line in the flow field. Results for the first these two approaches are shown in figures 2.7(a, b) and figures 2.8(a, b), focusing on the temporal evolution of the density field at the point $(x = 1, r = 1)$. Following the second approach results in figures 2.7(c, d) and figures 2.8(c, d), where again the density is plotted in space-time diagrams, but now along the line $r = 1$. In these figures, four different combinations of D/θ_0 and Re are considered.

Let us start the discussion with figure 2.7, which shows the case $(D/\theta_0 = 15, Re = 500)$

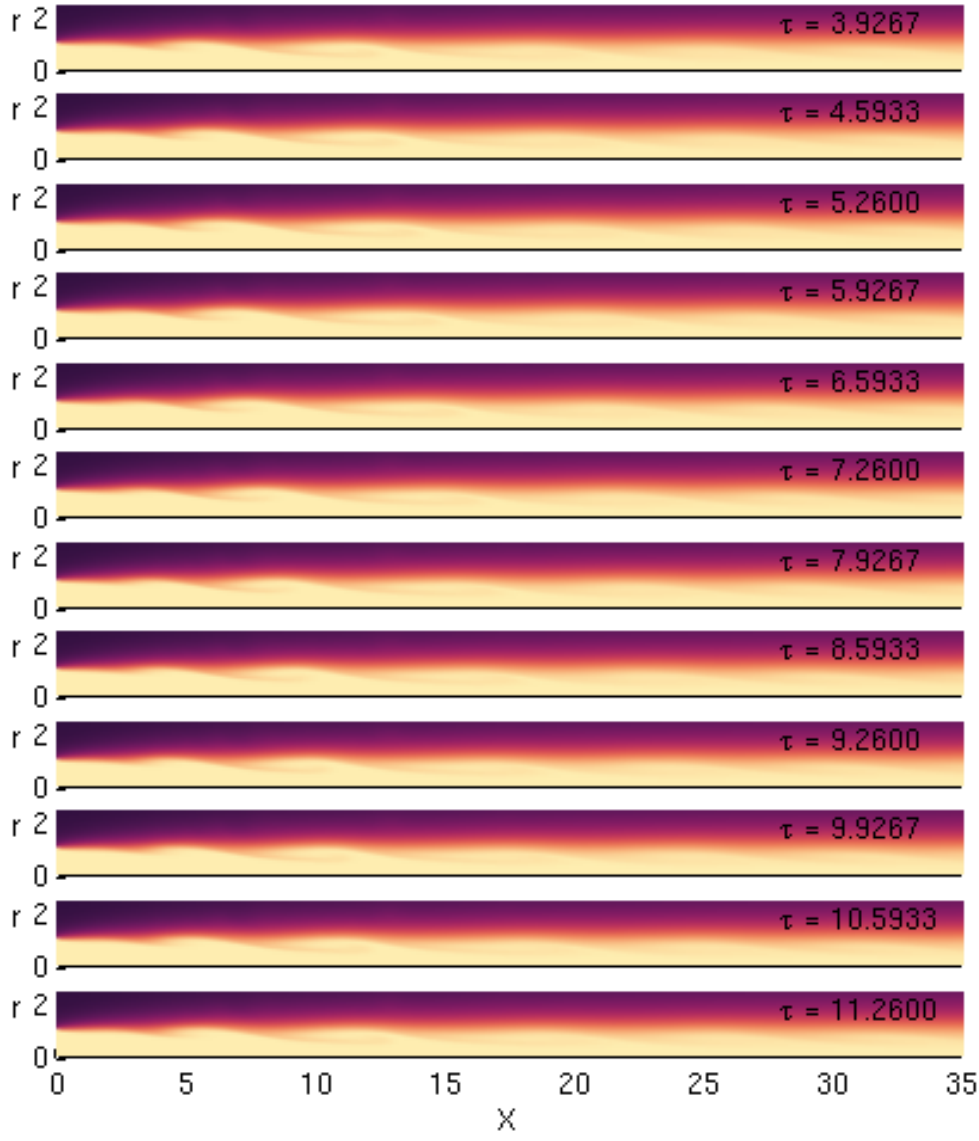

Figure 2.5: Temporal evolution of a helium jet discharging in nitrogen atmosphere ($S = 0.143$), for $D/\theta_0 = 15$ and $Re = 580$, during approximately one oscillation period at the dominant oscillation frequency. Colors indicate the value of the density ρ, the light yellow corresponding to $\rho = 1$, and the dark red corresponding to $\rho = 1/S = 7$. Dimensionless time is represented as $\tau = R^*/U_m^*$. Note that only a part of the total computational domain is shown in the figure.

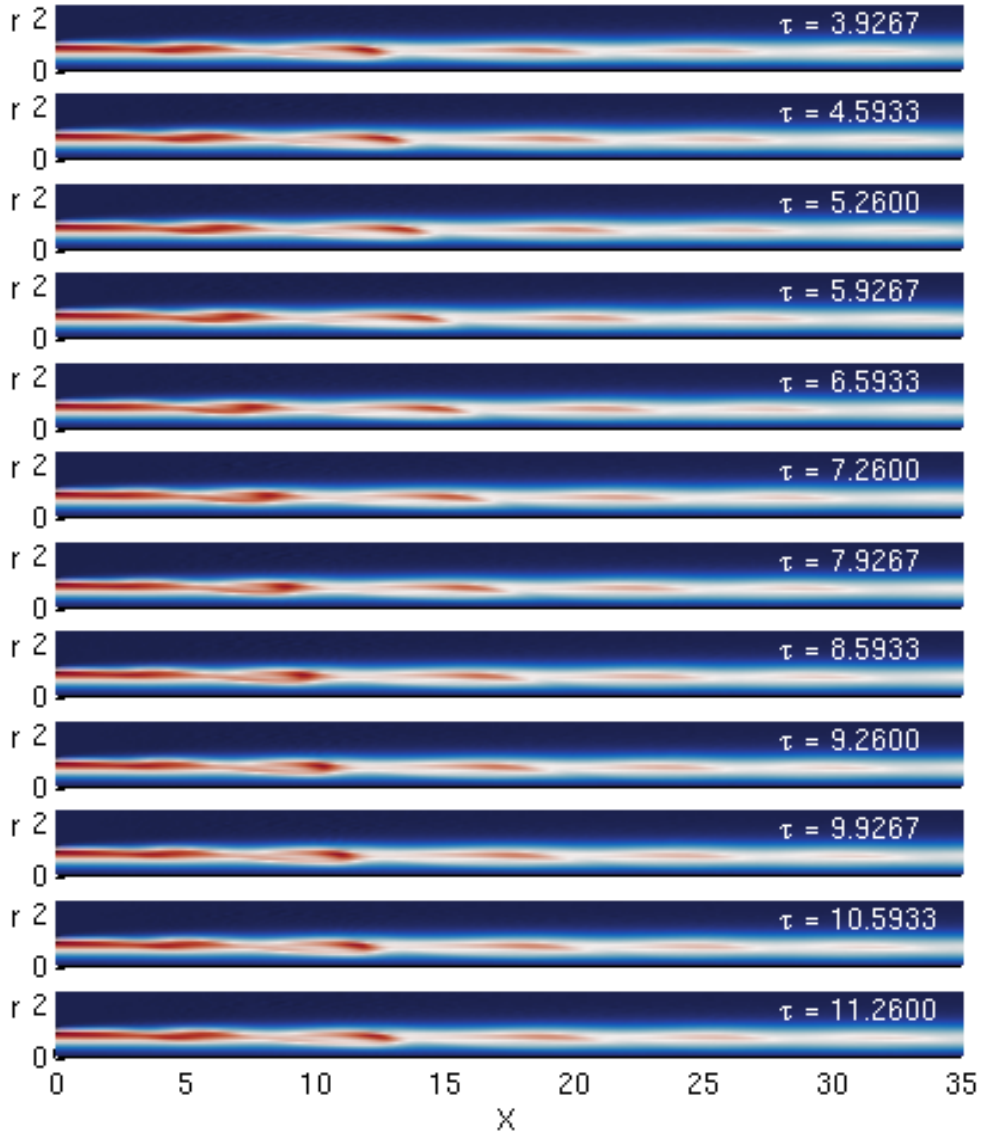

Figure 2.6: Temporal evolution of a helium jet discharging in nitrogen atmosphere ($S = 0.143$), for $D/\theta_0 = 15$ and $Re = 580$, at the same time instants as in figure 2.5. Colors indicate the value of the azimuthal vorticity, red corresponding to 2, white to 1, and blue to 0. Dimensionless time is represented as $\tau = R^*/U_m^*$. Note that only a part of the total computational domain is shown in the figure.

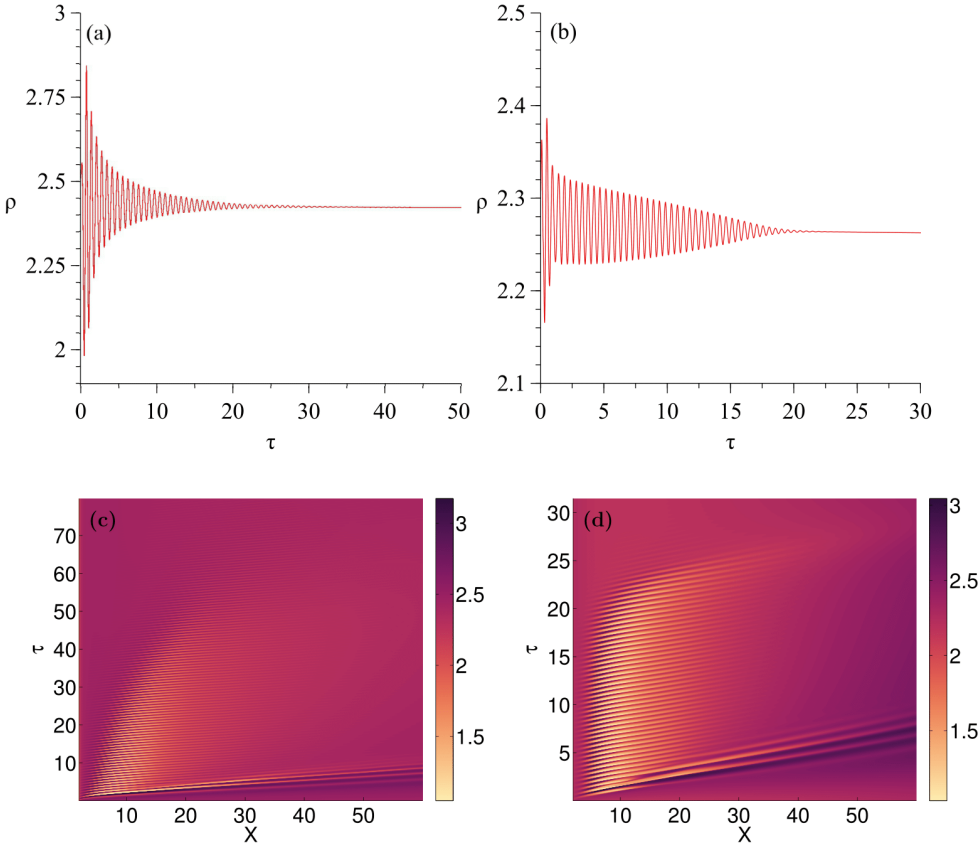

Figure 2.7: Temporal evolution of the density field for $D/\theta_0 = 15$ and $Re = 500$ on the left-hand side (a, c) and $D/\theta_0 = 35$ and $Re = 200$ on the right-hand side (b, d). Top panels (a, b): evolution at a single spatial position ($x = 1, r = 1$). Bottom panels (c, d): space-time diagram of the density field along the line $r = 1$.

on the left-hand side (a, b), and the case ($D/\theta_0 = 35, Re = 200$) on the right-hand side (b, d). From the time evolution in a single point, i.e. the top panels (a, b), it can be seen how, after undergoing an initial perturbation, the value of the density relaxes to a constant value. All other points along the line $r = 1$ undergo the same evolution, as shown in the space-time diagrams (c, d). Note that in these panels a cut along the vertical line $x = 1$ reproduces the data of the panels (a, b) again. The time it takes for the initial perturbation to be washed away changes with the axial position x, but eventually, a steady state is obtained throughout the entire flow domain. These results thus clearly indicate that the cases ($D/\theta_0 = 15, Re = 500$) and ($D/\theta_0 = 35, Re = 200$) are globally stable. In the former case, ($D/\theta_0 = 15, Re = 500$), this is consistent with the experimental and the theoretical stability margins pointed out at the beginning of this section. On the contrary, for the latter case, ($D/\theta_0 = 35, Re = 200$), the results are in agreement with the predictions of

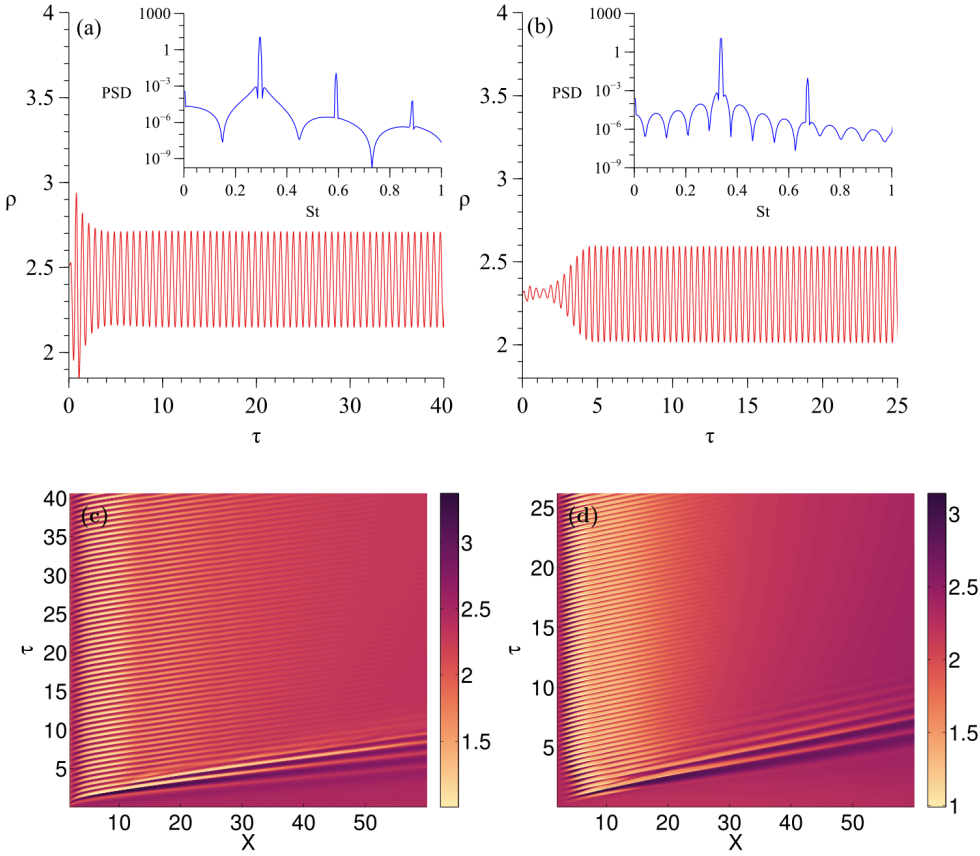

Figure 2.8: Temporal evolution of the density field for $D/\theta_0 = 15$ and $Re = 800$ on the left-hand side (a, c) and $D/\theta_0 = 35$ and $Re = 280$ on the right-hand side (b, d). Top panels (a, b): evolution at a single spatial position ($x = 1, r = 1$); insets show the power spectral density of the corresponding signals. Bottom panels (c, d): space-time diagram of the density field along the line $r = 1$.

the global stability analysis of Coenen *et al.* (2017), but in disagreement with Hallberg & Strykowski (2006), who observed the flow to be unstable for this combination of control parameters.

We now proceed to discuss figure 2.8, which shows the results for the same values of D/θ_0, but for corresponding Reynolds numbers that are considerably larger than those discussed before in figure 2.7: ($D/\theta_0 = 15, Re = 800$) on the left-hand side (a, c), and ($D/\theta_0 = 35, Re = 280$) on the right-hand side (b, d). In both cases, it can be seen how the jet undergoes an initial perturbation that washes away, after which it evolves towards a limit cycle in which it oscillates with a constant amplitude. This globally unstable behavior corresponds to that described in the introductory figures 2.5 and 2.6 discussed earlier in this section. Here too, the space-time diagrams do not show evidence of vortex pairing occurring in the jet shear layer.

The power spectral density of the temporal evolution of the density at $(x = 1, r = 1)$ is shown in the insets of figures 2.8(a, b). In both cases, a clear peak is observed for a Strouhal number $St \simeq 0.3$, together with its harmonics. Here, the Strouhal number is the dimensionless frequency based on the jet diameter and the jet mean outlet velocity, namely $St = 2f^*R^*/U_m^*$.

The Strouhal number obtained from the present simulations is slightly different from both the experimental results of Hallberg & Strykowski (2006) and the global stability analysis performed by Coenen *et al.* (2017). Indeed, the value of St obtained from the DNS is 24.6% larger than the experimental one, and between 5.6% and 14.9% larger than that obtained with linear stability theory. Interestingly, the first and second harmonics can also be appreciated in the experiments of Hallberg & Strykowski (2006).

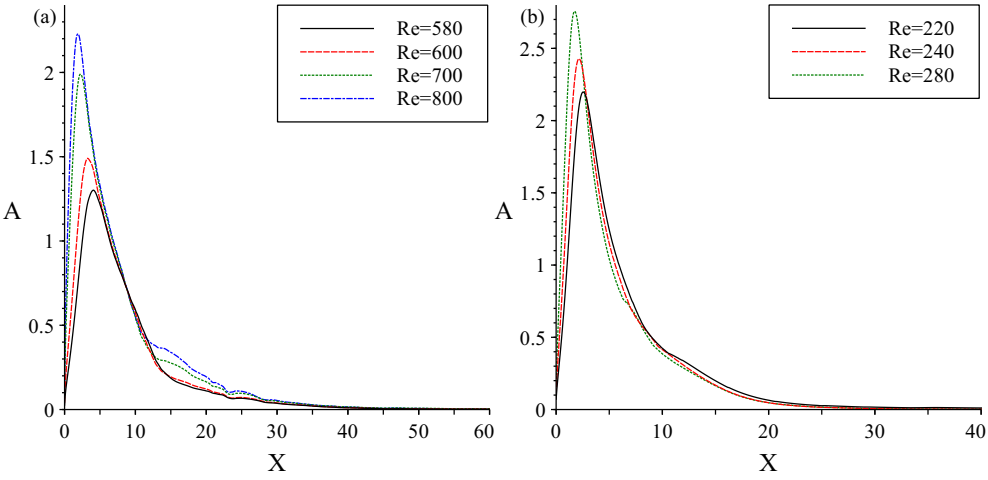

Figure 2.9: Normalized amplitude of the limit-cycle density oscillations along the line $r = 1$ for globally unstable jets with (a) $D/\theta_0 = 15$ and (b) $D/\theta_0 = 35$, and for different values of Re, as indicated in the legend.

From the color intensity in the space-time diagrams in figures 2.7(c, d) it can be deduced that the oscillation amplitude is maximum around $x \simeq 5$. The streamwise amplitude distribution is quantified in figure 2.9, where we plot the normalized oscillation amplitude $A(x)$ of the limit cycle along the line $r = 1$ for different values of the Reynolds number. Here, $A(x)$ was computed as

$$A = \frac{\rho_{\max} - \rho_{\min}}{\rho_{\text{avg}}}, \tag{2.28}$$

with $\rho_{\max}$, $\rho_{\min}$, and ρ_{avg} being the maximum, minimum and time-averaged value of the density oscillations at a certain position x along $r = 1$. Note that this definition is

different from that of Lesshafft *et al.* (2006), who define the amplitude as an integral of the entropy in the flow field; nevertheless, their results show a behavior similar to that reported here. The oscillation amplitude is seen to grow strongly close to the injector outlet, reaching a maximum around $x \simeq 5$, before it decays slowly downstream. The spatial evolution of the oscillations in the jet emerging with a parabolic velocity profile ($D/\theta_0 = 15$) in figure 2.9(a) is slower than that of its counterpart emerging with a steep top-hat like profile ($D/\theta_0 = 35$) in figure 2.9(b).

For $0 < x \lesssim 10$, the oscillation amplitude A decreases monotonically if the Reynolds number is decreased towards those corresponding to a globally stable flow. By tracking the oscillation amplitude A at a certain point for decreasing values of the Reynolds number Re, we can thus determine the critical Reynolds number for the onset of self-sustained oscillations as the value of Re for which $A = 0$. Nevertheless, the success of this procedure is hindered by the fact that near the bifurcation, the duration of the transient the flow goes through before the limit cycle is established becomes exponentially long. To overcome this difficulty, we can leverage the theoretical Stuart-Landau model for the Hopf bifurcation that states that in vicinity of the bifurcation, i.e. for Re slightly larger than Re_c, the square of the oscillation amplitude of the limit cycle grows linearly with the distance to the bifurcation, such that $A^2 \sim Re - Re_c$.

Once the amplitude A is known for a few values of the Reynolds number Re above the estimated value of Re_c, a linear interpolation of $A^2(Re)$ yields the value of Re_c as the root of the interpolated curve. This is shown for $D/\theta_0 = 35$ and $D/\theta_0 = 15$ in figures 2.10 (b) and (c), respectively, using data for two different points of the flow field: $(x = 1, r = 1)$ shown with blue circles, and $(x = 0.5, r = 1)$ shown with green squares. Note that here A is not normalized, i.e. $A = \rho_{\max} - \rho_{\min}$. The extrapolation procedure toward the critical Reynolds number Re_c for both positions yields values (red diamonds) that are in excellent mutual agreement, confirming the validity of the Stuart–Landau theory and the global character of the transition. For $D/\theta_0 = 15$, the value $Re_c = 575$ is obtained, whereas for $D/\theta_0 = 35$, the critical value is $Re_c = 209$.

The procedure just described was employed to obtain the critical Reynolds number for three additional values of the initial momentum thickness D/θ_0 of the jet, constructing in this manner the critical curve for the onset of self-sustained oscillations in the Re–D/θ_0 parameter plane. The results are shown as the red diamonds in figure 2.10(a), to be compared with the experimental observations of Hallberg & Strykowski (2006), indicated by the black squares, and the linear stability predictions of Coenen *et al.* (2017), indicated by the blue dots. With the exception of case with $D/\theta_0 = 15$, the results of the present direct numerical simulations are seen to lie in between those of the experiments and those of the linear stability theory, in better agreement with the former than with the latter.

As pointed out above, the critical Reynolds numbers found in this chapter lie between the experimental results of Hallberg & Strykowski (2006) and those obtained with linear stability theory by Coenen *et al.* (2017), except for the particular case $D/\theta_0 = 15$. The values of Re_c are closer to the experimental observations than to the results of linear

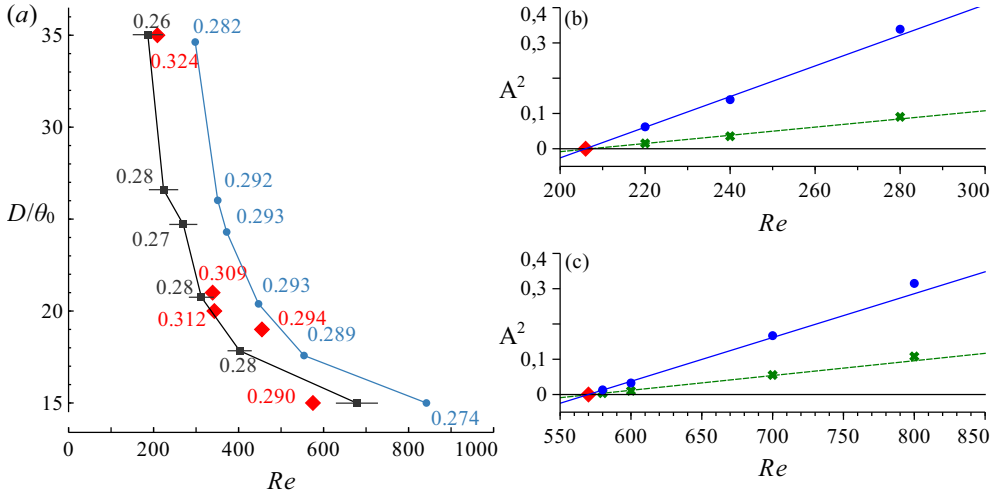

Figure 2.10: (a) Curves of marginal stability in the Re–D/θ_0 parameter plane for helium jets discharging into a nitrogen atmosphere ($S = 0.143$), separating globally stable settings on the left-hand side from globally unstable jets on the right-hand side. Red diamonds indicate the DNS results of the present work; black squares correspond to experimental results from Hallberg & Strykowski (2006); blue dots correspond to global linear stability predictions from Coenen *et al.* (2017). The numerical values next to the symbols indicate the dimensionless oscillation frequency (Strouhal number). (b) Square of the limit-cycle oscillation amplitude as a function of Re for $D/\theta_0 = 35$, at the spatial position ($x = 1, r = 1$), indicated with blue circles, and at the position ($x = 0.5, r = 1$), indicated with green squares. The red diamond indicates the value of Re_c obtained by a linear extrapolation of the data. (c) As in (b), but for $D/\theta_0 = 15$.

stability theory. This might be explained by the fact that linear theory does not take into account small perturbations due to ambient noise or numerical error that could induce a transition from stable to unstable flow at smaller Reynolds numbers. In addition, it is important to emphasize that the numerical simulations take into account non-linear effects not contemplated by the linear theory, which may also affect the critical Reynolds number.

The Strouhal numbers obtained by DNS shown in figure 2.10(a) are systematically larger than both the experimental ones taken from Hallberg & Strykowski (2006), and the linear results of Coenen *et al.* (2017). A sensitivity analysis of the DNS results should be performed to check if the domain size and the mesh resolution may affect the simulation frequencies. Such a sensitivity analysis was done for the oscillation amplitude, and was very expensive computationally. For the latter reason, a detailed analysis of the sensitivity of St to changes in domain and mesh refinement was left for future work.

According to the results discussed above, the flow is globally asymptotically stable for $Re < Re_c$, and becomes globally unstable for $Re > Re_c$ within the investigated range of momentum thicknesses $15 \leq D/\theta_0 \leq 35$. It was expected, however, that for a certain

range of Reynolds numbers below Re_c a globally stable but convectively unstable flow would be observed, in which small disturbances close to the injector would grow in the downstream direction without creating a self-sustained state. The latter scenario was indeed found by Lesshafft *et al.* (2007), but for a higher density ratio of $S = 0.65$. Interestingly, Hallberg & Strykowski (2006) show experimental pictures for two different injectors close to the critical Reynolds number, both for globally stable and globally unstable conditions. In particular, the globally stable jet is very slender and nearly steady even far away from the nozzle, without strong convective instabilities, in agreement with the numerical simulations presented in this chapter. Moreover, anticipating results from chapter 3, our axisymmetric numerical simulations do not take into account helical modes, which will be shown to dominate the linear energy gain in globally stable settings. Indeed, the axisymmetric mode will be shown to have relatively low gains for all Strouhal numbers even with an optimal forcing, indicating that convective instabilities are not expected in axisymmetric simulations, at least for the range of Reynolds numbers considered in the present study.

2.6 Conclusions and further work

The present chapter represents the first attempt to capture the transition between globally stable and globally unstable submerged laminar low-density jets by direct numerical simulations of the axisymmetric equations of motion under a realistic geometric setting. The study includes different momentum thicknesses of the outlet velocity profiles, from the fully-developed parabolic one to the top-hat like shapes associated with short tubes attached to injection nozzles.

The globally stable regimes, like that shown in figure 2.7, have been identified by the fact that initial perturbations vanish at large times, and the jet recovers the basic axisymmetric steady state. In contrast, globally unstable regimes, like that shown in figure 2.8, asymptotically reach a self-sustained oscillatory state with a well marked characteristic frequency. The numerical frequencies found in the present computations are slightly larger than those reported in the experiments of Hallberg & Strykowski (2006), and also larger than the eigenfrequencies computed by Coenen *et al.* (2017) using linear stability. Further analysis is required to find an explanation if this frequency mismatch. The streamwise distribution of the normalized oscillation amplitudes (figure 2.9) are consistent with the results of Lesshafft *et al.* (2006) for synthetic jets, reaching a maximum at $x \sim 5$, with decreasing amplitude as the Reynolds number decreases.

Our numerical simulations successfully reproduce the Hopf bifurcation towards the self-sustained unstable state described by Hallberg & Strykowski (2006) and Lesshafft *et al.* (2006), as evidenced by figure 2.10. Indeed, close to criticality, the numerical oscillation amplitudes fit the supercritical Stuart-Landau model.

The critical conditions for the onset of global instability lie between the experimentally

observed values of Hallberg & Strykowski (2006), and those predicted by the global linear stability analysis of Coenen *et al.* (2017). This fact supports the hypothesis that low-level noise in experiments and numerical simulations can prematurely trigger a transition to a globally unstable behavior. Nevertheless, a stronger proof of this hypothesis is clearly needed, and future numerical simulations imposing a harmonic forcing at the inlet could well represent a promising avenue of research along these lines. In addition, by changing the amplitude and frequency of the forcing, the response of the jet can also be compared with the results of chapter 3. However, the numerical method used in the present work is computationally expensive, and increasing the number of independent parameters in the simulations would be an extremely time-consuming task. Therefore, to that end, improved numerical methods are clearly needed to reduce the computational cost.

Several future works are proposed based on the results of the present chapter. First, it would be interesting to check the performance of the mean flow stability analysis in cases where the base flow is linearly unstable (Barkley, 2006).

In addition, three-dimensional direct numerical simulations would also provide important information about the evolution of the jet, although such a study requires substantial changes in our numerical method to be a computationally affordable task. Indeed, both mesh and time-stepping algorithm optimizations are required to fully understand the dynamical behavior of the jet under the influence of any kind of perturbations, especially non-axisymmetric ones, that have not been covered by the axisymmetric formulation employed in the present chapter.

References

BARKLEY, D 2006 Linear analysis of the cylinder wake mean flow. *EPL (Europhysics Letters)* **75** (5), 750.

BATCHELOR, G. K. & GILL, A. E. 1962 Analysis of the stability of axisymmetric jets. *J. Fluid Mech.* **14**, 529–551.

BEN-ISRAEL, ADI 1966 A newton-raphson method for the solution of systems of equations. *Journal of Mathematical Analysis and Applications* **15** (2), 243 – 252.

BÉNARD, H 1908 Formation périodique de centres de giration à l'arriére d'un obstacle en mouvement. *C. R. Acad. Sci.* (147), 839.

BROWN, GARRY L. & ROSHKO, ANATOL 1974 On density effects and large structure in turbulent mixing layers. *Journal of Fluid Mechanics* **64** (4), 775–816.

COENEN, W., LESSHAFFT, L., GARNAUD, X. & SEVILLA, A. 2017 Global instability of low-density jets. *J. Fluid Mech.* **820**, 187:207.

COENEN, W. & SEVILLA, A. 2012 The structure of the absolutely unstable regions in the near eld of low-density jets. *J. Fluid Mech.* **713**, 123–149.

COENEN, W., SEVILLA, A. & SÁNCHEZ, A. 2008 Absolute instability of light jets emerging from circular injector tubes. *Phys. Fluids* **20**, 074104.

COURANT, R., FRIEDRICHS, K. & LEWY, H. 1928 Über die partiellen differenzengleichungen der mathematischen physik. *Mathematische Annalen* **100** (1), 32–74.

GARNAUD, X., LESSHAFFT, L., SCHMID, P.J. & HUERRE, P. 2013 Modal and transient dynamics of jet flows. *Phys. Fluids* **25** (4), 044103.

HALLBERG, M. P. & STRYKOWSKI, P. J. 2006 On the universality of global modes in low-density axisymmetric jets. *J. Fluid Mech.* **569**, 493–507.

HECHT, FRÉDÉRIC 2012 New development in freefem++. *Journal of numerical mathematics* **20** (3-4), 251–266.

HUERRE, P. & MONKEWITZ, P. A. 1990 Local and global instabilities in spatially developing flows. *Annu. Rev. Fluid Mech.* **22**, 473–537.

KYLE, D. M. & SREENIVASAN, K. R. 1993 The instability and breakdown of a round variable-density jet. *J. Fluid Mech.* **249**, 619–664.

LANCZOS, CORNELIUS 1996 *Linear differential operators*. SIAM.

LECONTE, JOHN 1858 On the influence of musical sounds on the flame of a jet of coal-gas. *Philosophical Magazine* **15** (99), 235–239.

LESSEN, MARTIN & SINGH, PAWAN JIT 1973 The stability of axisymmetric free shear layers. *Journal of Fluid Mechanics* **60** (3), 433–457.

LESSHAFFT, L. & HUERRE, P. 2007 Linear impulse response in hot round jets. *Phys. Fluids* **19** (2), 024102.

LESSHAFFT, L., HUERRE, P. & SAGAUT, P. 2007 Frequency selection in globally unstable round jets. *Phys. Fluids* **19** (5), 054108.

LESSHAFFT, L., HUERRE, P., SAGAUT, P. & TERRACOL, M. 2006 Nonlinear global modes in hot jets. *J. Fluid Mech.* **554**, 393–409.

LESSHAFFT, LUTZ & MARQUET, OLIVIER 2010 Optimal velocity and density profiles for the onset of absolute instability in jets. *Journal of Fluid Mechanics* **662**, 398–408.

LIDE, DAVID R 2001 Crc handbook of physics and chemistry. *CRC Press, Boca Raton, USA* **76**, 1995–1996.

MICHALKE, ALFONS 1970 A note on the spatial jet-instability of the compressible cylindrical vortex sheet. *Tech. Rep.*. Deutsche Forschungs-und Versuchsanstalt für Luft- und Raumfahrt.

MONKEWITZ, P. A., BECHERT, D. W., BARSIKOW, B. & LEHMANN, B. 1990 Self-excited oscillations and mixing in a heated round jet. *J. Fluid Mech.* **213**, 611–639.

MONKEWITZ, PETER A. & SOHN, KIHOD. 1988 Absolute instability in hot jets. *AIAA Journal* **26** (8), 911–916.

NICHOLS, J & LELE, S 2010 Global mode analysis of turbulent high-speed jets. *Annual Research Briefs* .

NICHOLS, J. W., SCHMID, P. J. & RILEY, J. J. 2007 Self-sustained oscillations in variable-density round jets. *J. Fluid Mech.* **582**, 341–376.

QADRI, UBAID ALI & SCHMID, PETER J. 2017 Effect of nonlinearities on the frequency response of a round jet. *Physical Review Fluids* **2** (4), 1–14.

SREENIVASAN, KR, STRYKOWSKI, PJ & OLINGER, DJ 1987 Hopf bifurcation, landau equation, and vortex shedding behind circular cylinders. In *Forum on unsteady flow separation*, , vol. 1, pp. 1–13. American Society for Mechanical Engineers, Fluids Engineering Division New York.

TYNDALL, JOHN 1867 On sounding and sensitive flames. *Philosophical Magazine* **33** (221), 92–99.

VON KARMAN, T 1908 Ueber den mechanismus des widerstandes, den ein bewegter körper in einer flüssigkeit erfährt. *Gottingen Nachr. Math. Phys. Kl.* (12), 509.

WILLIAMS, F. A. 1985 Comment. *Combustion Science and Technology* **43** (5-6), 329–332.

CHAPTER

THREE

Global frequency response analysis of axisymmetric laminar jets

Contents

This chapter presents a numerical study of the linear global frequency response of submerged axisymmetric jets emerging from a circular tube into a infinite ambient at rest. One of the main goals is to find a critical Reynolds number based on the kinetic energy gain of small disturbances introduced in the form of a harmonic forcing of the laminar base flow with optimal and uniformly distributed perturbations. The results obtained will be compared with the available literature. All the reported calculations were performed with `FreeFEM++`, used to compute the axisymmetric base flows with the same procedure explained in chapter 2, as well as all the matrices needed in the linearized analysis, together with home-made MATLAB® scripts that computed the global frequency response of these base flows for several azimuthal modes, contemplating both uniform and optimal forcing structures restricted inside the injection pipe.

The need to contemplate non-axisymmetric modes is motivated by several previous works like Mollendorf & Gebhart (1973), who found that the first helical mode, $m = \pm 1$, was the most unstable one in their local stability analysis of buoyant jets. The same fact had been previously pointed out by Crow & Champagne (1971) in their introduction. The direct numerical simulations in the laminar regime performed by Danaila *et al.* (1997) also revealed this dominance of helical structures in transitional jets. More recently, both the linear frequency response analysis of Garnaud *et al.* (2013), and the weakly nonlinear

frequency response analysis of Qadri & Schmid (2017) showed that, both for turbulent mean flows and laminar base flows, respectively, non-axisymmetric modes $|m| \neq 0$ are dominant with respect to the axisymmetric one in a wide range of forcing frequencies.

The present chapter starts with a brief literature review, followed by a presentation of the mathematical formulation and the numerical techniques employed to solve the equations. Then, a discussion of the results is presented and, finally, several conclusions are drawn and future developments are suggested.

3.1 Introduction

Jet flows, either constant-density or low-density ones, are highly sensitive to perturbations. As described in chapter 2, these kind of flows may be globally unstable and develop self-sustained oscillations when the jet-to-ambient density ratio is small enough and the Reynolds number large enough, or they may be globally stable and act as noise amplifiers. In the latter case, which is the subject of the present chapter, high-Reynolds-number jets exhibit large amplification gains within a certain frequency range and respond with a preferred frequency, as evidenced for instance by Tyndall (1867*b*), who studied the influence of sound at moderately large values of the Reynolds numbers both with flames and jets (Tyndall, 1867*a*). A precise knowledge of these amplification characteristics of jets has important applications in industry either to preserve laminar flow or to trigger turbulent flow to enhance transport and mixing.

The first works on the stability of two-dimensional jets were done in the context of local stability theory by Pai (1951), who considered compressible and incompressible flows, symmetric and antisymmetric perturbations, with inviscid and viscous disturbances. He found that symmetric and antisymmetric disturbances are both unstable at large Reynolds numbers. He also revealed that the effect of viscosity is always stabilizing. Later on, his works was extended by Tatsumi & Kakutani (1958), who computed the neutral curve of parallel two-dimensional jets in the wavenumber versus Reynolds number plane.

The parallel stability analysis of round jets was pioneered by Batchelor & Gill (1962), who applied local inviscid theory to incompressible constant-density jets. Jets with uniform velocity profiles were found to be unstable for all azimuthal modes m, while the self-similar velocity profile that is reached in their far field was found to be stable for the axisymmetric mode, but unstable for non-axisymmetric modes, being the helical mode, $|m| = 1$, the dominant one.

In the same decade Reynolds (1962) performed experiments with nearly constant density jets using dyed liquid to find the critical Reynolds number by flow visualization. He found that a dyed water jet discharging into a large water tank exhibited different states depending on the Reynolds number based on the injector diameter, Re_D. For $10 < Re_D < 30$ a steady jet was observed. For $30 < Re_D < 150$, long steady jets were

appreciated with some axisymmetric condensations due to background disturbances. For $150 < Re_D < 300$, long-wavelength sinuous disturbances appeared and a complex breakdown took place downstream. For $Re_D > 300$, disordered flow was observed near the nozzle.

In the same year, Viilu (1962) also studied the transition from stable to unstable flow in round jets of water discharging into a water ambient. He described four kinds of states: an unstable one with steady flow close to nozzle that developed ring vortices; a slightly unstable one when the flow was steady but with intermittent ripples close to nozzle; a marginally stable one when the flow displayed small perturbations such as beats of vibrations that created waves taking a long time to vanish; and finally, a stable state when all disturbances were observed to disappear fast. According to these observations, the critical Reynolds number reported by Viilu (1962) was $Re_D \approx 11$.

Later on, Kambe (1969) performed a parallel temporal stability analysis of jets with parabolic velocity profiles for viscous and inviscid disturbances. He found that axisymmetric viscous disturbances are stable at moderate Reynolds numbers, while non-axisymmetric inviscid disturbances are unstable.

Several years later, the amplification of disturbances induced by external forcing was studied experimentally by Crow & Champagne (1971) in turbulent air jets discharging into air, revealing that the highest response took place at a Strouhal number $St \approx 0.3$ based on the nozzle diameter. These perturbations grow downstream of the nozzle exit until they become non-linear.

Mollendorf & Gebhart (1973) analyzed the parallel stability of laminar buoyant jets in the range of Reynolds numbers $138 < Re_D < 537$. They found that non-axisymmetric modes were dominant. The spatial and temporal stability properties of jets and wakes were studied by Lessen & Singh (1973) both for viscous and inviscid disturbances, including velocity profiles in their self-similar regions. These authors reported the existence of very small critical Reynolds numbers using parallel stability theory, and pointed out that their results were thus inconsistent, since the base flow is far from parallel for such low values of the Reynolds number. Morris (1976) analyzed, using parallel spatial stability analysis, the influence of three different velocity profiles going from top-hat like to the self-similar far-field profile.

Danaila *et al.* (1997) studied coherent structures in laminar round jets at low Reynolds number using three-dimensional direct numerical simulations, finding the dominance of helical disturbances with a Strouhal number $St \approx 0.3$. He also found instabilities at Reynolds number $Re_D = 200$ at Strouhal number $St = 0.169$.

Using a global approach, Garnaud *et al.* (2013) analyzed the linear frequency response of a turbulent axisymmetric constant-density jet using a model mean flow, focusing on the optimal response of the axisymmetric mode, $m = 0$. In addition, for one particular case these authors reported a comparison between the modes $m = 0, \pm 1$ and ± 2, showing that, for a wide range of frequencies the most amplified mode is, the helical one, $m = \pm 1$.

However, Garnaud *et al.* (2013) restricted their results to a model turbulent mean flow of constant density, and did not perform a systematic parametric study of non-axisymmetric modes, $m \neq 0$.

In a recent work, Qadri & Schmid (2017) studied the linear and weakly non-linear frequency response of laminar axisymmetric jets of uniform density for the first three azimuthal modes. However, these authors only considered the optimal forcing, and restricted the forcing to the radial velocity component with spatial support within a small annular region close to the injector outlet.

Therefore, the objective of this chapter is to analyze the linear frequency response of globally stable laminar axisymmetric jets that discharge into a quiescent ambient, considering both optimal and uniform forcing, and contemplating the azimuthal modes $m = 0, \pm 1$ and ± 2. Higher-order azimuthal modes are disregarded, since they are subdominant. Two different kinds of outlet velocity profiles are also considered, namely the fully developed Poiseuille profile, and a top-hat like profile. In addition, besides the Reynolds number, we also consider the influence of the jet-to-ambient density ratio, that is changed from the helium-air value of $S = 0.143$, to the constant-density case, $S = 1$. To provide o more complete picture, an intermediate case with density ratio $S = 0.5$ is also included in appendix B. In contrast with Garnaud *et al.* (2013), that considered a model turbulent mean flow as base flow, the present work uses a laminar jet as base state, computed as a steady solution of the governing equations. Moreover, although Qadri & Schmid (2017) also used a laminar base flow, they only considered the optimal forcing of the radial velocity component inside an arbitrary region of the domain close to the pipe exit. In contrast, here we consider the forcing of all the velocity components with a spatial support inside the whole injection pipe. A brief comparison will also be made with an extended forcing region.

3.2 Flow configuration

We consider an axisymmetric laminar jet that discharges from a circular pipe at a constant flow rate Q^* into a stagnant ambient. The nozzle has a radius R^* and the injection pipe, of length L^*_{pipe}, ends with the knife-edge configuration that can be seen in figure 3.1. A cylindrical coordinate system is used (x^*,r^*) with origin (0,0) centered at the exit of the injector. The jet fluid has density ρ^*_j and and viscosity μ^*_j, while the ambient fluid has density ρ^*_∞ and and viscosity μ^*_∞. The axial and radial velocity components are defined as $\boldsymbol{u}^* = (u^*, v^*)$, respectively. The jet-to-ambient density ratio is defined as

$$S = \rho^*_j / \rho^*_\infty. \tag{3.1}$$

Note that the flow configuration is basically the same considered in chapter 2, with the exception that non-axisymmetric modes are considered in the present chapter.

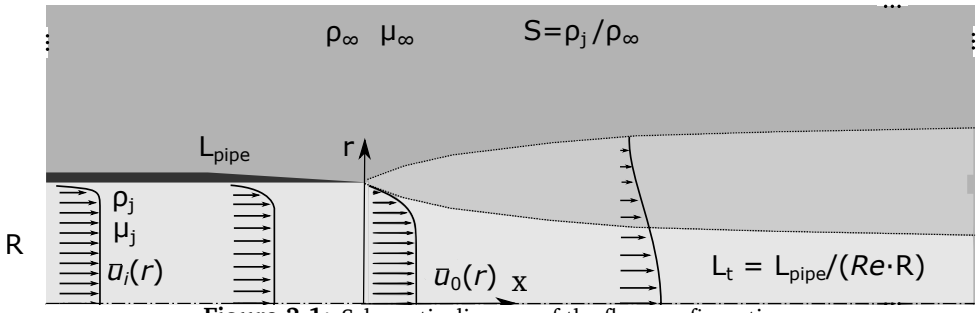

Figure 3.1: Schematic diagram of the flow configuration.

Lengths, densities and velocities are scaled with the jet radius R^*, the jet density ρ_j^* and the mean outlet velocity $U_m^* = 4Q^*/(\pi R^{*2})$. The Reynolds number is defined as

$$Re = \rho_j^* U_m^* R^* / \mu_j^*, \tag{3.2}$$

The shape of the outlet velocity profile $u_0^*(r)$ depends on the length of the pipe, L_{pipe}^*. In appendix A we describe the methodology used to obtain the desired outlet velocity profile, which follows the works of Coenen *et al.* (2008) and Coenen & Sevilla (2012). The steepness of the velocity profile is measured by the momentum thickness,

$$\theta_0 = \int_0^\infty \frac{u_0^*(r)}{u_0^*(0)} \left[1 - \frac{u_0^*(r)}{u_0^*(0)} \right] \mathrm{d}r, \tag{3.3}$$

with dimensionless counterpart $D/\theta_0 = 2R^*/\theta_0$, such that top-hat like velocity profiles correspond to large values of D/θ_0, while the parabolic Poiseuille profile has an associated value of $D/\theta_0 = 15$ (see appendix A).

Buoyancy effects will be neglected, as corresponds to the small values assumed for the Richardson number, $Ri = (\rho_\infty^* - \rho_j^*) g^* R^* / (\rho_j^* U_m^{*\,2}) \ll 1$. Indeed, Coenen *et al.* (2017) showed that the global modes are only slightly affected if realistic values of $Ri \ll 1$ are used in the analysis, compared to making the buoyancy-free approximation $Ri = 0$.

As in chapter 2, we assume small values of the Mach number, $Ma = U_m^*/c^*$ being c^* the speed of sound in the jet, providing the same low-Mach-number approximation of the governing equations formulated in chapter 2. We remind the reader that this formulation only takes into account density variations due to the mixing of gases with different molecular weight. Also, it implies that the jet is isothermal and that the energy equation is not need in the description. The variable p incorporates the viscous stresses which are proportional to the second coefficient of viscosity, and is scaled with the dynamic pressure $\rho_j^* U_m^{*\,2}$. The resulting dimensionless conservation equations are

$$\frac{\partial \rho}{\partial t} + \nabla \cdot \left(\rho \boldsymbol{u}\right) = 0, \tag{3.4}$$

$$\rho\left(\frac{\partial \boldsymbol{u}}{\partial t} + \boldsymbol{u} \cdot \nabla \boldsymbol{u}\right) = -\nabla p + \frac{1}{Re}\nabla^2 \boldsymbol{u}, \tag{3.5}$$

$$\rho\left(\frac{\partial Y}{\partial t} + \boldsymbol{u} \cdot \nabla Y\right) = \frac{1}{Re\,Sc}\nabla \cdot \left(\rho \nabla Y\right), \tag{3.6}$$

where $Y = Y_j(1/\rho - S)/(1-S)$, $Y_j = (1/S-1)/(W_{He-N_2}-1)$ and the Schmidt number, Sc, is defined as

$$Sc = \frac{\mu_j^*}{\rho_j^* D^*} = \frac{1}{S}\frac{W_{He}}{W_{N_2}}\frac{\mu_j}{\mu_{He}} Sc_{He-N_2}. \tag{3.7}$$

Note that the Schmidt number associated to the helium-nitrogen diffusion is $Sc_{He-N_2} = 1.69$, that the corresponding ratio of molecular weights is $W_{He}/W_{N_2} = 0.143$. On the other hand, the jet-to-helium viscosity ratio, $\frac{\mu_j}{\mu_{He}}$, is defined according to Hirschfelder *et al.* (1954) as

$$\frac{\mu_j}{\mu_{He}} = \left(1 + 1.385 \cdot Sc_{He-N_2}\frac{W_{He}}{W_{N_2}}\frac{1-Y_j}{Y_j}\right)^{-1} + \left(\frac{\mu_{He}}{\mu_{N_2}} + 1.385 \cdot Sc_{He-N_2}\frac{Y_j}{1-Y_j}\right)^{-1}, \tag{3.8}$$

where the helium-nitrogen viscosity ratio $\mu_{\mathrm{He}}/\mu_{\mathrm{N}_2} = 1.11$.

Equations (3.4)–(3.6) are subjected to the following boundary conditions. For $x = 0$ and $r \leq 1$, the velocity profile is the prescribed injector outlet profile, $u = u_0(r)$, $v = 0$, which depends on the value of D/θ_0; the density is related with the density-ratio S. In the far field, $x^2 + r^2 \to \infty$, the fluid is at rest, $(u, v) \to 0$, and the density is that of the ambient, $\rho \to 1/S$. Finally, no-slip conditions $u = v = 0$ are imposed at the walls, where $r \geq 1$ and $x \leq 0$.

3.3 Global modes and response to harmonic forcing

In this section the global mode decomposition is first described, followed by the formulation of the response of the jet to harmonic forcing.

3.3.1 Modal decomposition

To perform the linear analysis, equations (3.4) – (3.6) are decomposed into a steady base flow plus a small perturbation,

$$(u, v, w, \rho, p) = (\overline{u}, \overline{v}, 0, \overline{\rho}, \overline{p}) + \varepsilon(u', v', w', \rho', p'), \tag{3.9}$$

where small perturbations are represented as global modes with time-harmonic dependence,

$$(u', v', w', \rho', p') = (\widehat{u}, \widehat{v}, \widehat{w}, \widehat{p}, \widehat{\rho})e^{i\omega t}, \tag{3.10}$$

being ω the eigenvalue and $\widehat{u}, \widehat{v}, \widehat{w}, \widehat{p}, \widehat{\rho}$ the associated eigenfunctions. Notice that although the base flow is axisymmetric $\overline{w}$, non-axisymmetric perturbations are contemplated, with associated azimuthal velocity eigenfunctions $\widehat{w}$.

After substituting the modal decomposition in equations (3.4) – (3.6) and neglecting second order terms in the amplitude ε, the linearized modal equations are obtained: (3.11) is the mass conservation equation, (3.12) the axial momentum equation, (3.13) the radial momentum equation, (3.14) the azimuthal momentum equation and (3.15) the species conservation equation.

$$\begin{aligned}
-i\omega\widehat{\rho} = &-\overline{\rho}\left(\partial_x\widehat{u} + \partial_r\widehat{v} + \frac{\widehat{v}}{r} + \frac{im}{r}\widehat{w}\right) \\
&-\widehat{\rho}\left(\partial_x\overline{u} + \partial_r\overline{v} + \frac{\overline{v}}{r}\right) - \overline{u}\partial_x\widehat{\rho} - \overline{v}\partial_r\widehat{\rho} - \widehat{u}\partial_x\overline{\rho} - \widehat{v}\partial_r\overline{\rho}, \qquad (3.11)\\
-i\omega\overline{\rho}\widehat{u} = &-\overline{\rho}\left(\overline{u}\partial_x\widehat{u} + \overline{v}\partial_r\widehat{u} + \widehat{u}\partial_x\overline{u} + \widehat{v}\partial_r\overline{u}\right) - \widehat{\rho}\left(\overline{u}\partial_x\overline{u} + \overline{v}\partial_r\overline{v}\right) \\
&-\partial_x\widehat{p} + \frac{1}{Re}\left(\nabla_*^2\widehat{u} - \frac{m^2}{r^2}\widehat{u}\right), \qquad (3.12)\\
-i\omega\overline{\rho}\widehat{v} = &-\overline{\rho}\left(\overline{u}\partial_x\widehat{v} + \overline{v}\partial_r\widehat{v} + \widehat{u}\partial_x\overline{v} + \widehat{v}\partial_r\overline{v}\right) - \widehat{\rho}\left(\overline{u}\partial_x\overline{v} + \overline{v}\partial_r\overline{v}\right) \\
&-\partial_r\widehat{p} + \frac{1}{Re}\left(\nabla_*^2\widehat{v} - \frac{1+m^2}{r^2}\widehat{v} - \frac{2im}{r^2}\widehat{w}\right), \qquad (3.13)\\
-i\omega\overline{\rho}\widehat{w} = &-\overline{\rho}\left(\overline{u}\partial_x\widehat{w} + \overline{v}\partial_r\widehat{w} + \frac{\overline{v}\widehat{w}}{r}\right) \\
&-\frac{im}{r}\widehat{p} + \frac{1}{Re}\left(\nabla_*^2\widehat{w} - \frac{1+m^2}{r^2}\widehat{w} + \frac{2im}{r^2}\widehat{v}\right), \qquad (3.14)\\
-i\omega\overline{\rho}\widehat{Y} = &-\overline{\rho}\left(\overline{u}\partial_x\widehat{Y} + \overline{v}\partial_r\widehat{Y} + \widehat{u}\partial_x\overline{Y} + \widehat{v}\partial_r\overline{Y}\right) - \widehat{\rho}\left(\overline{u}\partial_x\overline{Y} + \overline{v}\partial_r\overline{Y}\right) \\
&+\frac{1}{Re\,Sc}\left(\nabla_*\cdot\left(\overline{\rho}\nabla_*\widehat{Y} + \widehat{\rho}\nabla_*\overline{Y}\right) - \overline{\rho}\frac{m^2}{r^2}\widehat{Y}\right), \qquad (3.15)
\end{aligned}$$

where the mathematical operators in the (x, r) plane are

$$\nabla_*^2 \varphi = \partial_{xx}\varphi + \partial_{rr}\varphi + \frac{1}{r}\partial_x \varphi, \tag{3.16}$$

$$\nabla_* \varphi = \partial_x \varphi \boldsymbol{e_x} + \partial_r \varphi \boldsymbol{e_r}, \tag{3.17}$$

$$\nabla_* \cdot \varphi = \partial_x \varphi_x + \partial_r \varphi_r + \frac{1}{r}\varphi_r. \tag{3.18}$$

The boundary conditions for the eigenfunctions depend on the azimuthal mode, as described e.g. in Batchelor & Gill (1962),

$$m = 0 \begin{cases} \partial_r \widehat{u} = \widehat{v} = \widehat{w} = 0 \text{ on } \Gamma_a, \\ \widehat{u} = \widehat{v} = \widehat{w} = 0 \text{ on } \Gamma_w, \\ \widehat{u} = \widehat{v} = \widehat{w} = \widehat{\rho} = 0 \text{ on } \Gamma_i, \\ -\widehat{p}\boldsymbol{n} + \boldsymbol{n}/Re \cdot \nabla(\widehat{u}, \widehat{v}, \widehat{w}) = 0 \text{ on } \Gamma_o, \Gamma_t \end{cases}$$

$$|m| = 1 \begin{cases} \widehat{u} = \widehat{w} = \widehat{\rho} = \widehat{p} = 0 \text{ on } \Gamma_a, \\ \widehat{u} = \widehat{v} = \widehat{w} = 0 \text{ on } \Gamma_w, \\ \widehat{u} = \widehat{v} = \widehat{w} = \widehat{\rho} = 0 \text{ on } \Gamma_i, \\ -\widehat{p}\boldsymbol{n} + \boldsymbol{n}/Re \cdot \nabla(\widehat{u}, \widehat{v}, \widehat{w}) = 0 \text{ on } \Gamma_o, \Gamma_t \end{cases}$$

$$|m| > 1 \begin{cases} \widehat{u} = \widehat{v} = \widehat{w} = \widehat{\rho} = \widehat{p} = 0 \text{ on } \Gamma_a, \\ \widehat{u} = \widehat{v} = \widehat{w} = 0 \text{ on } \Gamma_w, \\ \widehat{u} = \widehat{v} = \widehat{w} = \widehat{\rho} = 0 \text{ on } \Gamma_i, \\ -\widehat{p}\boldsymbol{n} + \boldsymbol{n}/Re \cdot \nabla(\widehat{u}, \widehat{v}, \widehat{w}) = 0 \text{ on } \Gamma_o, \Gamma_t \end{cases}$$

The linearized equations (3.11) – (3.15) can be written as a generalized eigenvalue problem,

$$-(L + i\omega B)\widehat{q} = 0, \tag{3.19}$$

where $\widehat{q}$ is the vector of eigenfunctions, L and B are matrix operators. All the matrices are assembled using `FreeFEM++` and MUMPS (see Amestoy *et al.* (2000)), and the resulting algebraic eigenvalue problem solved in MATLAB® using ARPACK libraries (see Lehoucq *et al.* (1998)). The eigenvalue calculation implies an LU decomposition (see Lanczos (1996)) to invert the shifted system

$$P_O \, A \, Q_O = L_O \, U_O \tag{3.20}$$

where A is the matrix to decompose, and P_O, Q_O, L_O and U_O are, respectively, the permutation matrix, the column reordering matrix, the lower triangular matrix and the upper triangular matrix for sparse non-empty A.

3.3.2 Harmonic forcing

Once the modes are calculated, we can add to the linear system a forcing function f and a distribution matrix B_f which includes a weight function $\phi(x,r)$ defined as $\phi(x,r)=1$ when $x<0$ and $0<r<1$, and $\phi(x,r)=0$ for the other coordinates, limiting the forcing f to a specific region of the computational domain.

Except otherwise stated, throughout this chapter the forcing region was set inside the pipe with length 2 and 1 radius. The forcing can be decomposed as the harmonic function $f=\widehat{f}e^{i\omega t}$, using the same definition as Garnaud *et al.* (2013) having finally the system

$$-(L+i\omega B)\widehat{q}=B_f\widehat{f}, \tag{3.21}$$

After it is solved, the gain or amplification of the forcing applied at a specific frequency ω is calculated as

$$G(\omega)=max\left(\frac{\int_\Omega |\,\widehat{u}\,|^2\,rdrdx}{\int_\Omega |\,\widehat{f}\,|^2\,rdrdx}\right). \tag{3.22}$$

The square of the gain can also be defined as the ratio between the response norm and the forcing norm,

$$G^2(\omega)=\frac{||\widehat{q}||^2}{||\widehat{f}||^2}=\frac{||(L+i\omega B)^{-1}B_f\widehat{f}||^2}{||\widehat{f}||^2}=\frac{\widehat{f}^H B_f^H(L+i\omega B)^{-H}Q(L+i\omega B)^{-1}B_f\widehat{f}}{\widehat{f}^H Q\widehat{f}}, \tag{3.23}$$

where the superscript H denotes the transpose-conjugate of a vector or matrix. This methodology to compute the gain function was also used by Garnaud *et al.* (2013) and by Qadri & Schmid (2017).

Here we will distinguish between two different kinds of gains: the optimal gain, G_{opt}, when $\widehat{f}$ is obtained as the forcing distribution inside the chosen region that maximizes the gain among all the possible forcing structures. It is constructed as decomposition of the singular values of the global resolvent as it is deeply explained in Sipp & Marquet (2013). And the uniform gain, G_{uni}, when the forcing function is uniform inside the chosen region. It is calculated setting the forcing vector $\widehat{f}$ to unity.

Here we will adopt the following criterion to distinguish between unstable and stable jets: if the gain is smaller than one for all values of the forcing frequency, the jet is considered stable. However, if there are frequencies for which the gain is larger than one, then the jet is considered unstable. Note that this criterion is very conservative, since the observability of unstable structures depends not only on the kinetic energy gain, but also on the kinetic energy of the forcing disturbances.

3.4 Numerical method

The finite element method was used to discretized the equations using the `FreeFEM++` code in its version 3-35, as described in subsection 2.4.1. More details about this software can be found in Hecht (2012) and the `FreeFEM++` manual. The procedure followed to compute the steady solutions is the same one described in subsection 2.4.3. Once the steady jet has been obtained, we apply home-made MATLAB® scripts to compute the frequency response making use of the matrix operators provided by the `FreeFEM++` codes.

3.4.1 Computational mesh

The finite-element mesh used for the numerical integrations is similar to that described in chapter 2, as can be seen in Figure 3.2 for a numerical injector pipe of length $x_p = 2$. Again, regions of increased refinement were incorporated, as indicated with different tones of grey, to properly capture the shear-layer region that appears downstream from the injector exit. In the figure, numbers inside the squares indicate the typical triangle size h. A value of $h_1 = 0.6$ was used for the outer mesh, while the successive refinements correspond to $h_2 = 0.12$, $h_3 = 0.06$ and $h_4 = 0.012$ from outside to inside.

This mesh configuration is similar to that used by Coenen *et al.* (2017). It was ensured that the results were independent of mesh refinement and domain size. For the azimuthal modes $m = 0$ and $m = 2$ it was found that a value of $x_{\max} = 60$ was enough for low Reynolds numbers, and $x_{\max} = 120$ for high Reynolds numbers, while for $m = 1$ a minimum of $x_{\max} = 500$ is needed to obtain converged solutions at small frequencies due to the long associated wavelengths of the response. The radial extent of the domain was always $r_{\max} = 10$ in all the reported results. The total number of vertices goes from 70,000 to 400,000.

The boundary conditions used in the base flow computations are as follows. At the injector inlet, Γ_i, $u = u(r)$, $v = 0$, $w = 0$ and $\rho = 1$ where $u(r)$ is an imposed velocity profile such that velocity profile at the outlet of the pipe has the desired value of D/θ_0, as described in chapter 2. Along the axis Γ_a, $v = 0$ and $w = 0$ to impose axisymmetry. At the walls, Γ_w, no-slip condition is applied, $u = v = w = 0$. Finally, at the lateral Γ_t and outlet boundaries, Γ_o, stress-free conditions are applied,$-p\boldsymbol{n} + Re^{-1}\boldsymbol{n}\cdot\nabla\boldsymbol{u} = 0$ while the density $\rho = 1/S$ and $\partial\rho/\partial x = 0$.

3.5 General procedure and expected outcome

The main goal of this chapter is to compute the linear frequency response of globally stable jets as a function of the Reynolds number, Re, for several combinations of the remaining parameters, such as the density ratio S, which takes the three values $S = 0.14$, $S = 1$ and

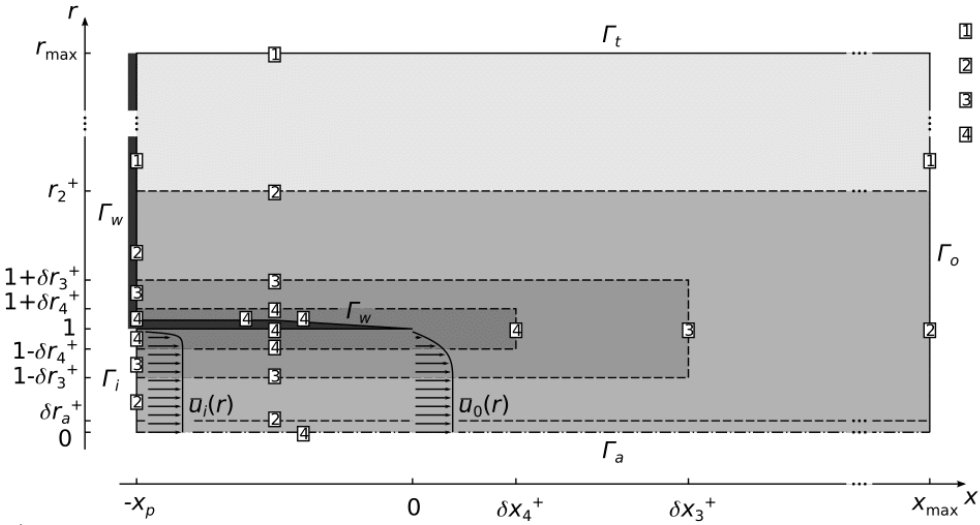

Figure 3.2: Physical configuration of the problem. Numbers inside the boxes indicates the refinement region h_i represented in grey scale. Boxes have same size as mesh of chapter 2.

$S = 0.5$, two different values of the dimensionless momentum thickness parameter D/θ_0, namely $D/\theta_0 = 15$ and $D/\theta_0 = 35$, and considering the azimuthal modes $m = 0, \pm 1$ and ± 2.

Another relevant contribution of the present chapter is the computation of a critical Reynolds number of submerged jets based on the kinetic energy gain. Indeed, since the gain is defined as the ratio of the kinetic energy of the response to that of the forcing, perturbations will grow when such gain is larger than one, what constitutes the criterion applied herein to define the critical Reynolds number. Each azimuthal mode will be characterized by a different critical Reynolds number, being the dominant mode the one with the smallest value of the critical Reynolds number. The forcing structure and its spatial support will affect these results. Indeed, it can be anticipated that optimal forcings and large spatial supports will have higher gains than uniform forcings and small spatial supports, affecting also the resulting value of the critical Reynolds number.

It is important to emphasize that Reynolds numbers larger than those predicted by the global linear theory for the transition to globally unstable flow will not be taken into account in the present study, since in those cases the jet behaves as a self-excited oscillator. The range of Reynolds numbers considered herein goes from about 100 to 1000, as suggested by the results of previous works (Coenen *et al.*, 2017; Hallberg & Strykowski, 2006; Mollendorf & Gebhart, 1973; Reynolds, 1962; Viilu, 1962).

3.6 Results

In this section, we present the results of the global frequency response analysis, in which the response of the submerged jet to harmonic forcing is assessed. Both the cases of a uniform forcing inside the injector tube, as the so-called optimal forcing, i.e. the forcing that produces the largest response, are considered. Note that in the latter case the spatial structure of the forcing is not known a priori, and must be obtained as part of the computation, as explained in section 3.3.2. We first compare the gains induced by forcings of different types, distinguishing in particular between axisymmetric and helical modes. This is followed by a discussion of the spatial structure of the response. Finally, we present a comparison between jets emerging from pipes and jets emerging from wall orifices, in addition to a study of the influence of the size of the forcing region on the jet response.

3.6.1 Frequency response analysis I: Energy gain and critical Reynolds number

Let us begin by presenting a comparison of the optimal frequency responses for different azimuthal numbers. Figure 3.3 shows the optimal gains associated with azimuthal modes $m = 0, \pm1, \pm2, \pm3$ as a function of the Strouhal number for a light jet with a density ratio $S = 0.5$, Reynolds number $Re = 500$, an outlet velocity profile with momentum thickness $D/\theta_0 = 24.7$, and different domain lenghts, as indicated in the legend. The axisymmetric mode $m = 0$ displays a maximum gain at $St \approx 0.45$. The mode $m = \pm2$ has a maximum at $St \approx 0.2$. The latter mode has larger gains than the axisymmetric one below a certain value of St, but at higher values of St the axisymmetric mode has larger gains. It is also deduced that the mode $m = \pm3$ has smaller gains than the mode $m = \pm2$ for all the frequency range, and thus modes with $|m| > 2$ will not be considered in the remainder of the chapter. Note also that the gains of all the azimuthal modes discussed above are independent of the domain length beyond a minimum length of 60. In contrast, the first helical mode, $m = \pm1$, is strongly influenced by the domain length at small values of St, precisely where it displays its maximum gain. This dependence is related to the fact that small values of St have long associated wavelengths, as will be seen below when the spatial structure of the response is presented. By comparing the results obtained for different domain lengths, it is deduced that to achieve a fairly converged gain for the mode $m = \pm1$, a domain length between 400 and 500 is needed, providing a maximum at a value of $St \simeq 0.03$. Longer domains could not be contemplated in the present work due to computational limitations.

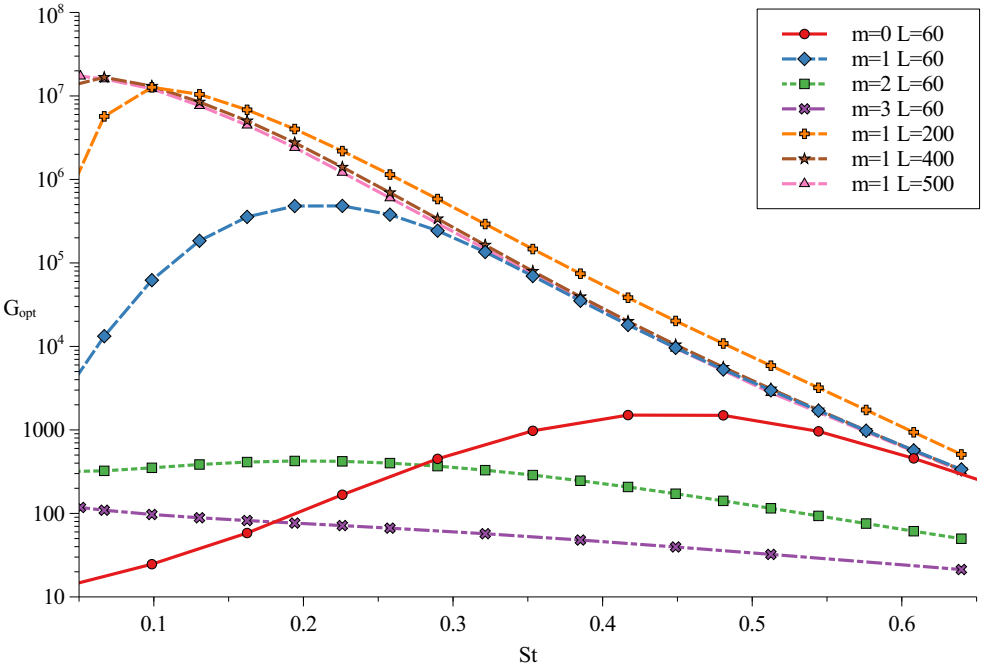

Figure 3.3: Comparison of the frequency response curves for several azimuthal modes and domain lengths, indicated in the legend, for a jet with $S = 0.5$, $Re = 500$ and $D/\theta_0 = 24.7$.

3.6.1.1 Low-density helium-nitrogen jets

Figures 3.4 and 3.5 show the optimal (left panels) and uniform (right panels) gains of helium-nitrogen jets, $S = 0.14$, at a Reynolds number $Re = 200$, for a parabolic outlet profile with $D/\theta_0 = 15$ in figure 3.4, and for a top-hat profile with $D/\theta_0 = 35$ in figure 3.5.

In figure 3.4, it can be seen that the first helical mode $m = \pm 1$ (blue dashed line) has the maximum gain by 4 orders of magnitude compared with the maximum gain of the other two modes, both for optimal and uniform forcing. It is also deduced that the optimal gain is approximately 2 orders of magnitude larger than the uniform forcing. The axisymmetric mode (red solid line) presents a maximum at $St \approx 0.3$, while non-axisymmetric modes have their maximum gains at smaller Strouhal numbers. Another interesting observation is that, for $m = 0$, the jet is unstable under optimal forcing conditions, but stable for the uniform forcing, since the gain is smaller than one for all frequencies in the latter case. Moreover, for $St > 0.4$ and optimal forcing, the modes $m = \pm 2$ and $m = \pm 1$ have approximately the same gain, but for uniform forcing, $m = \pm 2$ has larger gain than $m = \pm 1$, in both cases below unity.

The results of figure 3.5 reveal that the gains of mode $m = \pm 1$ for top-hat-like outlet velocity profiles, $D/\theta_0 = 35$, are slightly smaller than those associated with the parabolic

profile. In contrast, modes $m = 0$ and $m = \pm 2$ have much larger gains in the case of the top-hat profile for optimal forcing (figure 3.5a), and slightly larger in the case of uniform forcing (figure 3.5b). The axisymmetric mode, $m = 0$, presents a maximum at $St \approx 0.3$, while the mode $m = \pm 2$ has a maximum at $St \approx 0.1$.

As have been seen in figures 3.4 and 3.5, the modes $m = 0$ and $m = \pm 2$ have larger maximum gains for top-hat like profiles than for the parabolic profile, while the reverse is true for the helical $m = \pm 1$ mode, independently of the type of forcing.

In figure 3.6 the maximum of the gain for each mode is represented at several Reynolds numbers for parabolic profiles and helium-nitrogen jet, $S = 0.14$. The helical mode $m = \pm 1$ (blue diamonds) has larger gains than modes $m = 0$ (red dots) and $m = \pm 2$ (green squares), both for optimal (left panel) and uniform (right panel) types of forcing.

For the first helical mode, $m = \pm 1$, the transition from stable to unstable flow, associated with gains smaller and larger than one, respectively, takes place for a Reynolds number $Re \approx 8$ in the case of optimal forcing, and $Re \approx 55$ for uniform forcing. On the other hand, modes $m = 0$ and $m = \pm 2$ have the transition for optimal forcing at $Re \approx 15$ being the gain for $m = \pm 2$ slightly larger than that for $m = 0$ at low and moderate Reynolds numbers, while the opposite behavior is observer at high Reynolds numbers. A similar scenario takes place in the case of uniform forcing, but with larger values of the critical Reynolds number, namely $Re \approx 200$ for $m = \pm 2$, and $Re \approx 450$ for $m = 0$. The vertical dashed lines mark the limits for the onset of global instability calculated by Coenen *et al.* (2017). Note that it makes no sense to compute the gain above these limits, since the base flow is globally unstable.

Figure 3.7 shows the maximum gains for the same modes shown in figure 3.6, but considering top-hat like profiles for optimal forcing (left panel) and uniform forcing (right panel). The results are similar to those of figure 3.6. The dominant mode is always $m = \pm 1$, followed by the $m = \pm 2$ mode at low and moderate Reynolds numbers, and by $m = 0$ at high Reynolds numbers. The vertical dashed line represents, again, the global instability limit reported by Coenen *et al.* (2017).

It is interesting to note that the critical Reynolds numbers computed with optimal forcing and top-hat-like profiles are similar to those associated with parabolic profiles, namely $Re \approx 8$ for $m = \pm 1$ and $Re \approx 15$ for $m = 0$ and $m = \pm 2$. For uniform forcing, the critical Reynolds numbers are $Re \approx 60$ for $m = \pm 1$, slightly larger than that associated with the parabolic outlet profile, and $Re \approx 200$ for $m = \pm 2$. The main difference between both kinds of outlet profiles is associated with the axisymmetric mode, $m = 0$, which has an associated critical Reynolds number $Re \approx 150$ for a top-hat-like outlet profile. Also, in the latter case, the mode $m = 0$ dominates over $m = \pm 2$.

Summarizing the results of figures 3.4 and 3.5, it can be concluded that, for both types of forcing, top-hat-like profiles have smaller critical Reynolds numbers for modes $m = 0$ and $m = \pm 2$, and slightly larger critical Reynolds numbers for the first helical mode $m = \pm 1$.

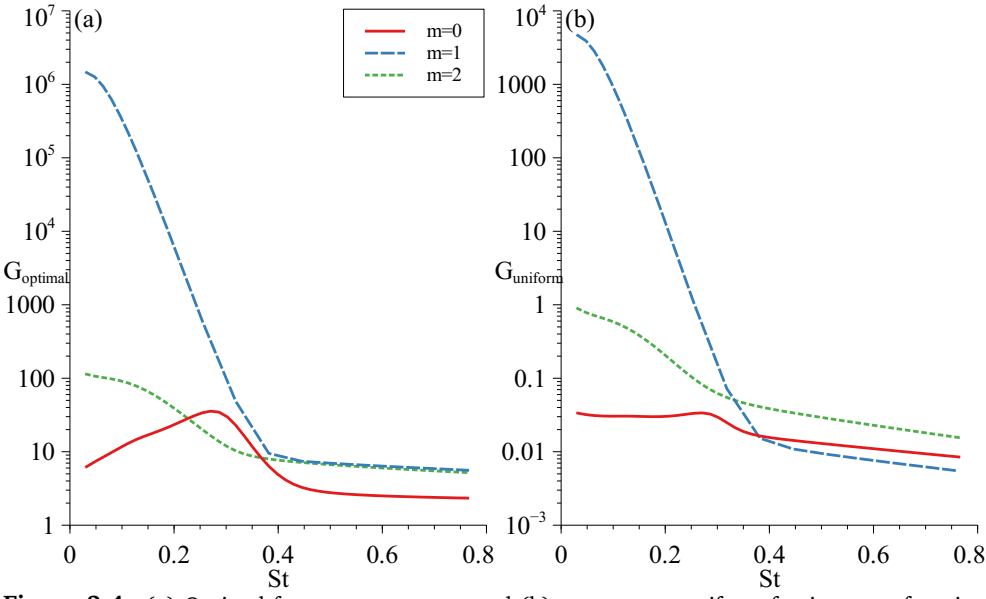

Figure 3.4: (a) Optimal frequency response and (b) response to uniform forcing, as a function of the Strouhal number for $m = 0$ (red solid line), $m = \pm 1$ (blue dashed line) and $m = \pm 2$ (green dotted line). Helium-nitrogen jet with parabolic outlet profile, $D/\theta_0 = 15$, $Re = 200$ and $S = 0.14$.

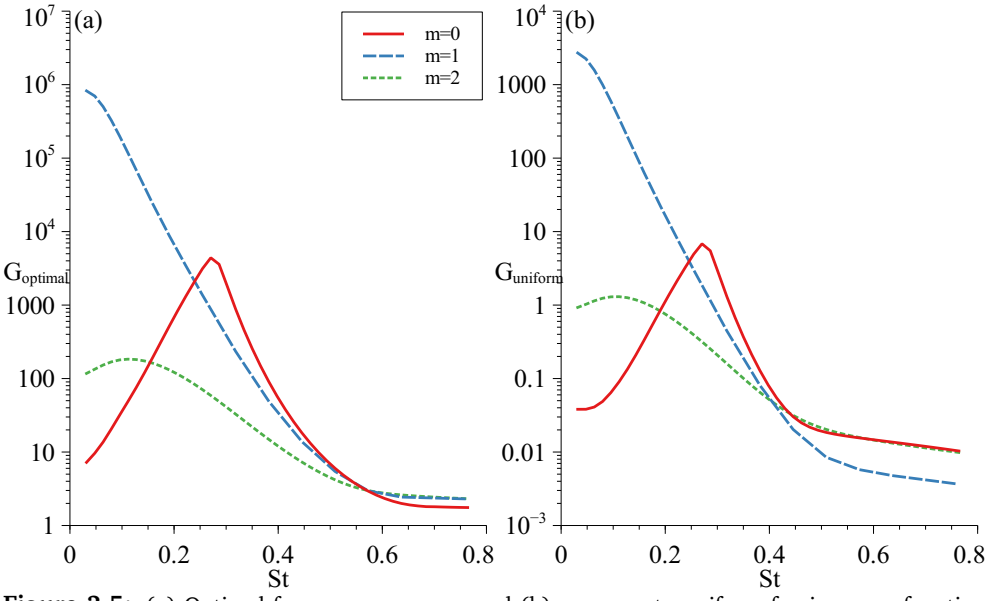

Figure 3.5: (a) Optimal frequency response and (b) response to uniform forcing, as a function of the Strouhal number for $m = 0$ (red solid line), $m = \pm 1$ (blue dashed line) and $m = \pm 2$ (green dotted line). Helium-nitrogen jet with top-hat outlet profile, $D/\Theta_0 = 35$, $Re = 200$ and $S = 0.14$.

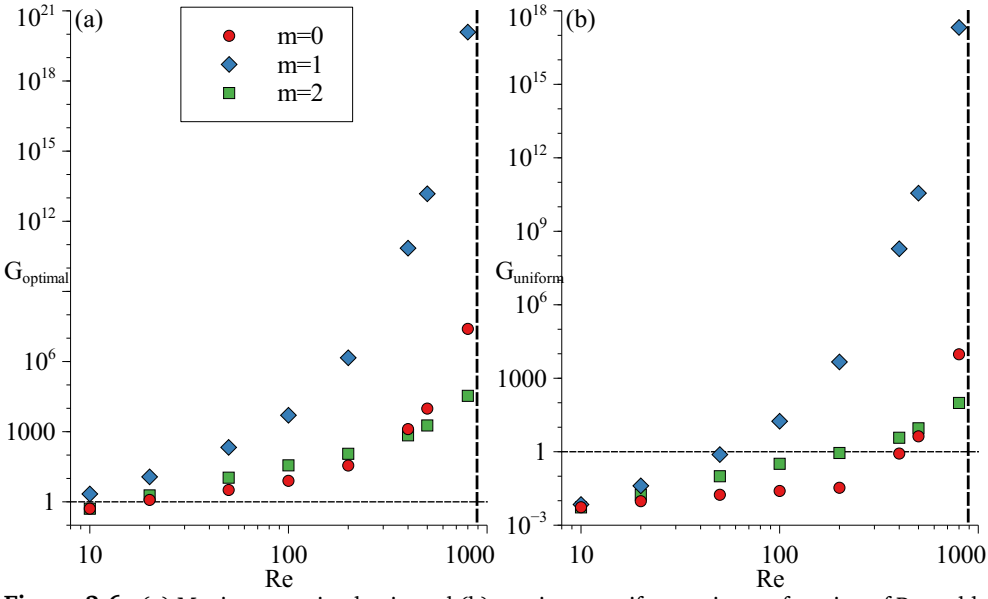

Figure 3.6: (a) Maximum optimal gain and (b) maximum uniform gain as a function of Reynolds number for $m = 0$ (red dots), $m = \pm 1$ (blue diamonds) and $m = \pm 2$ (green squares) for $D/\theta_0 = 15$ and $S = 0.14$.

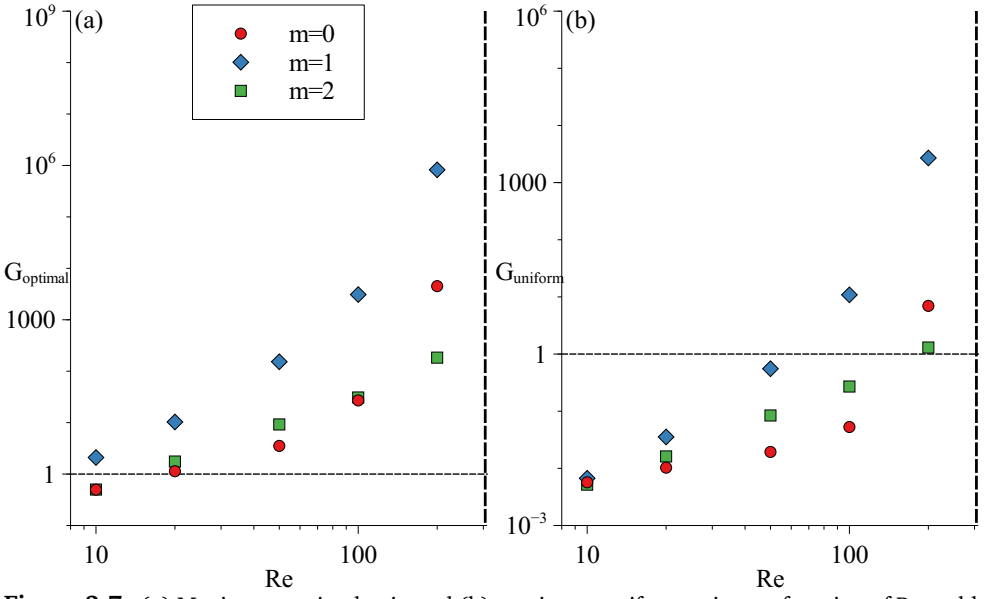

Figure 3.7: (a) Maximum optimal gain and (b) maximum uniform gain as a function of Reynolds number for $m = 0$ (red dots), $m = \pm 1$ (blue diamonds) and $m = \pm 2$ (green squares) for $D/\theta_0 = 35$ and $S = 0.14$.

In view of the direct numerical simulations of axisymmetric helium-nitrogen jets presented in chapter 2, it was deduced that these jets become asymptotically stable below the critical Reynolds number for the onset of globally instability, without any signature of a globally stable but convectively unstable regime. This behavior can be understood in the light of the results of the present chapter, in particular those presented in figures 3.4 and 3.5. Indeed, for Reynolds numbers close to the global instability limit, the maximum gains of the axisymmetric mode $m = 0$ under uniform forcing conditions are too small to compensate for the tiny numerical noise. In other words, the product of numerical noise times the gain seems to be much smaller than the numerical resolution of the simulations, which thereby tend asymptotically to the steady base flow state.

As reviewed in the introduction section of the present chapter, there are few examples in the literature of experiments where the transition from stable to unstable flow in round jets was examined, but only in the case of constant-density jets. For this reason, the next section is devoted to present the results of the global frequency response analysis applied to constant-density jets.

3.6.1.2 Constant-density jets

Figures 3.8 and 3.9 show the optimal gains (left panels) and the gains associated with uniform forcing (right panels) for the different azimuthal modes indicated in the legends. In all these cases, the jet has constant density, $S = 1$, and the Reynolds number is $Re = 200$. The outlet velocity profile is the fully-developed Poiseuille profile with $D/\theta_0 = 15$ in figure 3.8, and a top-hat like profile with $D/\theta_0 = 35$ in figure 3.9.

From the results of figure 3.8 it is deduced that the frequency response of constant-density jets is similar to that of helium-nitrogen jets for parabolic outlet profiles. The first helical mode, $m = \pm 1$, has associated gains that are three orders of magnitude larger for optimal forcing (figure 3.8a) than in the uniform forcing case (figure 3.8b). Moreover, the first helical mode clearly dominates over the other azimuthal modes. In the case of optimal forcing, the amplification curves of modes $m = 0$ and $m = \pm 2$ decrease monotonically with the Strouhal number, while the axisymmetric mode, $m = 0$, has a maximum at $St \approx 0.5$. It can also be appreciated that in the case of optimal forcing all the modes are unstable, with gains larger than one, but in the case of uniform forcing only the first helical mode is unstable at low to moderate values of the Strouhal number. Moreover, for uniform forcing, the axisymmetric mode decreases monotonically with St, in contrast with its behavior in the optimal case.

As happened in the case of low-density jets presented in the previous section, figure 3.9 reveals that the gains of mode $m = \pm 1$ for a top-hat velocity profile with $D/\theta_0 = 35$ are slightly smaller than in the case of parabolic profiles displayed in figure 3.8. In contrast, the axisymmetric mode $m = 0$ has only a slightly larger gain for the top-hat profile around the maximum, that takes place at $St \approx 0.5$ both for optimal and uniform forcing.

In figure 3.10 the maximum gain for each mode is shown for parabolic outlet profiles.

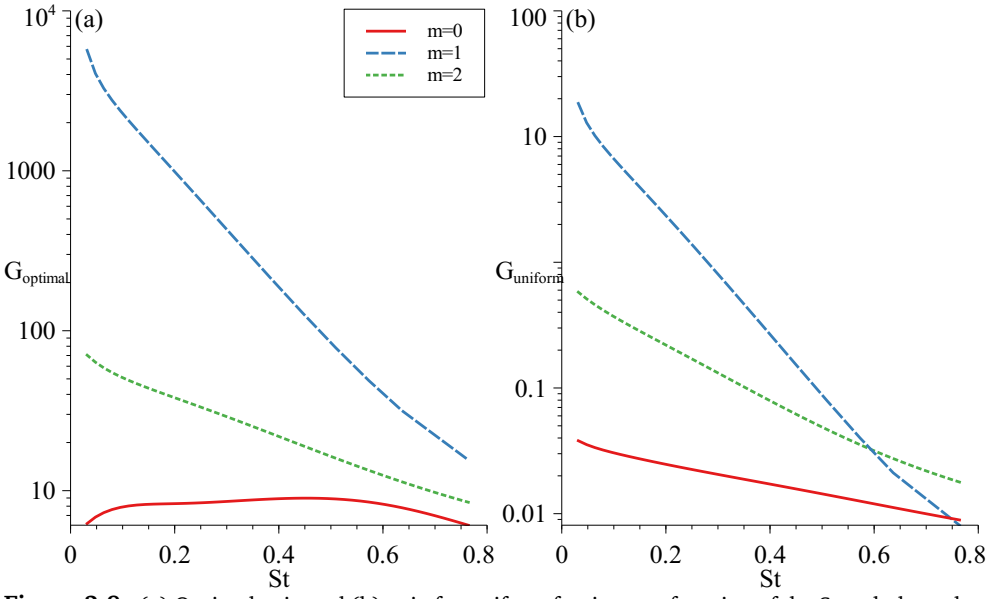

Figure 3.8: (a) Optimal gain and (b) gain for uniform forcing as a function of the Strouhal number for $m = 0$ (red solid line), $m = \pm 1$ (blue dashed line) and $m = \pm 2$ (green dotted line) for $D/\theta_0 = 15$, $Re = 200$ and $S = 1$.

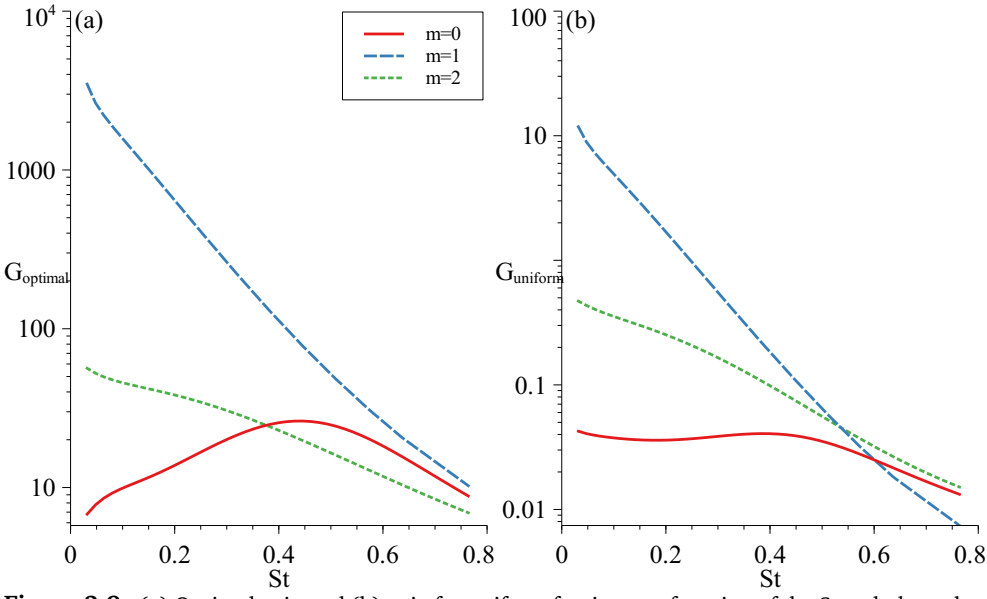

Figure 3.9: (a) Optimal gain and (b) gain for uniform forcing as a function of the Strouhal number for $m = 0$ (red solid line), $m = \pm 1$ (blue dashed line) and $m = \pm 2$ (green dotted line) for $D/\theta_0 = 35$, $Re = 200$ and $S = 1$.

The first helical mode $m = \pm 1$ (blue diamonds), has larger gains than modes $m = 0$ (red dots) and $m = \pm 2$ (green squares) as well as those associated with low-density jets shown in figure 3.6.

The critical Reynolds number for the dominant mode, $m = \pm 1$, is $Re \approx 8$ for optimal forcing and $Re \approx 90$ for uniform forcing, both being larger than the corresponding values found in the previous section for low-density jets. The subdominant modes $m = 0$ and $m = \pm 2$ have a critical Reynolds number $Re \approx 15$ for optimal forcing. For uniform forcing, the mode $m = \pm 2$ has a critical Reynolds number $Re \approx 450$, but the gain of the axisymmetric mode, $m = 0$, is less than one up to the largest value of the Reynolds number reached in our computations, namely $Re = 4,000$.

Figure 3.11 represents the maximum gains for optimal forcing (left panel) and uniform forcing (right panel) for the top-hat like outlet velocity profile, showing similar results as in all previous cases: the dominant mode is always $m = \pm 1$, while the mode $m = \pm 2$ is the subdominant one up to $Re \approx 500$. For larger values of the Reynolds number the axisymmetric mode $m = 0$ has larger maximum gains than the mode $m = \pm 2$.

The critical Reynolds numbers under optimal forcing conditions are similar for top-hat and parabolic outlet profiles, namely $Re \approx 8$ for $m = \pm 1$ and $Re \approx 15$ for $m = 0$ and $m = \pm 2$. In the case of uniform forcing, the critical Reynolds numbers for top-hat outlet profiles are $Re \approx 90$ for $m = \pm 1$, $Re \approx 350$ for $m = \pm 2$ and $Re \approx 450$ for $m = 0$.

Table 3.1 summarizes the different values of the critical Reynolds number obtained in the present work for the most unstable mode, $m = \pm 1$. These results contemplate both optimal and uniform forcing structures, as well as three different values of the density ratio, namely $S = 0.143$, $S = 0.5$ and $S = 1$. Considering first the case of optimal forcing, the critical Reynolds number is below 10 for all density ratios, with an associated Strouhal number, $St = 0.03$, corresponding with the smallest value converged in the computations due to the limitations of domain length discussed above (see figures 3.4, 3.5, 3.8 and 3.9). Indeed, at these small frequencies the typical wavelength of the response structures is very long, and the domain length is limited by our computational resources.

In the case of uniform forcing, the critical Reynolds number for low-density jets with $S = 0.143$ is $Re = 54$ for a parabolic outlet profile and $Re = 59$ for a top-hat outlet profile. For an intermediate value of the density ratio, $S = 0.5$, the critical Reynolds numbers are $Re = 73$ and $Re = 82$ for parabolic and top-hat outlet profiles, respectively. Finally, for constant-density jets, $S = 1$, the corresponding critical Reynolds numbers are $Re = 85$ and $Re = 97$, respectively. It is thus deduced that the influence of the outlet velocity profile is slightly stronger when the density ratio increases, with smooth profiles presenting smaller critical Reynolds numbers than top-hat like profiles.

Let us now compare our results with the evidence available from previous experimental and numerical studies. The experiments of Reynolds (1962) indicated the existence of a critical Reynolds number within the range $150 < Re_{D,c} < 300$ for constant-density jets with parabolic outlet profiles, and observed that the transition was

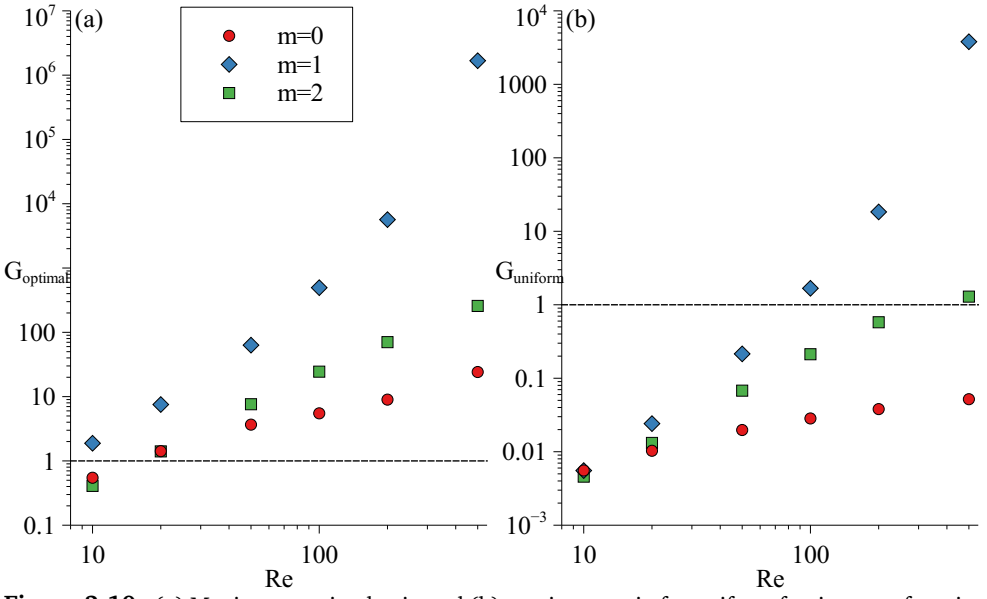

Figure 3.10: (a) Maximum optimal gain and (b) maximum gain for uniform forcing, as a function of the Reynolds number for $m = 0$ (red dots), $m = \pm 1$ (blue diamonds) and $m = \pm 2$ (green squares). Here, $D/\theta_0 = 15$ and $S = 1$.

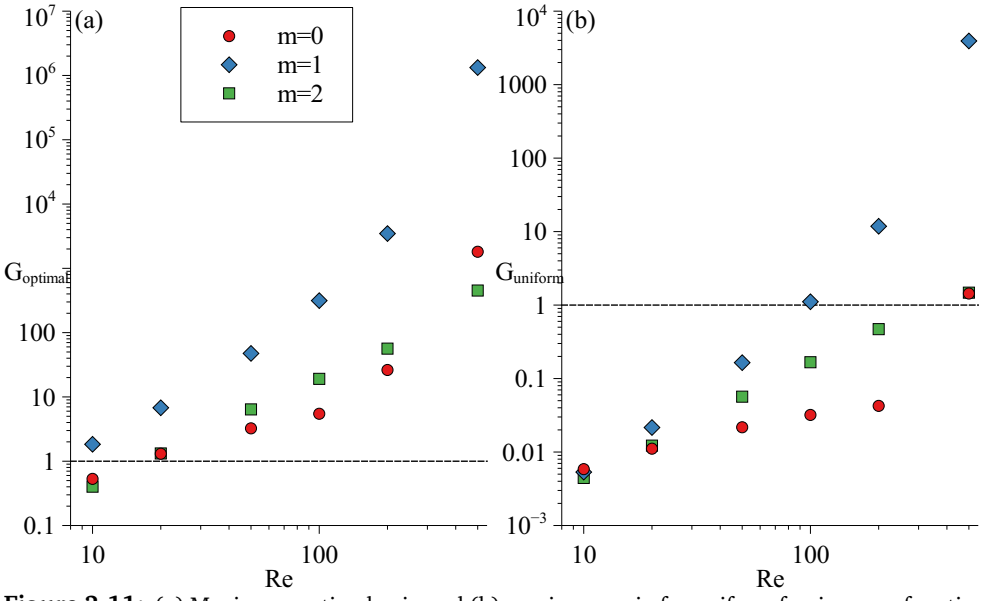

Figure 3.11: (a) Maximum optimal gain and (b) maximum gain for uniform forcing, as a function of the Reynolds number for $m = 0$ (red dots), $m = \pm 1$ (blue diamonds) and $m = \pm 2$ (green squares). Here, $D/\theta_0 = 35$ and $S = 1$.

	$S = 0.143$		$S = 0.5$		$S = 1$	
	Opt.	Unif.	Opt.	Unif.	Opt.	Unif.
$D/\theta_0 = 15$	$Re < 10$	$Re = 54$	$Re < 10$	$Re = 73$	$Re < 10$	$Re = 85$
$D/\theta_0 = 35$	$Re < 10$	$Re = 59$	$Re < 10$	$Re = 82$	$Re < 10$	$Re = 97$

Table 3.1: Critical Reynolds numbers for the most unstable mode $m = \pm 1$.

associated with sinuous undulations of the jet column. Similarly, the numerical simulation reported by Danaila *et al.* (1997) at $Re_D = 300$ and top-hat-like outlet profiles, revealed an unstable jet with dominant $m = \pm 1$ helical structures with a Strouhal number $St \approx 0.3$. Although the picture that emerges from these studies is qualitatively consistent with the results of the present work, the dominant Strouhal number deduced from our frequency response analysis, namely $St \approx 0.03$, is much smaller than the numerical one found by Danaila *et al.* (1997). In marked contrast with the results of Reynolds (1962) and Danaila *et al.* (1997), the experiments reported by Viilu (1962) for a constant-density jet with Poiseuille outlet velocity profile pointed to the existence of a critical Reynolds number $Re_D \approx 11$, defined by the transition from a stable to a marginally stable flow where perturbations disappear after a long time. However, it must be pointed out that Viilu (1962) did not report any clear information about the spatial structures associated with this transition, except for the presence of "ripples".

From the discussion of the previous paragraph it is clear that new experimental and numerical studies should be performed to improve our understanding of the natural transition process of submerged laminar jets, and to provide a more precise quantitative characterization of the critical Reynolds number and its dependence on the flow parameters.

3.6.2 Frequency response analysis II: Spatial structures

This subsection is devoted to present and discuss the spatial structure of the optimal disturbances and the corresponding responses. Since the uniform forcing presents similar spatial structures as the optimal ones, only the latter will be shown for conciseness.

All the figures shown in this section share a common design: the optimal forcing and the corresponding response are shown in panels (a) and (b), respectively, both by means of isocontours of the axial velocity amplitude. Finally, the axial velocity amplitude is represented along the line $r = 0.5$ in panel (c). Notice that only a small part of the spatial domain is shown to help the reader visualize panels (a) and (b), and that the colorbar scales in these two panels are different. To compare the responses of the three leading azimuthal modes, fixed values of the Strouhal number, $St = 0.3$, of the Reynolds number, $Re = 200$, and of the density ratio, $S = 0.14$, were chosen in all cases.

The following three figures consider jets with Poiseuille outlet velocity profiles, $D/\theta_0 = 15$. In particular, figure 3.12 displays the forcing and response structures for

the axisymmetric mode, $m = 0$. It is deduced that the response is contained within a distance of about 30 injector radii, presenting a maximum at an axial position of approximately 10. Figure 3.13, which corresponds to the first helical mode $m = \pm 1$,

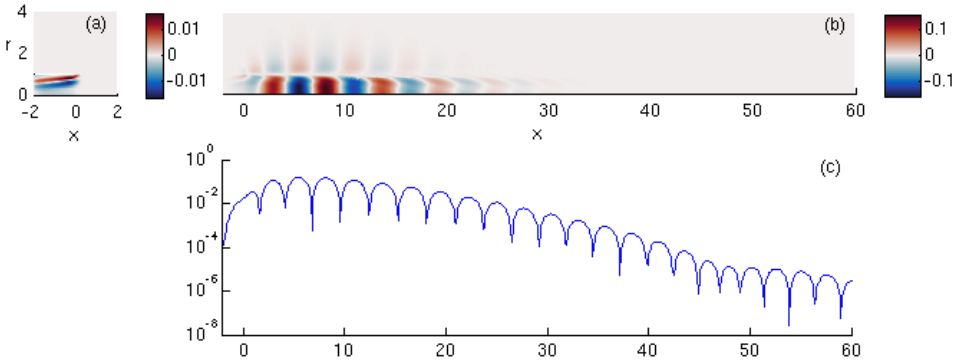

Figure 3.12: (a) Contours of optimal forcing, (b) contours of optimal response and (c) optimal response profile at $r = 0.5$, for the axisymmetric mode, $m = 0$, and a jet with $S = 0.14$, $D/\theta_0 = 15$, $Re = 200$ and $St = 0.3$. The three panels show the amplitude of the axial velocity.

shows an optimal response contained within about 50 radii downstream of the injector outlet, with a maximum at an axial distance of approximately 20. Thus, the typical axial scales are almost doubled with respect to the axisymmetric mode for the same values of the Reynolds and Strouhal numbers. Finally, figure 3.14 illustrates the case of mode

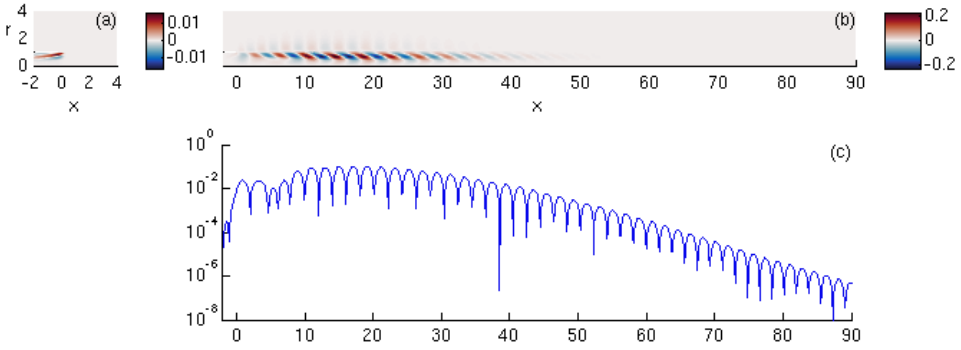

Figure 3.13: (a) Contours of optimal forcing, (b) contours of optimal response and (c) optimal response profile at $r = 0.5$, for the mode $m = \pm 1$, and a jet with $S = 0.14$, $D/\theta_0 = 15$, $Re = 200$ and $St = 0.3$. The three panels show the amplitude of the axial velocity.

$m = \pm 2$, whose optimal response is contained within a distance of about 20 radii, with a maximum at approximately 5, and therefore considerably closer to the injector than the $m = 0$ and $m = \pm 1$ modes.

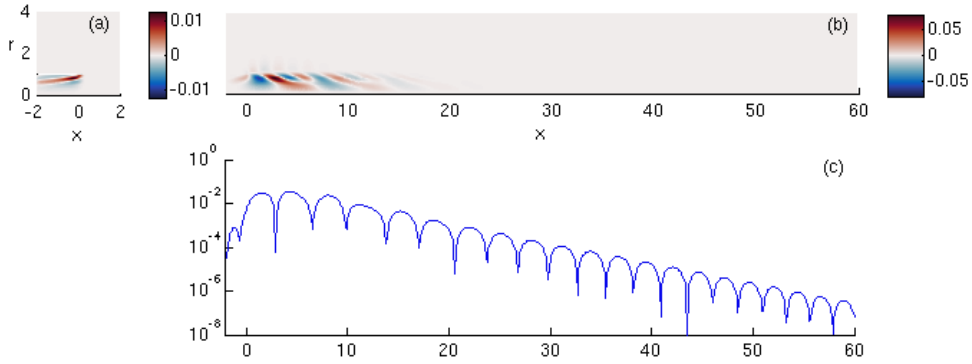

Figure 3.14: (a) Contours of optimal forcing, (b) contours of optimal response and (c) optimal response profile at $r = 0.5$, for the mode $m = \pm 2$, and a jet with $S = 0.14$, $D/\theta_0 = 15$, $Re = 200$ and $St = 0.3$. The three panels show the amplitude of the axial velocity.

In the next three figures, the outlet velocity profile of the jet is top-hat-like with $D/\theta_0 = 35$. Figure 3.15 corresponds to the axisymmetric mode $m = 0$, and reveals that the response is contained within a distance of 30 radii, with a maximum at approximately 10. Moreover, figure 3.16 shows the case of the first helical mode, $m = \pm 1$, whose response

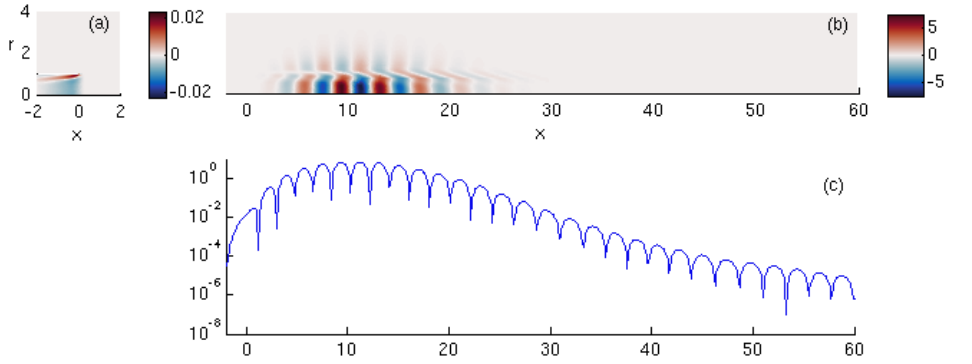

Figure 3.15: Optimal forcing and response for $m = 0$, $S = 0.14$, $D/\theta_0 = 35$, $Re = 200$ at $St = 0.3$

is contained within about 40 radii, and presents its maximum at approximately 15. It is thus deduced that the response is closer to the injector than in the case of a parabolic outlet profile. Finally, figure 3.17 presents the case of mode $m = \pm 2$, whose response is contained within a distance of about 20 radii, with a maximum at approximately 5. Again, the response takes place closer to the injector than for the modes $m = 0$ and $m = \pm 1$, but in this case is similar to that found for a parabolic outlet profile.

The spatial structure of the forcing and response for jets with density ratios $S = 0.5$

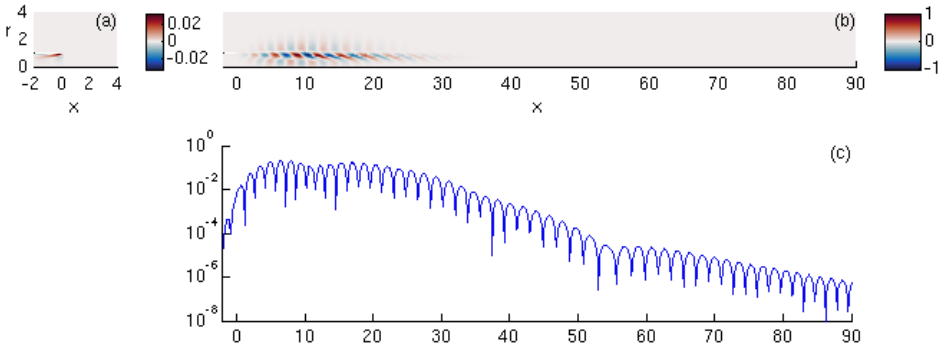

Figure 3.16: Optimal forcing and response for $m = \pm 1$, $S = 0.14$, $D/\theta_0 = 35$, $Re = 200$ at $St = 0.3$

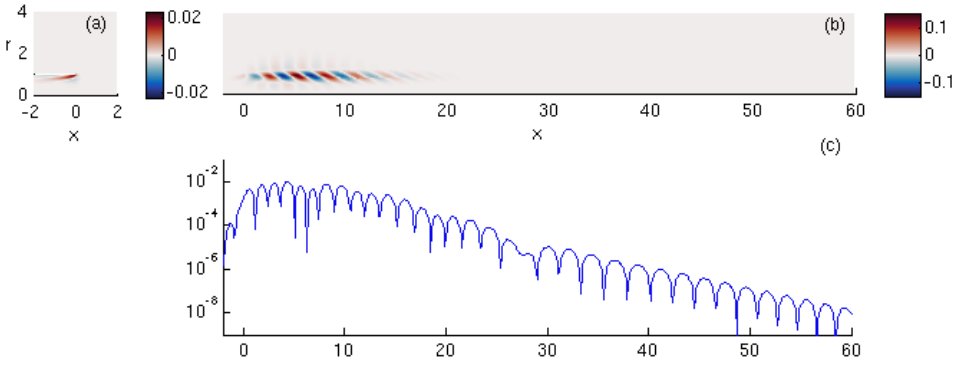

Figure 3.17: Optimal forcing and response for $m = \pm 2$, $S = 0.14$, $D/\theta_0 = 35$, $Re = 200$ at $St = 0.3$

and $S = 1$ can be found in appendix C.

3.6.3 Influence of the injector geometry

This subsection is devoted to discuss the influence of two geometrical modifications on the frequency response of submerged jets. First, we will examine the influence of the length of the injection pipe. Second, we will consider an alternative to the injector pipe configuration, in which the jet emerges from a wall orifice of circular cross-section.

The upper panel of figure 3.18 shows a sketch of the computational domain used to represent a jet that emerges from a wall orifice. Note that the only change with respect to the injector configuration considered up to this point is the presence of a radial wall attached to the nozzle exit. The geometrical parameters are again R and L_{pipe}, and the dimensional variables associated with the jet, ρ_j, μ_j,$\bar{u}_i$, and the ambient, ρ_∞, μ_∞, are also the same. The desired outlet velocity profiles are achieved using the same methodology as in previous cases, as described in appendix A.

The lower panel of figure 3.18 indicates the typical triangle size, h, associated with the four refinement regions plotted with different shades of gray, which were chosen to achieve convergence of the results with respect to the mesh size and its discretization. The refinement surfaces were placed in the regions of largest shear and close to the jet outlet. The seed triangles were chosen in decreasing sizes, from $h_1 = 0.4$ to $h_2 = 0.1$, $h_3 = 0.06$ and the finest close to the corner region, $h_4 = 0.02$. The resulting mesh is similar to the ones used by Garnaud *et al.* (2013) and by Qadri & Schmid (2017). The domain size is determined by the values of x_{max} and r_{max}, which were set to 150 and 10, respectively, to ensure independence of the results.

Figure 3.19 shows that the different azimuthal modes $m = 0$ (red), $m = \pm 1$ (blue) and $m = \pm 2$ (green) converge with respect to the pipe length, provided that $x_p > 16$ in the case of optimal forcing. For uniform forcing, the results are similar for the first and second helical modes, $m = \pm 1$ and $m = \pm 2$, but not so conclusive for the axisymmetric mode $m = 0$. Since the tubes are long, only parabolic outlet velocity profiles, with $D/\theta_0 = 15$, were considered in this particular case.

Table 3.2 shows the maximum optimal gains of the axisymmetric mode $m = 0$ for jets with pipe length $x_p = 16$ at a Reynolds number $Re = 200$ and three different values of S, comparing the results of injector and wall geometries. As can be seen, the maximum relative difference corresponds to helium-air jets, and are smaller as the density ratio increases.

	$S = 0.143$	$S = 0.5$	$S = 1$
Injector $G_{opt,max}$	48.7343	18.9314	16.0101
Wall $G_{opt,max}$	35.5695	19.3183	16.2571

Table 3.2: Maximum optimal gain with injector and wall geometries for $m = 0$ and $Re = 200$.

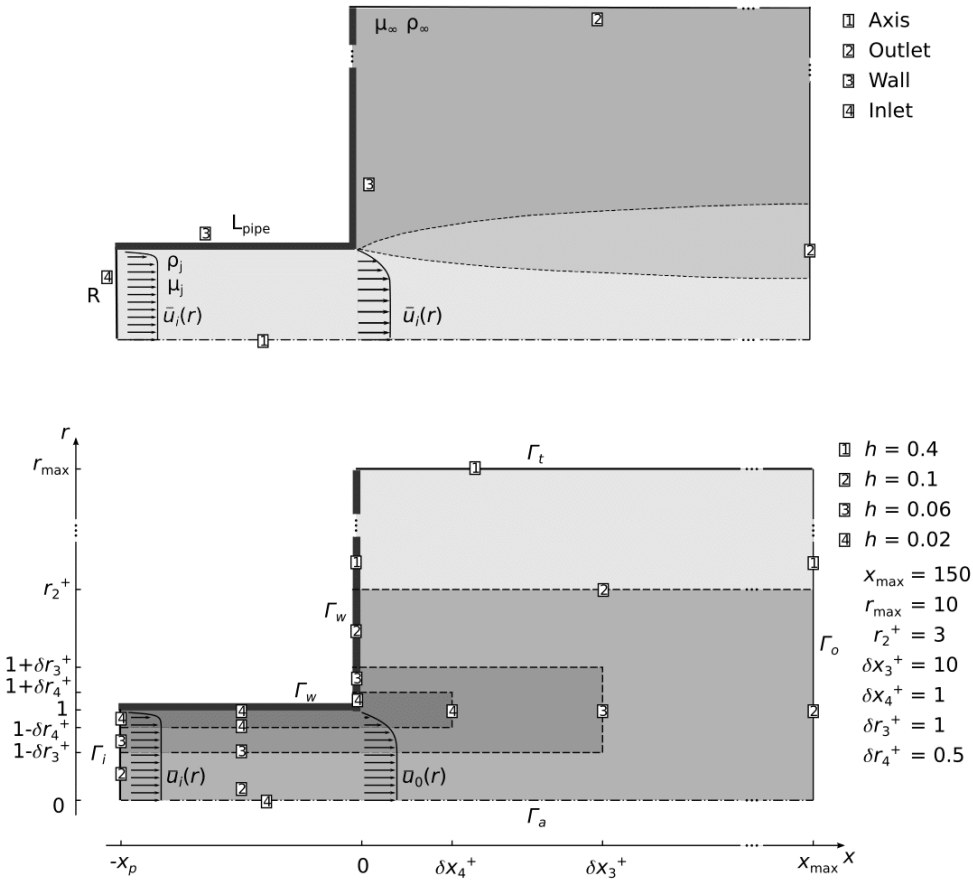

Figure 3.18: The upper panel sketches the flow configuration with the physical properties and boundaries. The lower panel shows the mesh seeds on each boundary and the sub-domains used to control the spatial resolution.

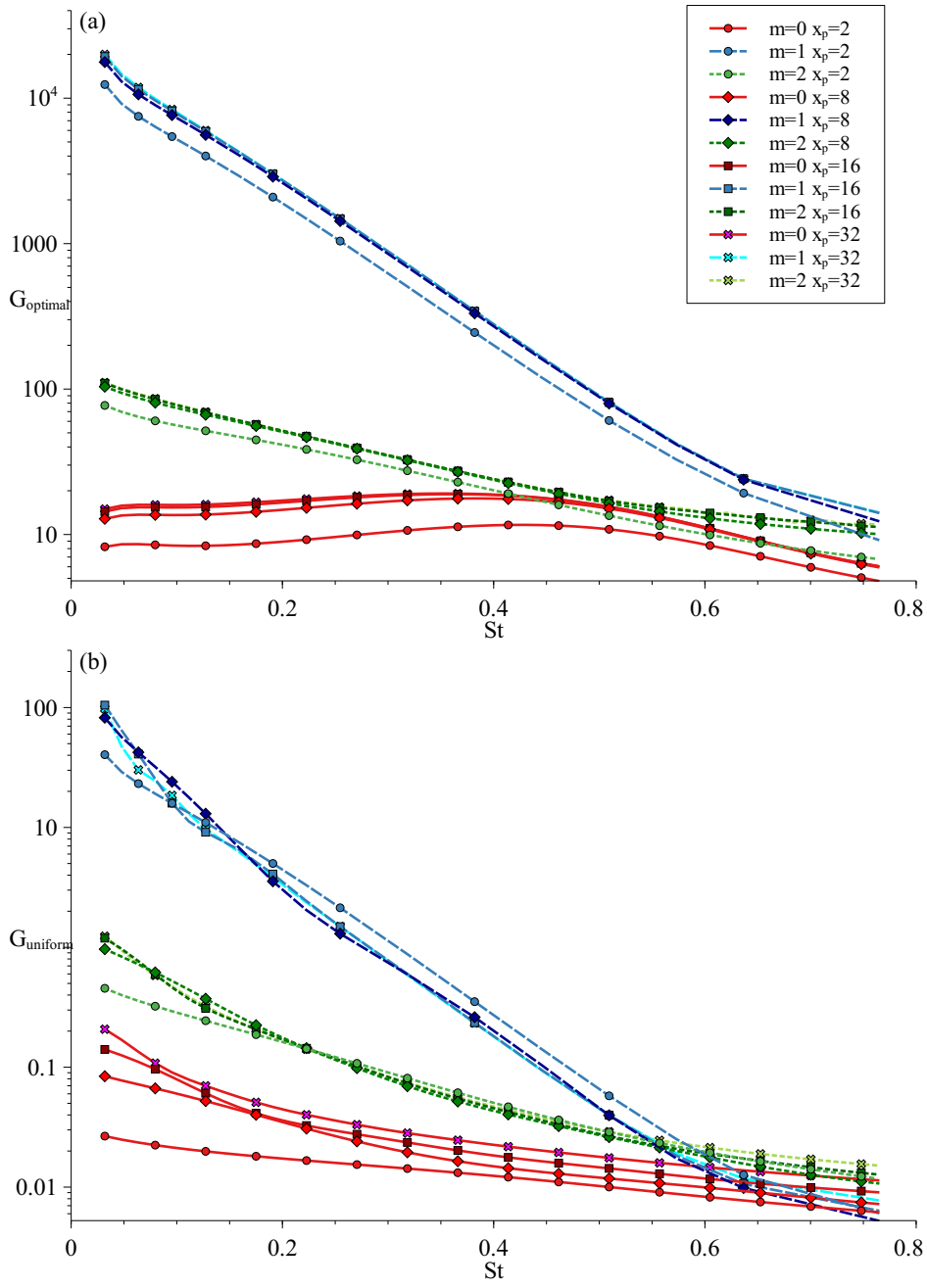

Figure 3.19: Gains for different pipe lengths, x_p, corresponding to (a) optimal forcing and (b) uniform forcing for a jet with $S = 0.5$, $Re = 200$ and parabolic outlet velocity profiles. Red colors represent the axisymmetric mode, $m = 0$, blue colors the first helical mode, $m = \pm 1$, and green colors the second helical mode, $m = \pm 2$.

In contrast, table 3.3 reveals that, for uniform forcing, the gains are one order-of-magnitude larger in the injector geometry than in the wall geometry. In the latter case, the maximum gain decreases as S increases, in agreement with the trend found for optimal forcing, but the injector with uniform forcing configuration does not show any trend.

	$S = 0.143$	$S = 0.5$	$S = 1$
Injector $G_{uni,max}$	0.1799	0.1408	0.1931
Wall $G_{uni,max}$	0.0210	0.0128	0.0101

Table 3.3: Maximum uniform gain with injector and wall geometries for $m = 0$ and $Re = 200$.

In figure 3.20 the comparison between the gains of the axisymmetric mode for both geometries is extended to contemplate the density ratios $S = 0.14$ (red), $S = 0.5$ (blue) and $S = 1$ (green). In all cases, the Reynolds number is $Re = 200$, the outlet velocity profile is parabolic, and the pipe length is $x_p = 16$. The results of the injector configuration are represented with solid lines, while those of the wall orifice geometry are plotted with dashed lines. From the results of figure 3.20 it is deduced that, in the case of uniform forcing, the injector configuration leads to larger gains in the whole range of Strouhal numbers for all values of S. In contrast, under optimal forcing the gains are similar for both geometric configurations, with the exception of the larger gains observed for $S = 0.14$ within a range of Strouhal numbers around the maximum gain.

3.6.4 The effect of an extended forcing region in the wall orifice configuration

The present subsection is dedicated to a brief discussion of the influence of the forcing region on the frequency response of jets in the wall orifice geometry. The first forcing region is the one considered up to this point. It is restricted inside the pipe, with length 16 and radius 1. The second forcing region also includes the pipe, but is extended inside the jet with a length of 16 downstream of the outlet, and a width of 2 radii.

Figure 3.21 shows the dependence of the maximum gain of the axisymmetric mode, $m = 0$, on the Reynolds number, for a jet with $S = 0.14$ and parabolic outlet velocity profile. The forcing is optimal in figure 3.21(a), and uniform in figure 3.21(b). The red circles display the results for a forcing region restricted inside the pipe, and the blue diamonds represent the results for the extended forcing region. The vertical dashed lines represent the transition from a globally stable to globally unstable jet using the global mode decomposition of Coenen *et al.* (2017). The results demonstrate that extending the forcing region leads to larger gains both for optimal and uniform forcing. Indeed, for $Re = 100$ the maximum optimal gain for the forcing region restricted inside the pipe is $G_{opt,in} \approx 10$ while $G_{opt,ex} \approx 50$ for the extended region. Similarly, in the case of uniform forcing, $G_{uni,in} \approx 0.01$ while $G_{uni,ex} \approx 0.1$, i.e. one order of magnitude larger. This

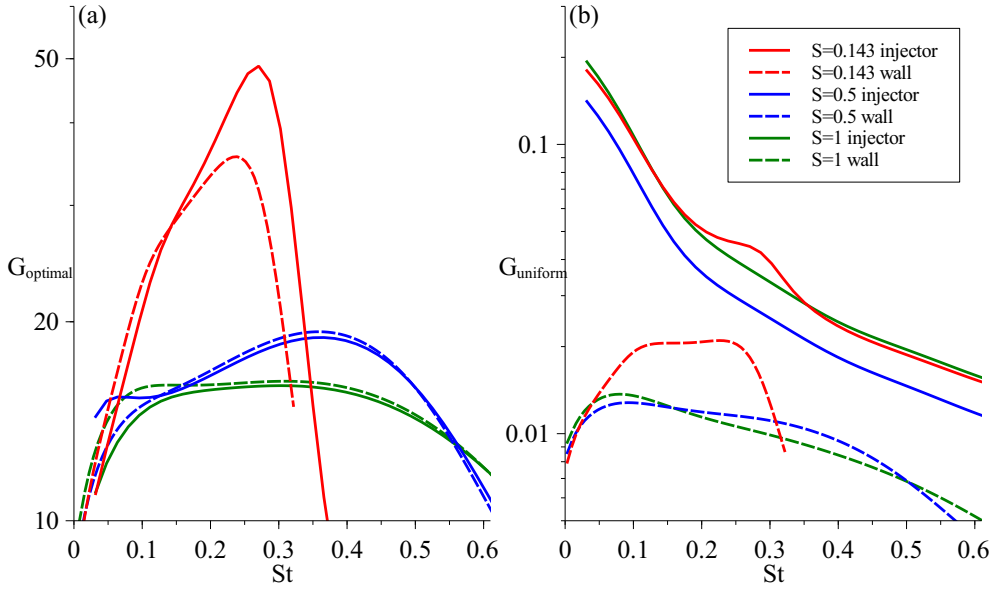

Figure 3.20: Gain curves for the wall orifice geometry (dashed lines), and for the injector geometry (solid lines), for (a) optimal forcing and (b) uniform forcing, for density ratios $S = 0.14$ (red), $S = 0.5$ (blue) and $S = 1$ (green) for $m = 0$, $D/\theta_0 = 15$ and $Re = 200$.

difference is consistently observed for the whole range of Reynolds numbers. As expected, optimal gains are several orders of magnitude larger than uniform ones.

Figure 3.22 shows isocontours of the logarithm of the maximum gain for optimal forcing (left) and uniform forcing (right) restricted inside the pipe. The black-filled area delimits the globally unstable region. It can be seen that the difference between uniform and optimal gains increase as S increases. However, when S increases beyond a certain limit, the dominant eigenmode is contaminated with spurious eigenmode branches affected by the length of the computational domain, as described by Coenen *et al.* (2017). Black dashed lines provide an estimation of the transition curve, although it is important to emphasize that it depends on the domain size. Finally, figure 3.23 represents the same information as figure 3.22, but in the case of the extended forcing region. As expected, the maximum gains are larger for the same value of the Reynolds number.

3.7 Conclusions and further work

As a first general conclusion, it has been found that the first helical mode, $m = \pm 1$, is the most unstable mode for all the configurations studied in the present chapter. A salient

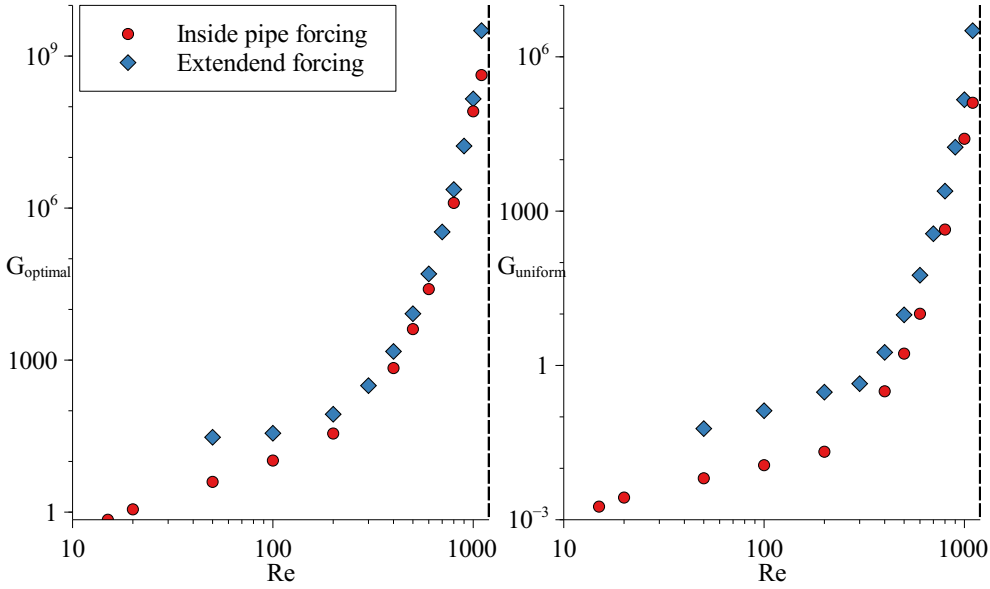

Figure 3.21: Maximum gain of the axisymmetric mode, $m = 0$, as a function of the Reynolds number for (a) optimal forcing and (b) uniform forcing. The density ratio is $S = 0.14$. Red dots indicate forcing restricted inside the pipe, and blue diamonds correspond to the extended forcing region described in the main text.

feature of this mode is the fact that its largest gains take place at very small values of the Strouhal number, associated with long characteristic length scales in its response to forcing. This behavior sets a lower limit for the Strouhal number that can be converged with given computational resources that, in our case, corresponded to $St = 0.03$. The axisymmetric mode, $m = 0$, and the second helical one, $m = \pm 2$, are always subdominant, and may both be the next-to-leading mode depending on the Strouhal number.

Low-density jets have a similar response behavior under optimal and uniform forcing conditions, but optimal forcing provides about two orders of magnitude larger gains than uniform forcing. The mode $m = \pm 1$ is the most unstable one, followed by either $m = 0$ at moderate to high Strouhal numbers, or $m = \pm 2$ at low Strouhal numbers. Top-hat like outlet velocity profiles with $D/\theta_0 = 35$ have larger gains for $m = 0$ than parabolic ones.

The critical Reynolds number of low-density jets under optimal forcing is $Re \approx 8$ for $m = \pm 1$ and $Re \approx 15$ for $m = 0$ and $m = \pm 2$ for both types of outlet velocity profiles. In contrast, under uniform forcing conditions the critical Reynolds numbers with parabolic outlet profile is $Re = 54$ for $m = \pm 1$, $Re \approx 200$ for $m = \pm 2$, and $Re \approx 450$ for $m = 0$. For top-hat like velocity profiles, it has been found that $Re = 59$ for $m = \pm 1$, $Re \approx 150$ for $m = 0$, and $Re \approx 200$ for $m = \pm 2$.

In the case of constant-density jets, the gains for optimal forcing are larger than those

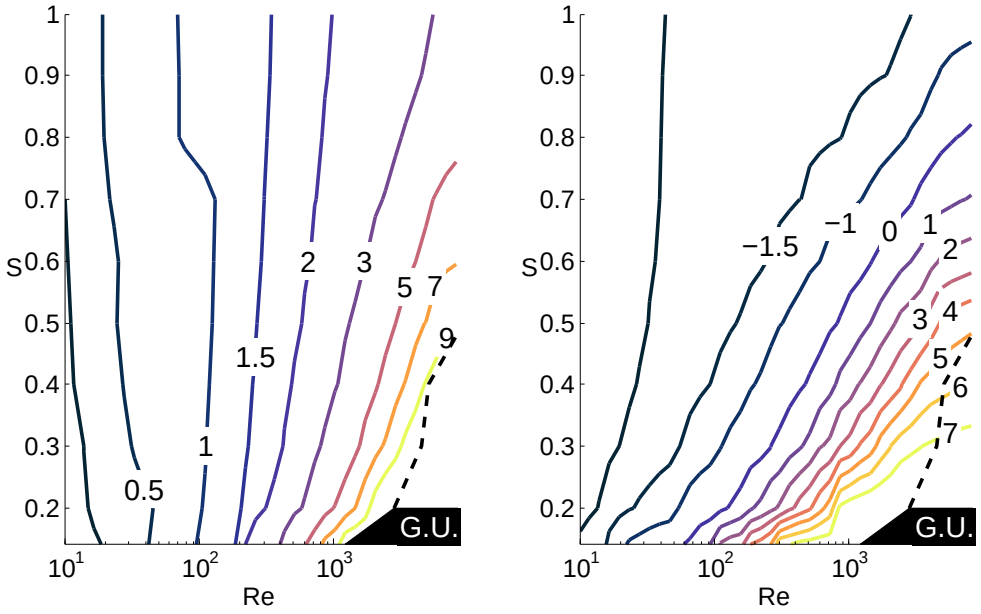

Figure 3.22: Logarithm of the gain for optimal (left) and uniform (right) forcing restricted inside the pipe for $m = 0$.

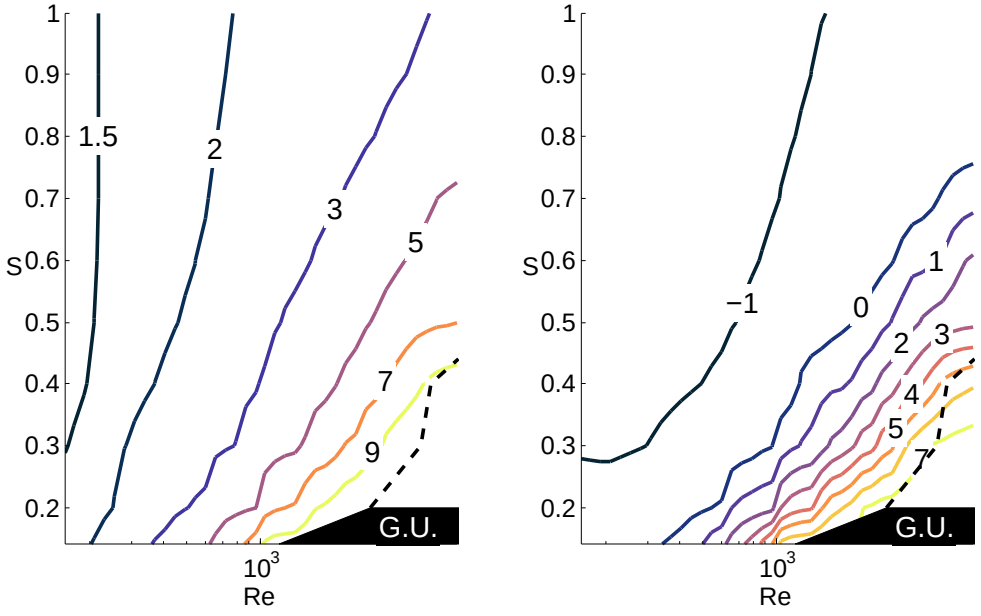

Figure 3.23: Logarithm of the gain for optimal (left) and uniform (right) forcing in the extended region for $m = 0$.

for uniform forcing by several orders of magnitude, and the most unstable mode is also $m = \pm 1$. The modes $m = \pm 1$ and $m = \pm 2$ have monotonically decreasing gains as a function of the Strouhal number. However, the axisymmetric mode, $m = 0$, presents a maximum at $St \approx 0.5$. As in the case of low-density jets, modes $m = 0$ and $m = \pm 2$ have slightly larger gains for a top-hat like outlet velocity profile than with the parabolic one.

The critical Reynolds number using optimal gain has similar values as light jet $Re \approx 8$ for $m = \pm 1$ and $Re \approx 15$ for $m = 0$ and $m = \pm 2$. On the other hand, using uniform forcing with parabolic profiles, the helical mode $m = \pm 1$ has the critical Reynolds number $Re = 85$ while the mode $m = \pm 2$ have this critical value $Re \approx 450$ and axisymmetric mode $m = 0$ was not found any. Top-hat kind velocity profiles found for mode $m = \pm 1$ a slightly high critical Reynolds number $Re = 97$ but modes $m = 0$ and $m = \pm 2$ have their critical Reynolds number at $Re \approx 450$ both. These results of critical Reynolds number for uniform forcing are found consistent with ones reported by Reynolds (1962) and Danaila *et al.* (1997) for their Reynolds number, although ones from Viilu (1962) must be aware he does not show the response and we can not conclude which mode is closer.

For a fixed value of $St = 0.3$, the spatial structure of the response for parabolic outlet profiles presents local maximum at distances of 5, 10 and 20 and is mainly contained within 20, 30 and 50 radii for $m = \pm 2$, $m = 0$ and $m = \pm 1$, respectively. For top-hat like outlet profiles, the results are similar, except that the mode $m = \pm 1$ has its maximum response closer to the injector.

Another conclusion extracted from the present study concerns the role of the jet injection geometry. By comparing two different configurations, namely an injector tube far from walls and a circular orifice on a wall, it has been shown that low-density jets under optimal forcing conditions present substantial difference in gain, while for constant-density jets the results are similar. In the case of uniform forcing, the gains for the injector configuration are one order of magnitude larger than those associated with the orifice geometry for all the density ratios studied.

With respect to the extent of the forcing region, it has been found that the results are independent of the injector pipe length, x_p, provided that $x_p \gtrsim 16$. In addition, by extending the forcing region outside the pipe, our results have revealed an increase in the gains for optimal and uniform forcing.

Future work suggested by the present chapter could follow several lines of research. First, a more detailed study of the influence of the density ratio and of the momentum thickness parameter D/θ_0 on the critical Reynolds number would be desirable. Another important aspect, not considered in the present work, is the use of a more realistic model of the actual disturbances present in practical applications. To this end, introducing the disturbances as inflow boundary conditions could change the results, and help clarifying the relationship between the frequency response analysis and the critical Reynolds number found in experiments.

References

Amestoy, P.R., Duff, I.S. & L'Excellent, J.-Y. 2000 Multifrontal parallel distributed symmetric and unsymmetric solvers. *Computer Methods in Applied Mechanics and Engineering* **184** (2), 501 – 520.

Batchelor, G. K. & Gill, A. E. 1962 Analysis of the stability of axisymmetric jets. *J. Fluid Mech.* **14**, 529–551.

Coenen, W., Lesshafft, L., Garnaud, X. & Sevilla, A. 2017 Global instability of low-density jets. *J. Fluid Mech.* **820**, 187:207.

Coenen, W. & Sevilla, A. 2012 The structure of the absolutely unstable regions in the near eld of low-density jets. *J. Fluid Mech.* **713**, 123–149.

Coenen, W., Sevilla, A. & Sánchez, A. 2008 Absolute instability of light jets emerging from circular injector tubes. *Phys. Fluids* **20**, 074104.

Crow, S. C. & Champagne, F. H. 1971 Orderly structure in jet turbulence. *Journal of Fluid Mechanics* **48** (3), 547–591.

Danaila, Ionut, Dušek, Jan & Anselmet, Fabien 1997 Coherent structures in a round, spatially evolving, unforced, homogeneous jet at low Reynolds numbers. *Physics of Fluids* **9** (11), 3323–3342.

Garnaud, X., Lesshafft, L., Schmid, P.J. & Huerre, P. 2013 Modal and transient dynamics of jet flows. *Phys. Fluids* **25** (4), 044103.

Hallberg, M. P. & Strykowski, P. J. 2006 On the universality of global modes in low-density axisymmetric jets. *J. Fluid Mech.* **569**, 493–507.

Hecht, Frédéric 2012 New development in freefem++. *Journal of numerical mathematics* **20** (3-4), 251–266.

Hirschfelder, Joseph Oakland, Bird, Robert Byron & Curtiss, Charles Francis 1954 *Molecular theory of gases and liquids*. John Wiley.

Kambe, Tutomu 1969 The stability of an axisymmetric jet with parabolic profile. *Journal of the Physical Society of Japan* **26** (2), 566–575.

Lanczos, Cornelius 1996 *Linear differential operators*. SIAM.

Lehoucq, Richard B, Sorensen, Danny C & Yang, Chao 1998 *ARPACK users' guide: solution of large-scale eigenvalue problems with implicitly restarted Arnoldi methods*, , vol. 6. Siam.

Lessen, Martin & Singh, Pawan Jit 1973 The stability of axisymmetric free shear layers. *Journal of Fluid Mechanics* **60** (3), 433–457.

MOLLENDORF, J. C. & GEBHART, B. 1973 An experimental and numerical study of the viscous stability of a round laminar vertical jet with and without thermal buoyancy for symmetric and asymmetric disturbances. *Journal of Fluid Mechanics* **61** (2), 367–399.

MORRIS, PHILIP J. 1976 The spatial viscous instability of axisymmetric jets. *Journal of Fluid Mechanics* **77** (3), 511–529.

PAI, SI 1951 On the stability of two-dimensional laminar jet flow of gas. *Journal of the Aeronautical Sciences* **18** (11), 731–742.

QADRI, UBAID ALI & SCHMID, PETER J. 2017 Effect of nonlinearities on the frequency response of a round jet. *Physical Review Fluids* **2** (4), 1–14.

REYNOLDS, A J 1962 Observations of a liquid-into-liquid jet. *Journal of Fluid Mechanics* **14** (4), 552–556.

SIPP, DENIS & MARQUET, OLIVIER 2013 Characterization of noise amplifiers with global singular modes: The case of the leading-edge flat-plate boundary layer. *Theoretical and Computational Fluid Dynamics* **27** (5), 617–635.

TATSUMI, T. & KAKUTANI, T. 1958 The stability of a two dimensional laminar jet .

TYNDALL, F.R.S. 1867*a* On the action of sonorous vibrations on gaseous and liquid jets. *The London, Edinburgh, and Dublin Philosophical Magazine and Journal of Science* **33** (224), 375–391.

TYNDALL, JOHN 1867*b* On sounding and sensitive flames. *Philosophical Magazine* **33** (221), 92–99.

VIILU, ANDRUS 1962 An Experimental Determination of the Minimum Reynolds Number for Instability in a Free Jet. *J. Appl. Mech.* **29** (5), 506–508.

CHAPTER

FOUR

Linear stability of Clarke-Riley diffusion flames

Contents

In this chapter, we are concerned with the buoyancy-driven horizontal boundary-layer flow that forms when a semi-infinite horizontal fuel surface is burned in a quiescent oxidizing atmosphere. This flow is known to be unstable with small disturbances, whose prevalence is observed downstream from a characteristic distance to the edge. The instability typically develops either in the form of stationary counter-rotating vortex rolls along the streamwise direction, or in the form of Tollmien-Schlichting-like traveling waves driven by shear. In the literature on fire research, the former are known as 'toe vortices', since they appear at the edge of the base of large pool fires, where such a boundary-layer flow exists.

The self-similar structure of the laminar boundary-layer flow was first described by Clarke & Riley (1976) in the Burke-Schumann limit of infinitely fast reaction. Their analysis was performed for unity reactant Lewis numbers, with the viscosity and thermal conductivity being linearly proportional to the temperature. In this chapter we extend this preliminary work by considering fuels with non-unity Lewis numbers and gas mixtures with a realistic power-law dependence of the different transport properties. The problem is formulated in terms of chemistry-free, Shvab-Zel'dovich, linear combinations of the temperature and reactant mass fractions, not changed directly by the reactions, as conserved scalars.

The resulting self-similar base-flow solution is then used in a temporal linear stability analysis to determine the critical value of the boundary-layer thickness—measured by the local Grashof number, and directly related to the distance from the edge of the

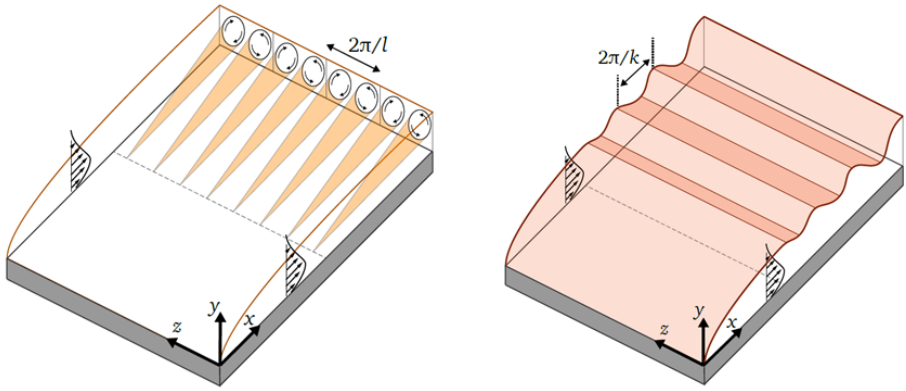

Figure 4.1: The two types of instabilities considered in the Clarke-Riley diffusion flame near the edge of a burning fuel surface: (left) the vortex mode, i.e. stationary counterrotating vortical structures aligned with the stream, and (right) the wave mode, i.e. Tollmien-Schlichting-like traveling waves.

fuel surface—at which the flow becomes unstable to either of the modes of instability described before. The analysis is carried out for three realistic fuels: methanol, heptane, and dodecane.

The chapter starts with a brief literature review. Next, in section 4.2 we present a mathematical formulation of the self-similar flow under consideration, and describe the temporal local linear stability analysis that was carried out. The numerical methods employed to obtain the basic flow and to solve the eigenvalue problem for the linear stability analysis are discussed in section 4.3. Results are presented and discussed in section 4.4. Finally, concluding remarks and future developments are given in section 4.5.

4.1 Introduction

When a semi-infinite horizontal fuel surface is burned in quiescent ambient of air, a buoyancy-driven boundary-layer flow forms starting at the edge of the surface. In this dissertation, we will refer to this flow with the term “Clarke-Riley diffusion flame”, in honor of Clarke & Riley (1976), who were the firsts to describe its self-similar structure in a formal manner.

In real-life situations, the Clarke-Riley flow can be encountered for example at the edge of large pool fires or wildfires (Finney *et al.* (2015)). This boundary-layer flow is known to be very susceptible to instabilities. In particular, two types of instabilities are prevalent. The first type are stationary counterrotating vortical structures, aligned with the stream, similar to the Görtler instability of flow over a concave surface (Gortler

(1954)). In the latter, the instabilities are driven by the centrifugal force, whereas in the present configuration, it is the buoyancy force that plays this role. For shortness, this mode of instability will henceforth be named the *vortex mode*. In the fire literature, when this instability is present at the base of a large pool fire, the vortical structures are often called "toe vortices". The second type of instabilities are Tollmien-Schlichting-like traveling waves (Schubauer (1947)), which will be shortened in what follows as the *wave mode*. Figure 4.1 gives a schematic representation of the vortex mode on the left, and the wave mode on the right-hand-side.

In wildfires, which are typically very turbulent in nature, these instabilities lead to coherent structures that are advected away from the edge and can feed or interact with the large-scale puffing behavior of the fire. Miller *et al.* (2017) has analyzed such coherent structures in boundary-layer flames in the context of wildfires.

The Clarke-Riley flow shares many characteristics with other natural-convection-driven flows, such as the boundary-layer flow over an horizontal or an inclined plate, a simpler configuration which has been given more attention in the literature. In that context, the first study dates back to Schmidt & Beckmann (1930), who already found that the boundary layer far away from the leading edge presents a self-similar structure.

Sparrow & Husar (1969) found that the laminar free convection flow over an inclined heated plate is unstable to both vortex and wave perturbation modes. Lloyd & Sparrow (1970) showed that there is a secondary flow in the natural convection flow over a hot plate that creates longitudinal vortices. Hwang & Cheng (1973) analyzed the case of natural convection over an isothermal inclined plate using a linear stability analysis under te Boussinesq and non-parallel flow assumptions. Jones (1973) studied the hot inclined surface, and found that when the inclination is positive, two solutions appear: one that is valid close to the leading edge, and another one far way from it.

Lloyd & Sparrow (1970) observed also in the case of hot inclined plates that for any angle greater than 17 degrees from the vertical, the vortex mode is dominant, while when the angle is less than 14 is the wave mode that dominates. Between 14 and 17 degrees there is a transition zone where both modes coexist. Later, Kahawita & Meroney (1974) confirmed these observations for a gaseous flow with Prandtl number $Pr = 0.72$. Iyer & Kelly (1974) examined this inclined plate for $Pr = 6.7$ and saw the transition taking place at 4 degrees. Another experimental work that found both instabilities to exist in the flow over hot inclined plates is that of Haaland & Sparrow (1973*a*) and Haaland & Sparrow (1973*b*). Rotem & Claassen (1969) showed experimentally that when a horizontal surface is heated, a laminar boundary layer is formed at moderate Grashof numbers. This boundary layer breaks at some distance from the leading edge into instabilities. Other relevant works include that of Pera & Gebhart (1973*a*), and Pera & Gebhart (1973*b*) who analyzed the stability over horizontal or slightly inclined plates finding discrepancies between the experiments and the predictions of linear stability theory, and the analytical study of Chen & Tzuoo (1982). Last year Rajamanickam *et al.*

(2017) analyzed the linear stability of the flow over a hot inclined surface considering non-Boussinesq effects, including nonparallel effects of the base flow.

The self-similar structure of the boundary-layer diffusion flame under consideration here was first described by Clarke & Riley (1976). Their analysis employed the Burke-Schumann limit of infinitely fast reaction, and was performed for unity reactant Lewis numbers, with the viscosity and thermal conductivity taken to be linearly proportional to the temperature.

This work has two main objectives. First, the formulation of Clarke & Riley (1976) is to be generalized to take into account a non-unity Lewis number, a realistic power-law dependence of the different transport properties with the temperature, as well as an equation of state that accounts for the difference in molecular weight between the fuel vapor and the ambient air. These generalizations are necessary to give accurate results for hydrocarbon fuels such as heptane and dodecane.

The second objective is to perform a linear stability analysis of the resulting flow. Since such an analysis has not been carried out before in the literature, we opt here to start with the conceptually simplest approach: a strictly parallel temporal local linear stability analysis. The self-similar boundary-layer description, which directly depends on the thermochemical parameters of the fuel, is used as the basic flow for the stability analysis, which only depends on the Grashof number. This Grashof number is uniquely related to the streamwise distance to the edge of the fuel surface. Therefore, by computing the critical Grashof number above which small perturbations can grow, we can give a prediction for the streamwise distance from the edge at which the instability can be expected to set in. This analysis will be carried out for the two types of instabilities described before, namely the vortex mode and the wave mode.

The outline of the remainder of this chapter is as follows. In section 4.2, we give the complete mathematical formulation of the problem, encompassing the derivation of the conservation equations for the flame, the self-similar description, and the linear stability analysis. Section 4.3 treats the numerical methods employed to obtain the results. Finally, in section 4.4 we show the results of our analysis, presenting first the solution of the basic flow field, followed by the result of the linear stability analysis. Finally, section 4.5 is dedicated to conclusions and a discussion of future work.

4.2 Formulation

4.2.1 Conservation equations, boundary conditions, and conserved scalars for the Clarke-Riley diffusion flame

We consider the burning of a semi-infinite fuel surface in a quiescent air atmosphere, as depicted in figure 4.2. The properties of the ambient are denoted with the subscript ∞. The flow is described in terms of the cartesian coordinates $\boldsymbol{x} = (x, y, z)$, with

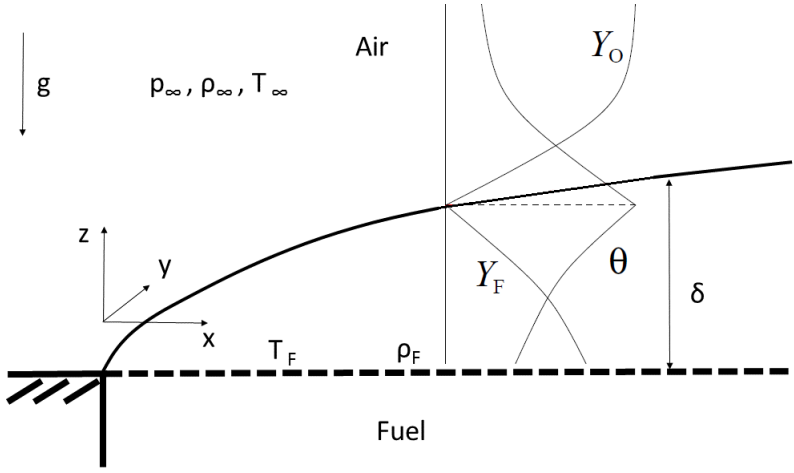

Figure 4.2: Problem representation of the flame including fuel and air variables

corresponding velocities $\boldsymbol{v} = (v_x, v_y, v_z)$. Here we consider the unperturbed planar flow, so that $v_y = 0$ and the flow variables do not depend on y. Later, in the linear stability analysis, we will consider modes of instability that do vary in the spanwise direction y.

The reaction between the fuel and the oxygen from the atmosphere is considered as global irreversible step

$$\mathrm{F} + s\mathrm{O}_2 \rightarrow (1+s)\mathrm{P} + q', \tag{4.1}$$

where s and q' are the mass of oxygen consumed and the heat released per unit mass of fuel F burnt; P indicates the created products of combustion. In the low-Mach number equations, these thermochemical parameters appear as $S = s/Y_{O_2,\infty}$ and $q = q'/(c_p T_\infty)$, involving the mass fraction of oxygen in air $Y_{O_2,\infty} \simeq 0.232$, the ambient temperature T_∞, and the specific heat at constant pressure c_p which is assumed to be constant. The parameter $S \approx 17$, represents the oxygen needed to burn fuel per unit mass. The dimensionless heat release per unit mass of fuel q, scaled with the ambient enthalpy, takes large values for usual fuels, such that $q/S \sim 8$.

Besides the continuity and momentum equations

$$\frac{\partial \rho}{\partial t} + \nabla \cdot \rho \boldsymbol{v} = 0, \tag{4.2}$$

$$\rho \frac{\partial \boldsymbol{v}}{\partial t} + \rho \boldsymbol{v} \cdot \nabla \boldsymbol{v} = -\nabla p + (\rho_\infty - \rho) g \boldsymbol{e}_z + \nabla \cdot [\mu(\nabla \boldsymbol{v} + \nabla \boldsymbol{v}^T)] \tag{4.3}$$

the description involves the conservation equations for reactants and energy

$$\rho\frac{\partial Y_F}{\partial t}+\rho\boldsymbol{v}\cdot\nabla Y_F=\frac{1}{Le_F}\nabla\cdot(\rho\kappa\nabla Y_F)-w_F, \tag{4.4}$$

$$\rho\frac{\partial Y_O}{\partial t}+\rho\boldsymbol{v}\cdot\nabla Y_O=\nabla\cdot(\rho\kappa\nabla Y_O)-Sw_F, \tag{4.5}$$

$$\rho\frac{\partial}{\partial t}\left(\frac{T}{T_\infty}\right)+\rho\boldsymbol{v}\cdot\nabla\left(\frac{T}{T_\infty}\right)=\nabla\cdot\left[\rho\kappa\nabla\left(\frac{T}{T_\infty}\right)\right]+qw_F, \tag{4.6}$$

with w_F representing the mass of fuel consumed by the chemical reaction per unit volume and per unit time. In the formulation Y_F and $Y_O = Y_{O_2}/Y_{O_{2,\infty}}$ are the mass fraction of fuel vapor and the normalized mass fraction of oxygen, while T, ρ, μ, and κ represent the temperature, density, viscosity, and thermal diffusivity of the gas. The motion induced is very slow, involving small pressure variations that can be dismissed in the first approximation when it is defined the equation of state

$$\frac{\rho}{\rho_\infty}\frac{T}{T_\infty}=\left[Y_F\left(\frac{W_\infty}{W_F}-1\right)+1\right]^{-1}, \tag{4.7}$$

which takes into account the large variations of the molecular mass of the fuel W_F from that of the air W_∞. The small pressure variations must be accounted for in (4.3), where p represents the pressure difference from the hydrostatic pressure distribution found as $x\to-\infty$ with g representing the gravitational acceleration. The presumed power laws

$$\frac{\mu}{\mu_\infty}=\frac{\rho\kappa}{\rho_\infty\kappa_\infty}=\left(\frac{T}{T_\infty}\right)^\sigma \tag{4.8}$$

will be used below for the temperature variation of the transport properties, being $\sigma=0.7$ used in the calculations. The description considers non-unity values of the Lewis number is defined as the ratio between the thermal diffusivity and the molecular diffusivity of the fuel. This parameter is needed to improve accuracy in computations of most hydrocarbon fuels. On the other hand, to describe the transport of oxygen, a unity Lewis number has been used, which is a good approximation for the majority of conditions.

The boundary conditions in the surrounding air atmosphere can be written in the form

$$v_x=v_z=p=T-T_\infty=Y_F=Y_O-1=0 \quad \text{as} \quad (x^2+z^2)\to\infty \quad \text{for} \quad z\neq 0. \tag{4.9}$$

The surface $x<0$, $z=0$ is assumed to be impermeable and chemically inert, thereby providing the additional boundary conditions

$$v_x=v_z=\frac{\partial T}{\partial z}=\frac{\partial Y_F}{\partial z}=\frac{\partial Y_O}{\partial z}=0. \tag{4.10}$$

Fuel vaporization occurs at a defined boiling temperature T_B with latent heat of vaporization L_v. The energy used to increase the temperature of the liquid fuel, with specific heat c_l, from the ambient temperature to boiling is taken into account by defining a dimensionless heat of vaporization $l_v = [L_v + c_l(T_B - T_\infty)]/(c_p T_\infty)$. The resulting boundary conditions on the vaporizing fuel surface (i.e. at $z = 0$ for $x > 0$) are

$$u = T - T_B = 0 \tag{4.11}$$

$$\rho v_z Y_F - \frac{\rho\kappa}{Le_F}\frac{\partial Y_F}{\partial z} = \rho w \tag{4.12}$$

$$\rho v_z Y_O - \rho\kappa\frac{\partial Y_O}{\partial z} = 0 \tag{4.13}$$

$$\rho v_z\left(\frac{T}{T_\infty}\right) - \rho\kappa\frac{\partial}{\partial y}\left(\frac{T}{T_\infty}\right) = -l_v\rho w, \tag{4.14}$$

As in Clarke & Riley (1976) present analysis uses the fast-reaction limit in which the chemical-reaction terms in (4.4)–(4.6) appear as Dirac delta distributions along a flame surface that separates the outer region with oxygen and no fuel vapor from an inner region with fuel and no oxygen. For the analysis of the fast-reaction limit it is convenient to replace two of the equations (4.4)–(4.6) by two chemistry-free conservation equations, obtained by eliminating the reaction terms through appropriate linear combinations (Liñán *et al.* (2015)). We follow the derivation given in Liñán *et al.* (2017) for the analysis of counterflow gaseous diffusion flames. Thus multiplying (4.5) by q/S and adding (4.6) leads to a chemistry-free conservation equation (see Sánchez *et al.* (1997); Zeldovich (1951)) involving a single coupling function $(T + qY_O/S)$, which can be conveniently described as a normalized excess thermal and chemical enthalpy

$$\xi = \frac{(T/T_\infty) - 1 + (q/S)(Y_O - 1)}{(T_B/T_\infty) - 1 - q/S} \tag{4.15}$$

with transport equation

$$\rho\frac{\partial\xi}{\partial t} + \rho\boldsymbol{v}\cdot\nabla\xi = \nabla\cdot(\rho\kappa\nabla\xi). \tag{4.16}$$

using the normalization used in (4.15) the excess enthalpy ξ is null in the atmosphere and unity on the fuel surface.

The reaction component can also be eliminated by subtracting (4.5) from (4.4) and multiplying by S. When the Lewis number Le_F is non-unity, the resulting transport equation shows a coupling function $(SY_F - Y_O)$ in the accumulation and convective terms that is different from the coupling function $(SY_F/Le_F - Y_O)$ appearing in the diffusion term. Normalizing this coupling functions we find a diffusion-weighted mixture fraction

$$\tilde{Z} = \frac{SY_F/Le_F - Y_O + 1}{S/Le_F + 1}, \tag{4.17}$$

in addition with the mixture fraction

$$Z = \frac{SY_F - Y_O + 1}{S+1}, \tag{4.18}$$

with resulting conservation equation

$$\rho \frac{\partial Z}{\partial t} + \rho \boldsymbol{v} \cdot \nabla Z = \frac{1}{Le} \nabla \cdot (\rho \kappa \nabla \tilde{Z}). \tag{4.19}$$

where $Le = (S+1)/(S/Le_F + 1)$. To solve (4.16) and (4.19) coupled with (4.2) and (4.3) and supplemented with (4.7) and (4.8) we need to relate T, Y_F, and Z with ξ and $\tilde{Z}$. These relations can be obtained using the fast-reaction condition

$$Y_F Y_O = 0 \tag{4.20}$$

of non-coexistence of Y_O and Y_F, which are simultaneously zero at the flame, given by the $Z = Z_S = 1/(1+S)$, or $\tilde{Z} = \tilde{Z}_S = 1/(1+S/Le_F)$, from the definitions (4.17) and (4.18). For $\tilde{Z} \geq \tilde{Z}_S$

$$Y_O = 0 \quad \text{and} \quad Y_F = \frac{Z - Z_S}{1 - Z_S} = \frac{\tilde{Z} - \tilde{Z}_S}{1 - \tilde{Z}_S}, \quad \frac{T}{T_\infty} - 1 = \left(\frac{T_B}{T_\infty} - 1 \right) \xi + \frac{q}{S}(1 - \xi), \tag{4.21}$$

whereas for $\tilde{Z} \leq \tilde{Z}_S$

$$Y_F = 0 \quad \text{and} \quad 1 - Y_O = \frac{Z}{Z_S} = \frac{\tilde{Z}}{\tilde{Z}_S}, \quad \frac{T}{T_\infty} - 1 = \left(\frac{T_B}{T_\infty} - 1 \right) \xi + \frac{q}{S} \left(\frac{\tilde{Z}}{\tilde{Z}_S} - \xi \right). \tag{4.22}$$

Equations (4.21) and (4.22) provide piece-wise linear relations for the evaluation of Y_F, Y_O, and Z in terms of $\tilde{Z}$. Moreover, last equations relates the temperature with $\tilde{Z}$ and ξ. In terms of ξ and $\tilde{Z}$, the boundary conditions (4.9)–(4.11) become

$$v_x = v_z = p = \xi = \tilde{Z} = 0 \quad \text{as} \quad (x^2 + z^2) \to \infty \quad \text{for} \quad z \neq 0 \tag{4.23}$$

$$v_x = v_z = \frac{\partial \xi}{\partial z} = \frac{\partial \tilde{Z}}{\partial z} = 0 \quad \text{at} \quad z = 0 \quad \text{for} \quad x < 0 \tag{4.24}$$

$$\left.\begin{aligned} v_x = \xi - 1 = 0 \\ -\rho\kappa \frac{\partial \xi}{\partial z} = \alpha \rho v_z \\ -\rho\kappa \frac{\partial \tilde{Z}}{\partial z} = Le_F \rho v_z (1 - \tilde{Z}) \end{aligned}\right\} \quad \text{at} \quad z = 0 \quad \text{for} \quad x > 0, \tag{4.25}$$

where

$$\alpha = \frac{l_v + T_B/T_\infty}{q/S + 1 - T_B/T_\infty}, \tag{4.26}$$

thereby completing the definition of the problem.

In our analysis, the results of which will be presented in section 4.4, we consider three fuels: methanol, heptane, and dodecane. Table 4.1 summarizes the values of the dimensionless thermochemical parameters introduced in the description for these fuels.

	Methanol	Heptane	Dodecane
Molecular mass W_{F}	0.9091	0.2899	0.1706
Latent heat of evaporation l_v	2.62	0.8	0.8
Boiling temperature T_{B}	1.12	1.24	1.63
Lewis number Le_{F}	1.2	2.6	3.6
Heat release parameter q/S	7.7	7	7

Table 4.1: Values of the dimensionless thermochemical parameters used in the description, for methanol, heptane and dodecane. Evaluated with properties taken from Lide (2001).

4.2.2 The base flow – self-similar structure

We shall begin by describing the steady solution of the flow, which provides the base flow needed for the following stability analysis. Straightforward order-of-magnitude estimates in the momentum equation reveal that the flow induced by buoyancy has a local Reynolds number of order unity in a non-slender Navier–Stokes region of characteristic size $(\nu_\infty^2/g)^{1/3}$ around the fuel surface edge, where $\nu_\infty = \mu_\infty/\rho_\infty$ is the kinematic viscosity of the ambient air. Away from this Navier–Stokes region the flow field displays a distinct structure, including a boundary layer containing the diffusion flame adjacent to fuel surface and an outer inviscid region of slow motion driven by the boundary-layer entrainment.

The analysis below pertains to the structure of the boundary layer developing at distances $x \gg (\nu_\infty^2/g)^{1/3}$, where the resulting solution is self-similar, as shown by Clarke & Riley (1976). The characteristic boundary-layer thickness

$$\delta = (\nu_\infty^2 x^2/g)^{1/5}. \tag{4.27}$$

will be used in scaling the distance from the surface in the definition of the self-similar coordinate

$$\eta = z/\delta = z/(\nu_\infty^2 x^2/g)^{1/5}. \tag{4.28}$$

The velocity field will be described in terms of the stream function

$$\psi = \rho_\infty (g\,\nu_\infty^3 x^{3/5})^{1/5} F(\eta), \tag{4.29}$$

defined such that

$$\rho v_x = \rho_\infty (g^2 \nu_\infty x)^{1/5} F' \tag{4.30}$$

and

$$\rho v_z = \rho_\infty (g\nu_\infty^3/x^2)^{1/5}\left(\frac{2}{5}\eta F' - \frac{3}{5}F\right) \tag{4.31}$$

where the prime denotes differentiation with respect to η. The accompanying pressure distribution is given in terms of the self-similar variable $\Pi(\eta)$ by

$$p = \rho_\infty (g^2\nu_\infty x)^{2/5}\Pi(\eta). \tag{4.32}$$

In terms of these variables, the longitudinal and transverse components of the momentum equation can be written in the dimensionless form

$$\left[\theta^\sigma\left(\frac{F'}{R}\right)'\right]' + \frac{3F}{5}\left(\frac{F'}{R}\right)' - \frac{F'^2}{5R} + \frac{2}{5}(\eta\Pi' - \Pi) = 0 \tag{4.33}$$

$$\Pi' + R - 1 = 0, \tag{4.34}$$

whereas the conservation equations for the conserved scalars become

$$\left(\theta^\sigma \xi'\right)' + \frac{3}{5}PrF\xi' = 0 \tag{4.35}$$

$$\left(\theta^\sigma \tilde{Z}'\right)' + \frac{3}{5}PrLeFZ' = 0 \tag{4.36}$$

where $\theta = T/T_\infty$ and $R = \rho/\rho_\infty$, while $Pr = \mu/(\rho\kappa)$ is the Prandtl number. Equations (4.33)–(4.36) must be integrated subject to the boundary conditions

$$F' = \Pi = \xi = \tilde{Z} = 0 \quad \text{as} \quad \eta \to \infty \tag{4.37}$$

$$F' = \xi - 1 = 0 \quad \text{and} \quad \frac{3}{5}Pr\theta_{\text{B}}^{-\sigma}F = \xi'/\alpha = \frac{\tilde{Z}'}{Le_{\text{F}}(1-\tilde{Z})} \quad \text{at} \quad \eta = 0, \tag{4.38}$$

where $\theta_{\text{B}} = T_{\text{B}}/T_\infty$. In the integration, the functions Z, R, and θ are to be evaluated with use made of (4.7), (4.21), and (4.22) from

$$Z = \tilde{Z}/Le \quad \text{for} \quad \tilde{Z} \le \tilde{Z}_{\text{S}} \quad \text{and} \quad Z = Z_S + (Le_{\text{F}}/Le)(\tilde{Z} - \tilde{Z}_{\text{S}}) \quad \text{for} \quad \tilde{Z} \ge \tilde{Z}_{\text{S}} \tag{4.39}$$

and

$$\theta = R^{-1} = 1 + (\theta_{\text{B}} - 1)\xi + (q/S)(\tilde{Z}/\tilde{Z}_{\text{S}} - \xi) \quad \text{for} \quad \tilde{Z} \le \tilde{Z}_{\text{S}} \tag{4.40}$$

$$\theta = R^{-1}\left[\frac{\tilde{Z} - \tilde{Z}_{\text{S}}}{1 - \tilde{Z}_{\text{S}}}\left(\frac{W_\infty}{W_{\text{F}}} - 1\right) + 1\right]^{-1} = 1 + (\theta_{\text{B}} - 1)\xi + (q/S)(1 - \xi) \quad \text{for} \quad \tilde{Z} \ge \tilde{Z}_{\text{S}}. \tag{4.41}$$

The self-similar base flow profiles are obtained from solving (4.33)–(4.41) with a single computation for each fuel. The numerical methods employed for these

computations are described in section 4.3, and the results are presented in section 4.4. The profiles are then used to study the linear stability of the flow at a certain location x, which is reflected in the analysis through the value of the local Grashof number defined as

$$Gr = \frac{g\delta^3}{\nu_\infty^2} = \left(\frac{gx^3}{\nu_\infty^2}\right)^{2/5} = \left(\frac{x}{\delta}\right)^{2/5}, \tag{4.42}$$

which is also the square of the Reynolds number based on the local values of the boundary-layer thickness δ and the streamwise velocity $(g\delta)^{1/2}$. We anticipate that the stability analysis will predict a large value of the critical Grashof number, so that the boundary-layer description is valid. This will be assessed when we present the results in section 4.4. In the next section we present the details of the stability analysis.

4.2.3 Linear stability analysis

The linear stability of the flow at the streamwise location x is investigated by introducing small perturbations $\mathcal{O}(\varepsilon)$ around a steady base flow in the complete governing equations of motion (4.2)–(4.6). The latter are nondimensionalized using the local boundary-layer thickness δ, the local characteristic streamwise velocity $(g\delta)^{1/2}$, the convective time scale $\delta/(g\delta)^{1/2}$, the hydrostatic pressure difference $\rho_\infty g\delta$, and the ambient values for the fluid properties ρ_∞, ν_∞. The decomposition takes the form

$$\left(v_x, v_y, v_z, p, Z, \xi\right) = \left(\overline{v_x}, \overline{v_y}, \overline{v_z}, \overline{p}, \overline{Z}, \overline{\xi}\right) + \varepsilon\left(v_x', v_y', v_z', p', Z', \xi'\right). \tag{4.43}$$

The stability analysis must contemplate the vortex mode of instability, in which disturbances take the form of stationary counter-rotating vortices aligned with the flow (see figure 4.1(a)), as well as the wave mode of instability, in which the disturbances take the form of traveling Tollmien-Schlichting-like waves (see figure 4.1(b)). Therefore, the perturbations are expressed as normal modes in the general form

$$\left(v_x', v_y', v_z', p', Z', \xi'\right) = \left(\widehat{v_x}, \widehat{v_y}, \widehat{v_z}, \widehat{\rho}, \widehat{Z}, \widehat{\xi}\right)(z)e^{i(kx+ly-\omega t)}, \tag{4.44}$$

where $\omega = \omega_r + \mathrm{i}\omega_i$ contains the dimensionless frequency and growth rate of the perturbation, and k and l are the dimensionless real wavenumbers in the streamwise and spanwise direction, respectively. This means that $k = 0$ pertains to the vortex mode of instability, whereas $l = 0$ corresponds to the wave mode. In the temporal stability analysis employed in this work, k or l are given, and ω is found as an eigenvalue. If $\omega_i < 0$, the flow is stable, whereas if $\omega_i > 0$, the flow is unstable to perturbations of that wavenumber k or l. By sweeping over all values of k or l, and keeping track of how the maximum value of the growth rate $\omega_{i,max}$ changes with the Grashof number Gr, we can find the critical value of the Grashof number Gr_c, i.e. the value of Gr for which $\omega_{i,max} = 0$.

Upon introduction of the normal modes into the governing equations, and after

linearization around the basic flow (neglecting terms $\mathcal{O}(\varepsilon^2)$), we obtain the following set of stability equations:

$$\omega\widehat{\rho} = \overline{\rho}\; l\; \widehat{v_y} + \left(\overline{\rho}D + \partial_z\overline{\rho}\right)\widehat{v_z}, \tag{4.45}$$

$$i\omega\overline{\rho}\;\widehat{v_x} = i\;\overline{\rho}\;\partial_z\overline{v_x}\;\widehat{v_z} - \frac{1}{Gr^{1/2}}\left(D^2 - l^2\right)\widehat{v_x}, \tag{4.46}$$

$$i\omega\overline{\rho}\;\widehat{v_y} = i\;l\;\widehat{p} - \frac{1}{Gr^{1/2}}\left(D^2 - l^2\right)\widehat{v_y}, \tag{4.47}$$

$$i\omega\overline{\rho}\;\widehat{v_z} = -i\;D\widehat{p} - \frac{1}{Gr^{1/2}}\left(D^2 - l^2\right)\widehat{v_z} - i\widehat{\rho}, \tag{4.48}$$

$$i\omega\overline{\rho}\;\widehat{Z} = i\;\overline{\rho}\;\partial_z\overline{Z}\;\widehat{v_z} - \frac{1}{Pr\;Gr^{1/2}\;Le}\left(D^2 - l^2\right)\widehat{\tilde{Z}}, \tag{4.49}$$

$$i\omega\overline{\rho}\;\widehat{\xi} = i\;\overline{\rho}\;\partial_z\overline{\xi}\;\widehat{v_z} - \frac{1}{Pr\;Gr^{1/2}}\left(D^2 - l^2\right)\widehat{\xi}, \tag{4.50}$$

where the operator D indicates vertical derivatives $\mathrm{d}/\mathrm{d}z$. Note that $\widehat{\rho}$ can be expressed in terms of $\widehat{\xi}$ and $\widehat{\tilde{Z}}$ using the piecewise linear relations (4.21) and (4.22) presented in section 4.2.

The base flow variables are directly obtained from the solution of the self-similar boundary-layer problem (4.33)–(4.41): the dimensionless z-coordinate in the stability problem is equal to the similarity coordinate η, the streamwise velocity $\overline{v_x} = \dfrac{1}{\overline{\rho}}\dfrac{\mathrm{d}F}{\mathrm{d}\eta}$, and the density $\overline{\rho}$ is related to $\overline{\tilde{Z}}$ and $\overline{\xi}$ using the piecewise relations (4.21) and (4.22) given earlier.

Note that in the strictly parallel flow assumption, $\overline{v_y} = \overline{v_z} = 0$. It would be possible to include so-called non-parallel terms that involve streamwise derivatives of $\overline{v_x}$ and $\overline{\rho}$, as well as the transverse velocity $\overline{v_z}$. These terms would enter the stability equations at $\mathcal{O}(Gr^{-1/2})$, which is the same order than the viscous terms. This was done, for example, by Rajamanickam *et al.* (2017) in a study of the linear stability of the natural convection flow over a heated inclined plate, who found that the inclusion of the non-parallel terms resulted in small, but noticeable quantitative changes in the predicted critical Grashof numbers.

The stability equations must be accompanied by appropriate boundary conditions. In the far field, $(\widehat{p}, \widehat{v_x}, \widehat{v_y}, \widehat{v_z}, \widehat{\tilde{Z}}, \widehat{\xi}) \to 0$ as $z \to \infty$; at the fuel surface, $\widehat{p} = \widehat{v_x} = \widehat{v_y} = \widehat{\xi} = 0$, and

$$\left(D^2 - l^2\right)\widehat{\tilde{Z}} = Pr\;Gr^{1/2}\;Le\;i\;\overline{\rho}\;\partial_z\overline{\tilde{Z}}\widehat{v_z}, \tag{4.51}$$

$$\left(D^2 - l^2\right)\widehat{\xi} = Pr\;Gr^{1/2}\;i\;\overline{\rho}\;\partial_z\overline{\xi}\widehat{v_z}, \tag{4.52}$$

the latter conditions stemming from the mass and energy balance (4.25) that dictates the fuel evaporation at the surface.

4.3 Numerical method

4.3.1 Base flow

The solution of (4.33)–(4.41) to obtain the self-similar base-flow profiles is complicated by a discontinuity in the derivatives of the density and temperature at the stoichiometric line, where $Z = Z_s$. The location η_s where this occurs is part of the solution and unknown a priori. To overcome this difficulty, a rescaled coordinate ζ is introduced as

$$\zeta = \frac{\eta}{\eta_s} \tag{4.53}$$

so that the stoichiometric point is situated at $\zeta = 1$. This introduces the new variable η_s in the stability equations, which are now written as

$$5\left[\mu\left(\frac{1}{R}F'\right)'\right]' + 3\eta_s F\left(\frac{1}{R}F'\right)' - \frac{\eta_s^2}{R}\left(F'\right)^2 + 2\eta_s^3\left(\zeta\Pi' - \Pi\right) = 0 \tag{4.54}$$

$$\Pi' + \eta_s\left(R-1\right) = 0 \tag{4.55}$$

$$5\left(\theta^\sigma \tilde{Z}'\right)' + 3\,Pr\;\eta_s\;Le\;F\;Z' = 0 \tag{4.56}$$

$$5\left(\theta^\sigma \xi'\right)' + 3\,Pr\;\eta_s\;F\;\xi' = 0 \tag{4.57}$$

where the prime denotes the derivative $\mathrm{d}/\mathrm{d}\zeta$. Equations (4.54)–(4.57) are then solved in the separate domains (I) $0 \le \zeta \le 1$ (the fuel side where $Z > Z_s$), and (II) $1 \le \zeta \le \infty$ (the air side where $Z < Z_s$). The eight boundary conditions for each of the two numerical integrations are

$$\zeta = \zeta_{max} : \left\{\; Z = 0, \xi = 0, \Pi = 0, F' = 0 \right. \tag{4.58}$$

$$\zeta = 1 : \left\{\; Z = Z_s, \xi = \xi_s, F = F_s, F' = \dot{F}_s \right. \tag{4.59}$$

$$\zeta = 0 : \begin{cases} \xi = 1, F' = 0 \\ \xi' = \frac{3}{5} Pr\;\eta_s(\alpha - 1)\frac{F}{\theta^\sigma} \\ Z' = \frac{3}{5} Le\;Pr\;\eta_s(1-Z)\frac{F}{\theta^\sigma} \end{cases} \tag{4.60}$$

Note that the domain on the air side is bounded by a certain large value ζ_{max}. It was ensured that the value $\zeta_{max} = 50$ that was used in the integrations, is sufficiently large. In each domain, the system of ordinary differential equations with the corresponding boundary conditions was solved using a Chebyshev spectral collocation method. To that aim, the MATLAB library *chebfun* was employed (see, Trefethen (2013)).

By separating the complete integration into two problems, we have introduced, apart from η_s, three additional unknown variables, which are the values of F, $\mathrm{d}F/\mathrm{d}\zeta$, and ξ at $\zeta = 1$, named F_s, $\dot{F}_s$, and ξ_s. These four unknowns are determined by the four

requirements that the pressure Π, the first derivatives $\mathrm{d}\xi/\mathrm{d}\zeta$ and $\mathrm{d}\tilde{Z}/\mathrm{d}\zeta$, and the second derivative $\mathrm{d}^2F/\mathrm{d}\zeta^2$ be continuous at $\zeta = 1$, as is required by the highest order derivatives in the system of differential equations. This nonlinear root-finding problem is solved with a standard Newton-Raphson algorithm.

4.3.2 Stability analysis

The stability equations (4.45)–(4.49) are discretized using a standard Chebyshev spectral collocation method using N Gauss-Lobatto discretization points on the computational domain $[-1, 1]$. The computational domain is mapped to the physical domain $[0, z_{\max}]$ using the mapping

$$y = z_0 \frac{1-\xi}{\xi + 2z_0/z_{\max}}; \tag{4.61}$$

where z_0 is a clustering parameter (see Khorrami *et al.* (1989)). In the present work, we found that $N = 128$, $z_0 = 100$, and $z_{\max} = 500$ gave well-converged results.

Upon discretization, the stability equations (4.45)–(4.49) can be written as an eigenvalue problem

$$Aq = \omega Bq, \tag{4.62}$$

for the complex eigenvalue ω. A and B are the discretized operators associated with (4.45)–(4.49) that depend on k or l, on the Grashof number Gr, and on the base flow, which indirectly depends on the fuel type. $q = (\widehat{p}, \widehat{v_x}, \widehat{v_y}, \widehat{v_z}, \widehat{\xi}, \widehat{\tilde{Z}})$ is the eigenvector associated with the eigenvalue ω that contains the spatial structure of the perturbations. The eigenvalue problem can be solved in a straightforward manner using the MATLAB *eigs* function.

Note that for the vortex mode of instability, which manifests itself as stationary counterrotating vortex rolls aligned with the streamwise direction, $k = 0$ and $\omega_r = 0$. This means that to find, for a certain value of l, the critical Grashof number Gr_c, this can be found directly by setting $\omega = 0$ in the stability equations (4.45)–(4.49), so that these upon discretization can be written as an eigenvalue problem $A_0 q = Gr_c^{1/2} B_0 q$ for $Gr_c^{1/2}$. For the wave mode this is not possible, since the frequency ω_r is not equal to zero and must be solved for.

4.4 Results

4.4.1 Base flow

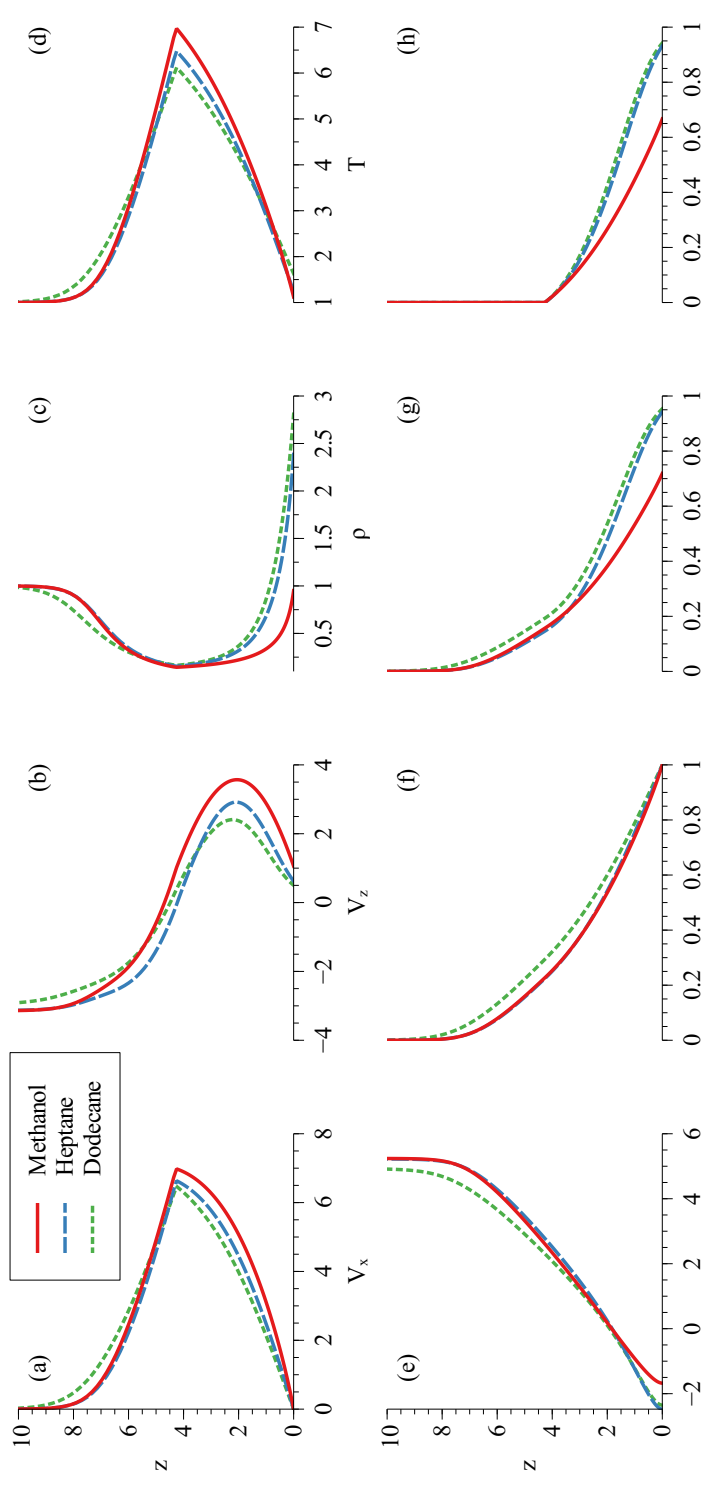

Figure 4.3: Steady base flow for methanol (solid red), heptane (long-dashed blue), and dodecane (short-dashed green). (a) Horizontal velocity v_x, (b) vertical velocity v_z, (c) density ρ, (d) temperature T, (e) stream function F, (f) excess-enthalpy ξ, (g) mixture fraction $\tilde{Z}$ and (h) fuel mass fraction Y_F.

Figure 4.3 shows the self-similar Clarke-Riley flow, computed for three different fuels: methanol (solid red lines), heptane (long-dashed blue lines), and dodecane (short-dashed green lines). The different panels (a)–(h) show different variables of interest. The dimensionless z coordinate is equal to the similarity variable η employed in the formulation of section 4.2.2. Note that in the figure only the interval $z \in [0, 10]$ is shown, but the computational domain stretched to $\zeta = z/\eta_s = 50$, which for the present results corresponds to $z \simeq 200$.

The horizontal velocity v_x in figure 4.3(a) reaches a maximum at the flame front, which is located around $z = \eta_s = 4$. This is consistent with the observations of Clarke & Riley (1976) in their study of unity-Lewis-number diffusion flames over horizontal fuel surfaces. Methanol flames are associated with a slightly larger velocity, which is also coincides with a slightly higher peak temperature at the flame front (figure 4.3(d)). In the thermochemical parameters used in the description (table 4.1), this higher value of the temperature for methanol can be traced back to the slightly higher value of the heat release parameter q/S.

The vertical velocity (4.3(b)) changes sign at the flame front, on one side bringing the evaporated fuel from the surface to the flame, and on the other side entraining the ambient air down towards the flame.

Our description of the flame takes into account the difference in molecular weight between the fuel and the air when evaluating the density. This is clear from figure 4.3(c), where for the heavy hydrocarbon fuels, heptane and dodecane, the density at the fuel surface is considerably larger ($\rho \simeq 2.5$) than that of the ambient air ($\rho = 1$). In the high-temperature flame region, the density is mainly determined by the temperature, and goes down to approximately $\rho \simeq 1/7$.

The temperature profiles of figure 4.3(d) show the expected trend, reaching a temperature of approximately 6 to 7 times the ambient temperature. In dimensional quantities, that would mean a peak flame temperature of approximately 1,800 to 2,100 K. For heptane and dodecane flames, it can be expected that heat loss due to radiation, which has not been taken into account in this work, would lower these temperatures. An ad-hoc approach to model this effect without the need of a specific radiation model would be to lower the value of the heat release parameter q/S by 10-15%, an approach recently taken by Moreno-Boza *et al.* (2018) in a study on puffing pool fires. Although the horizontal Clarke-Riley diffusion flames shares many physical aspects with the natural convection boundary-layer flow over a horizontal heated plate, the temperature profiles in the latter case are substantially different, in the sense that the peak temperature is located at the bottom wall and then decreases monotonically to the ambient value (see, for example Gollner *et al.* (2013) and Rajamanickam *et al.* (2017)).

Figure 4.3(e) shows the stream function, which is related with the horizontal and vertical velocities through (4.30) and (4.31).

Whereas the excess enthalpy variable ξ (figure 4.3(f)) has an imposed value of 1 at

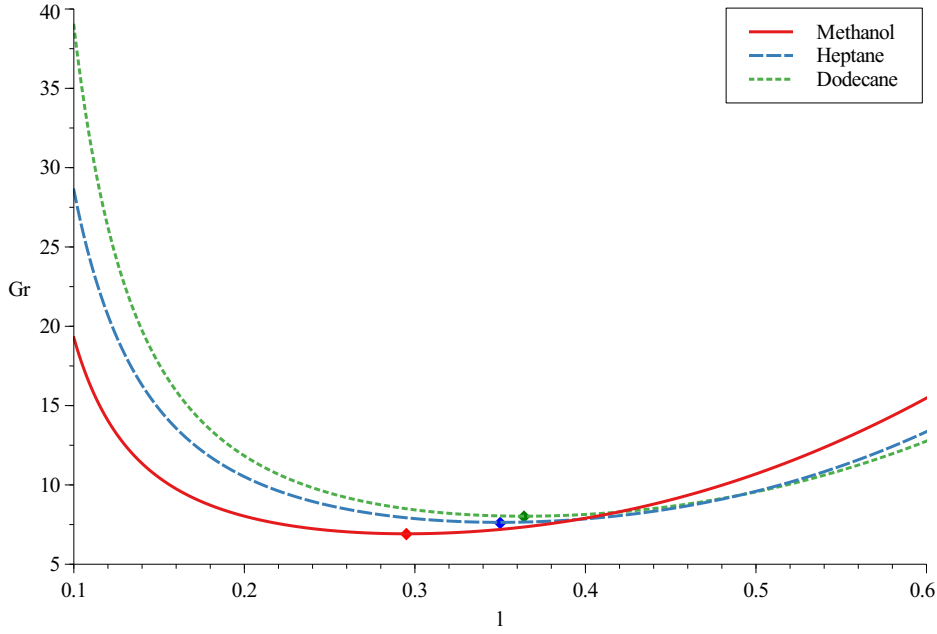

Figure 4.4: Critical Grashof number as a function of the spanwise wave number l for the vortex mode of instability, for methanol (solid red), heptane (long-dashed blue), and dodecane (short-dashed green); big dots indicate the minimum Grashof number over all l.

the fuel surface, corresponding to the temperature being equal to the boiling temperature, the mixture fraction variable Z (figure 4.3(g)) has a value at the flame surface that is computed as part of the solution. This value also determines the mass fraction of fuel at the evaporating fuel surface (4.3(g)), which is seen to be considerably lower for methanol. In agreement with the Burke-Schumann approximation employed in the present work, the mass fraction of fuel is identical to zero above the stoichiometric point η_s.

4.4.2 Local linear stability analysis

We now proceed to the results of a temporal linear stability analysis. We first present the results for the vortex mode of instability, in which the instability takes the form of stationary counterrotating vortex rolls aligned with the stream. This means that the streamwise wavenumber $k = 0$, and the frequency $\omega_r = 0$. As explained in section 4.3.2, in that case the critical Grashof number Gr_c corresponding to $\omega_i = 0$ can directly be obtained by solving the eigenvalue problem written in terms of the eigenvalue $Gr^{1/2}$.

Figure 4.4 represents the critical Grashof number as a function of the spanwise wave number l. The solid red line corresponds to methanol, the long-dashed blue line to heptane, and the short-dashed green line stands for dodecane. The big dots indicate

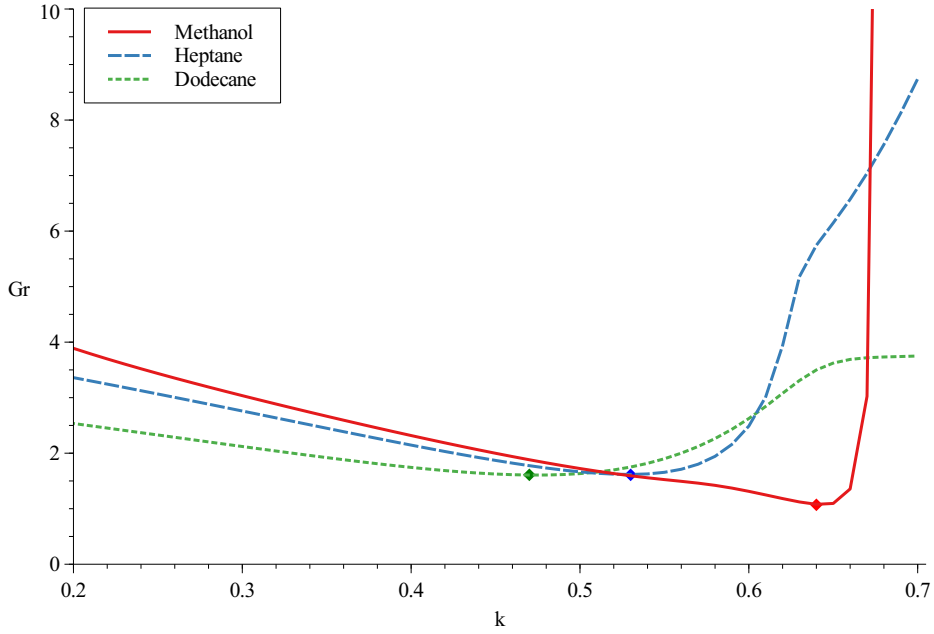

Figure 4.5: Critical Grashof number as a function of the streamwise number k for the wave mode of instability, for for methanol (solid red), heptane (long-dashed blue), and dodecane (short-dashed green); big dots indicate the minimum Grashof number over all k.

the minimum values of Gr_c over all l. These values $Gr_{c,min}$ are summarized in table 4.2. A similar trend is observed for the three fuels. Methanol is seen to be most unstable, with a minimum Grashof number of approximately 7. This is in agreement with methanol having the highest temperatures and the highest streamwise velocity gradients (see figure 4.3). For all fuels, the most unstable spanwise wavenumber lies around $l = 0.3 - 0.35$, as summarized in table 4.3.

For the wave mode of instability, in which disturbances take the form of Tollmien-Schlichting like waves with streamwise wavenumber k and frequency ω_r, a similar analysis yields the results of figure 4.5. Again, the most unstable fuel is seen to be methanol. The minimum values $Gr_{c,min}$ and corresponding wavenumbers k are again summarized in tables 4.2 and 4.3.

	Methanol	Heptane	Dodecane
vortex mode ($l \in \mathbb{R}, k = 0$), $Gr_{c,min}$	6.9	7.6	8
wave mode ($k \in \mathbb{R}, l = 0$), $Gr_{c,min}$	1.1	1.6	1.6

Table 4.2: The minimum critical Grashof number $Gr_{c,min}$ for the vortex and wave mode of instability, for the three fuels under consideration.

The results presented here show critical Grashof numbers that are very low compared

	Methanol	Heptane	Dodecane
vortex mode, spanwise wavenumber l	0.295	0.350	0.364
wave mode, streamwise wavenumber k	0.640	0.530	0.470

Table 4.3: The streamwise and spanwise wavenumber corresponding to the mininum Grashof number $Gr_{c,min}$ of table 4.2 for each of the three fuels under consideration.

to those observed in the literature for the physically similar problems of the natural convection flow over a flat horizontal or inclined plate (Chen & Tzuoo (1982); Rajamanickam *et al.* (2017)). Nevertheless, in those studies the temperature ratio between that of the plate and the ambient is much smaller than the flame-to-ambient temperature ratio of the order of 7 in the present results. In addition, previous studies on inclined plates showed that as the plate inclination is lowered from being vertical towards being horizontal, the dominant instability mode changes from the wave to the vortex mode. Also, experimental observations in wildfires (Miller *et al.* (2017)) show that the vortex modes are the most prevalent in the boundary-layer flow that forms near the edge. This is in disagreement with the present results of table 4.2 that show the wave mode as being the most unstable.

Nevertheless, care should be exerted when interpreting the results of the present local stability analysis, in that the critical Grashof numbers are too low for the boundary-layer approximation used to describe the base flow to be valid. In other words, the streamwise position x for the onset of instability, corresponding to $Gr_{c,min}$, lies too close to the edge for the flow to be sufficiently slender to use the parallel flow approximation. Thus, a more sophisticated analysis is required. In that regard, a fully nonparallel global analysis might be the right tool. In particular, a frequency response analysis, in which the flow is harmonically forced and the flow response in the entire flow domain is analyzed, might be promising. This requires prior calculation of a two-dimensional steady solution of the boundary-layer flow, including the non-slender Navier-Stokes region near the edge of the fuel surface.

4.5 Conclusions and further work

In this chapter, we have studied the self-similar buoyancy-driven boundary-layer flow that forms when a horizontal fuel surface is burned in a quiescent ambient. This flow was studied by Clarke & Riley (1976) under the assumption of a unity Lewis number. This work generalizes their approach to the case of non-unity Lewis numbers, which is especially relevant for the burning of heavy hydrocarbon fuels. In addition, our description incorporates a detailed evaporation model with which the amount of fuel that is evaporated and burned is obtained as part of the solution. Results have been presented for three sample fuels: methanol, heptane, and dodecane.

Heat loss due to radiation is not taken into account in the description, but might have a considerable effect for strongly sooting flames such as heptane and dodecane. Radiation can be anticipated to have a stabilizing effect on the flame, since it will lower the peak temperatures, and hence the temperature gradients in the flow.

The temporal linear stability analysis presented here is a first step in analyzing the prevalence and amplification of disturbances in this flow. Unlike similar configurations such as the natural convection flow over an horizontal or inclined heated plate, the stability of the Clarke-Riley diffusion flame has not been studied before in the literature. Two types of disturbances have been considered: stationary counter-rotating vortical structures aligned with the stream—called the vortex mode—and Tollmien-Schlichting wave-like structures—called the wave mode. For both modes, we obtained critical Grashof numbers on the order of 5-10. Unfortunately, this result invalidates the boundary-layer approximation that was employed to describe the basic flow. This means the Clarke-Riley boundary-layer flow is so unstable that disturbances can be expected to grow very close to the edge of the fuel surface, where the flow is not sufficiently slender to employ a strictly parallel local stability analysis in combination with a self-similar boundary-layer description. This creates the need for a different approach, that takes into account the fully two-dimensional character of the flow. In that regard, a frequency response analysis, like that provided in chapter 3 of this dissertation, is a promising option.

References

CHEN, T. S. & TZUOO, K. L. 1982 Vortex Instability of Free Convection Flow Over Horizontal and Inclined Surfaces. *J. Heat Transfer-ASME* **104**, 637–643.

CLARKE, J. F. & RILEY, N. 1976 Free convection and the burning of a horizontal fuel surface. *Journal of Fluid Mechanics* **74** (3), 415–431.

FINNEY, MARK A., COHEN, JACK D., FORTHOFER, JASON M., MCALLISTER, SARA S., GOLLNER, MICHAEL J., GORHAM, DANIEL J., SAITO, KOZO, AKAFUAH, NELSON K., ADAM, BRITTANY A. & ENGLISH, JUSTIN D. 2015 Role of buoyant flame dynamics in wildfire spread. *Proceedings of the National Academy of Sciences* **112** (32), 9833–9838.

GOLLNER, MICHAEL J., SÁNCHEZ, ANTONIO L. & WILLIAMS, FORMAN A. 2013 On the heat transferred to the air surrounding a semi-infinite inclined hot plate. *Journal of Fluid Mechanics* **732**, 304–315.

GORTLER, HENRY 1954 On the three-dimensional instability of laminar boundary layers on concave walls .

HAALAND, S.E. & SPARROW, E.M. 1973*a* Vortex instability of natural convection flow on inclined surfaces. *International Journal of Heat and Mass Transfer* **16** (12), 2355 – 2367.

HAALAND, S. E. & SPARROW, E. M. 1973*b* Wave instability of natural convection on inclined surfaces accounting for nonparallelism of the basic flow. *Journal of Heat Transfer* **95**.

HWANG, G J & CHENG, K C 1973 Thermal instability of laminar natural convection flow on inclined isothermal plates. *The Canadian Journal of Chemical Engineering* **51** (6), 659–666.

IYER, P. A. & KELLY, R. E. 1974 The stability of the laminar free convection flow induced by a heated inclined plate. *International Journal of Heat and Mass Transfer* **17** (4), 517–525.

JONES, D R 1973 Free convection from a semi-infinite flat plate inclined at a small angle to the horizontal. *The Quarterly Journal of Mechanics and Applied Mathematics* **26** (1), 77–98.

KAHAWITA, RENÉ A. & MERONEY, ROBERT N. 1974 The vortex mode of instability in natural convection flow along inclined plates. *International Journal of Heat and Mass Transfer* **17** (5), 541–548.

KHORRAMI, MEHDI R, MALIK, MUJEEB R & ASH, ROBERT L 1989 Application of spectral collocation techniques to the stability of swirling flows. *Journal of Computational Physics* **81**.

LIÑÁN, A., MARTÍNEZ-RUIZ, D., VERA, M. & SÁNCHEZ, A. L. 2017 The large-activation-energy analysis of extinction of counterflow diffusion flames with non-unity lewis numbers of the fuel. *CF* **175**, 91–106.

LIDE, DAVID R 2001 Crc handbook of physics and chemistry. *CRC Press, Boca Raton, USA* **76**, 1995–1996.

LIÑÁN, AMABLE, VERA, MARCOS & SÁNCHEZ, ANTONIO L. 2015 Ignition, Liftoff, and Extinction of Gaseous Diffusion Flames. *Annual Review of Fluid Mechanics* **47** (1), 293–314.

LLOYD, JR & SPARROW, EM 1970 On the instability of natural convection flow on inclined plates. *Journal of Fluid Mechanics* **42** (3), 465–470.

MILLER, COLIN H., TANG, WEI, FINNEY, MARK A., MCALLISTER, SARA S., FORTHOFER, JASON M. & GOLLNER, MICHAEL J. 2017 An investigation of coherent structures in laminar boundary layer flames. *Combustion and Flame* **181**, 123–135.

MORENO-BOZA, DANIEL, COENEN, WILFRIED, CARPIO, JAIME, SÁNCHEZ, ANTONIO L. & WILLIAMS, FORMAN A. 2018 On the critical conditions for pool-fire puffing. *Combustion and Flame* **192**, 426 – 438.

PERA, LUCIANO & GEBHART, BENJAMIN 1973*a* Natural convection boundary layer flow over horizontal and slightly inclined surfaces. *International Journal of Heat and Mass Transfer* **16** (6), 1131–1146.

PERA, LUCIANO & GEBHART, BENJAMIN 1973*b* On the stability of natural convection boundary layer flow over horizontal and slightly inclined surfaces. *International Journal of Heat and Mass Transfer* **16** (6), 1147–1163.

RAJAMANICKAM, PRABAKARAN, COENEN, WILFRIED & SÁNCHEZ, ANTONIO L. 2017 Non-Boussinesq stability analysis of natural-convection gaseous flow on inclined hot plates. *International Journal of Heat and Mass Transfer* **109**, 949–957.

ROTEM, ZEEV & CLAASSEN, LUTZ 1969 Natural convection above unconfined horizontal surfaces. *Journal of Fluid Mechanics* **39** (1), 173–192.

SÁNCHEZ, ANTONIO L, LIÑÁN, AMABLE & WILLIAMS, FORMAN A 1997 A generalized burke-schumann formulation for hydrogen-oxygen diffusion flames maintaining partial equilibrium of the shuffle reactions. *Combustion science and technology* **123** (1-6), 317–345.

SCHMIDT, ERNST & BECKMANN, WILHELM 1930 Das temperatur-und geschwindigkeitsfeld vor einer wärme abgebenden senkrechten platte bei natürlicher konvektion. *Technische Mechanik und Thermodynamik* **1** (11), 391–406.

SCHUBAUER, GB 1947 Laminar boundary-layer oscillations and stability of laminar flow. *Journal of the Aeronautical Sciences* **14** (2), 69–78.

SPARROW, EM & HUSAR, RB 1969 Longitudinal vortices in natural convection flow on inclined plates. *Journal of Fluid Mechanics* **37** (2), 251–255.

TREFETHEN, LLOYD N 2013 *Approximation theory and approximation practice*, , vol. 128. Siam.

ZELDOVICH, YA B 1951 On the theory of combustion of initially unmixed gases. *NASA* .

Conclusions and future work

Conclusions

The results of chapter 2 represent the first attempt to capture the transition between globally stable and globally unstable submerged axisymmetric laminar low-density jets by direct numerical simulations under a realistic geometric setting. The study includes different momentum thicknesses of the outlet velocity profiles, from the fully-developed parabolic one to top-hat like shapes associated with short tubes attached to injection nozzles.

The numerical simulations successfully reproduce the Hopf bifurcation described by Hallberg & Strykowski (2006) and Lesshafft *et al.* (2006) and represented in figure 2.10 for the range of momentum thicknesses covered by linear theory (Coenen *et al.*, 2017) and experiments (Hallberg & Strykowski, 2006). Moreover, close to criticality, the numerical oscillation amplitudes fit the supercritical Stuart-Landau model. In the globally stable regimes, the initial perturbations vanish at large times, and the jet recovers the basic axisymmetric steady state. In contrast, globally unstable regimes lead to a self-sustained oscillatory state with a well-marked characteristic frequency that is intrinsic to the flow. The critical conditions for the onset of global instability lie between the experimentally observed values, and those predicted by the global linear stability analysis. This fact supports the hypothesis that low-level noise in experiments and numerical simulations may prematurely trigger a transition to a globally unstable behavior.

The spatial distribution of the normalized density oscillation amplitude shown in figure 2.9 is consistent with the results of Lesshafft *et al.* (2006) for synthetic jets, reaching a maximum at $x \sim 5$, with decreasing amplitude as the Reynolds number decreases.

With respect to the critical Reynolds number studied in chapter 3, the first helical mode, $m = \pm 1$, has been found to be the most unstable mode in all the configurations studied. The axisymmetric mode, $m = 0$, and the second helical one, $m = \pm 2$, are always subdominant. The maximum gains of mode $m = \pm 1$ take place at very small values of the Strouhal number, associated with long characteristic length scales in their response. This behavior sets a lower limit for the Strouhal number that can be converged with given computational resources that, in our case, corresponded to $St = 0.03$.

Low-density jets have a similar response behavior under optimal and uniform forcing conditions, but optimal forcing provides about two orders of magnitude larger gains than uniform forcing. The mode $m = \pm 1$ is the most unstable one, followed by either $m = 0$

at moderate to high Strouhal numbers, or $m = \pm 2$ at low Strouhal numbers. Top-hat like outlet velocity profiles with $D/\theta_0 = 35$ have larger gains for $m = 0$ than parabolic ones.

The critical Reynolds number of low-density jets under optimal forcing is $Re \approx 8$ for $m = \pm 1$ and $Re \approx 15$ for $m = 0$ and $m = \pm 2$ for both types of outlet velocity profiles. In contrast, under uniform forcing conditions the critical Reynolds numbers with parabolic outlet profile is $Re = 54$ for $m = \pm 1$, $Re \approx 200$ for $m = \pm 2$, and $Re \approx 450$ for $m = 0$. For top-hat like velocity profiles, it has been found that $Re = 59$ for $m = \pm 1$, $Re \approx 150$ for $m = 0$, and $Re \approx 200$ for $m = \pm 2$.

In the case of constant-density jets, the gains for optimal forcing are larger than those for uniform forcing by several orders of magnitude, and the most unstable mode is also $m = \pm 1$. The modes $m = \pm 1$ and $m = \pm 2$ have monotonically decreasing gains as a function of the Strouhal number. However, the axisymmetric mode, $m = 0$, presents a maximum at $St \approx 0.5$. As in the case of low-density jets, modes $m = 0$ and $m = \pm 2$ have slightly larger gains for a top-hat like outlet velocity profile than with the parabolic one.

The critical Reynolds number using optimal gain has similar values as light jet $Re \approx 8$ for $m = \pm 1$ and $Re \approx 15$ for $m = 0$ and $m = \pm 2$. On the other hand, using uniform forcing with parabolic profiles, the helical mode $m = \pm 1$ has the critical Reynolds number $Re = 85$ while the mode $m = \pm 2$ have this critical value $Re \approx 450$ and axisymmetric mode $m = 0$ was not found any. Top hat kind velocity profiles found for mode $m = \pm 1$ a slightly high critical Reynolds number $Re = 97$ but modes $m = 0$ and $m = \pm 2$ have their critical Reynolds number at $Re \approx 450$ both. These results of critical Reynolds number for uniform forcing are found consistent with ones reported by Reynolds (1962) and Danaila *et al.* (1997) for their Reynolds number, although ones from Viilu (1962) must be aware he does not show the response and we can not conclude which mode is closer.

For a fixed value of $St = 0.3$, the spatial structure of the response for parabolic outlet profiles presents local maximum at distances of 5, 10 and 20 and is mainly contained within 20, 30 and 50 radii for $m = \pm 2$, $m = 0$ and $m = \pm 1$, respectively. For top-hat like outlet profiles, the results are similar, except that the mode $m = \pm 1$ has its maximum response closer to the injector. This behavior is reproduce by mixed and constant density jets of appendix C increasing the distance from the inject as the density ratio is increased.

When the jet geometry is analyzed, taking into account an injector tube far from walls and a circular orifice on a wall, it has been shown that low-density jets under optimal forcing conditions present substantial difference in gain, while for constant-density jets the results are similar. In the case of uniform forcing, the gains for the injector configuration are one order of magnitude larger than those associated with the orifice geometry for all the density ratios studied.

Analyzing the forcing region, it has been found that the results are independent of the injector pipe length, $x_p \gtrsim 16$. Also, extending the forcing region outside the pipe, results show an increasing in the gains for optimal and uniform forcing.

In chapter 4, the self-similar buoyancy-driven boundary-layer flow that forms when

a horizontal fuel surface is burned in a quiescent ambient has been analyzed. This flow was studied by Clarke & Riley (1976) under the assumption of a unity Lewis number. The present work generalizes their approach to the case of non-unity Lewis numbers, which is especially relevant for the burning of heavy hydrocarbon fuels. In addition, a detailed description of the evaporation model is given with the amount of fuel that is evaporated and burned obtained as part of the solution. The heat loss due to radiation has not been taken into account, although it may have a stabilizing effect on the flame by reducing the maximum temperature achieved. Results have been presented for three sample fuels: methanol, heptane, and dodecane.

The temporal linear stability analysis presented here represents a first step towards the study of the amplification of disturbances in this flow, which had not been studied in the previous literature. Two kinds of disturbances may appear: stationary counter-rotating vortical structures aligned with the stream—called the vortex mode—and Tollmien-Schlichting wave-like structures—called the wave mode. Both modes present a critical Grashof number on the order of unity to tens, a result that invalidates the boundary-layer approximation employed to describe the base flow. Indeed, it means that the flow is so unstable that disturbances appear very close to the edge, and is not slender enough to apply a strictly parallel local stability analysis in combination with a self-similar boundary-layer description.

Future work

In the case of submerged laminar jets, the hypothesis that low-level noise triggers a premature transition to a globally unstable state in experiments and numerical simulations needs further support. To that end, numerical simulations imposing a harmonic forcing at the inlet could well provide the necessary clues. Moreover, changing the amplitude and frequency of the forcing, the numerical response of the jet could also be compared with the results of chapter 3. However, the numerical method used in the present work is computationally expensive, and should be improved to reduce the simulation cost. In addition, since the dominant modes are non-axisymmetric, three-dimensional numerical simulations would be required to compare with the results of chapter 3. Moreover, using the numerical results of globally unstable regimes, a mean flow can easily be computed, and its use in the global linear analysis could be interesting to check the hypothesis of neutrality (Barkley, 2006) in a new flow configuration.

Future work suggested by chapter 3 would involve a more detailed study of the influence of the density ratio and of the momentum thickness parameter on the critical Reynolds number. Also, the use of a more realistic model of the actual disturbances that may appear in practical applications would be desirable. For instance, it could be interesting to impose disturbances as inflow boundary conditions, leading to a substantial change in the results.

Finally, concerning chapter 4, as a result of the small values of the critical Grashof number that make a parallel analysis questionable, a new global approach is clearly needed. In particular, it should take into account the fully two-dimensional flow, and a frequency response analysis similar to that used in chapter 3 for submerged jets.

Acknowledgments

This doctoral dissertation has been supported by a 4-year PIF contract of the Pre-doctoral Researcher Training Program of *Universidad Carlos III de Madrid* and under projects DPI2014-59292-C3-1-P and DPI2015-71901-REDT awarded by the Spanish Ministry of Economy and Competitiveness. The results presented in Chapter 4 were obtained at the *University of California San Diego* during a a six-month research period there. The author wishes to express his most sincere gratitude to Prof. Dr. Antonio L. Sánchez.

References

BARKLEY, D 2006 Linear analysis of the cylinder wake mean flow. *EPL (Europhysics Letters)* **75** (5), 750.

CLARKE, J. F. & RILEY, N. 1976 Free convection and the burning of a horizontal fuel surface. *Journal of Fluid Mechanics* **74** (3), 415–431.

COENEN, W., LESSHAFFT, L., GARNAUD, X. & SEVILLA, A. 2017 Global instability of low-density jets. *J. Fluid Mech.* **820**, 187:207.

DANAILA, IONUT, DUŠEK, JAN & ANSELMET, FABIEN 1997 Coherent structures in a round, spatially evolving, unforced, homogeneous jet at low Reynolds numbers. *Physics of Fluids* **9** (11), 3323–3342.

HALLBERG, M. P. & STRYKOWSKI, P. J. 2006 On the universality of global modes in low-density axisymmetric jets. *J. Fluid Mech.* **569**, 493–507.

LESSHAFFT, L., HUERRE, P., SAGAUT, P. & TERRACOL, M. 2006 Nonlinear global modes in hot jets. *J. Fluid Mech.* **554**, 393–409.

REYNOLDS, A J 1962 Observations of a liquid-into-liquid jet. *Journal of Fluid Mechanics* **14** (4), 552–556.

VIILU, ANDRUS 1962 An Experimental Determination of the Minimum Reynolds Number for Instability in a Free Jet. *J. Appl. Mech.* **29** (5), 506–508.

APPENDIX

A

The boundary layer formulation used to obtain the outlet velocity profile

This appendix is dedicated to explain the velocity profile calculation that has been used in chapters 2 and 3. This procedure is identical to one done by Coenen (2010).

Let us consider the axisymmetric laminar flow with a constant flow rate Q^* through an injector pipe of radius R^* and length L^*_{pipe} that discharges into an infinite media, showed in figure 2.1. A cylindrical coordinate is used (x^*, r^*) with velocity $\boldsymbol{u}^* = (u^*, v^*)$. The jet has density ρ^*_j and viscosity μ^*_j, while the ambient has density ρ^*_∞ and viscosity μ^*_∞. Density ratio is defined as $S = \rho^*_j/\rho^*_\infty$. Buoyancy effects can be neglected due to small Richardson number $Ri = \left(\rho_\infty - \rho_j\right) gR/\left(\rho_j U_j^2\right) \ll 1$. Considering fluid properties from Lide (2001) viscosity values differ by 10%, then, viscosity variations are not considered and $\mu^*_j = \mu^*_\infty$.

We assume the Reynolds number is large, $Re = \rho^*_j U^*_m R^*/\mu^*_j \gg 1$, so the characteristic length of the steady state solution is also large, $ReR \gg 1$, but below the critical value to consider it as laminar flow.

On the inlet, flow starts on the pipe with uniform velocity profile with constant value $U^*_m = 4Q^*/(\pi R^{*2})$, and discharges at pipe exit with a profile $u^*_0(r)$ having the same mean velocity U^*_m. Velocity profile shape varies with the length L^*_{pipe} of the pipe. For small values of L^*_{pipe}, the exit profile is Blasius-like, also known as top-hat-like, while long pipes, a smooth Hagen-Poiseuille profile appears.

The shape of the velocity profiles is measured by the momentum thickness, defined as $\theta^*_0 = \int_0^\infty \frac{u^*_0(r)}{u^*_0(0)}\left[1 - \frac{u^*_0(r)}{u^*_0(0)}\right] \mathrm{d}r^*$, or more specifically with the inverse of the dimensionless momentum thickness $D/\theta_0 = 2R^*/\theta^*_0$ of the jet at the exit based here on the diameter instead of the radius for consistency with the literature. Blasius-like profiles correspond to high values of D/θ_0, while the parabolic Hagen-Poiseuille profile has the limiting value $D/\theta_0 = 15$. This differences in the profiles can be seen in figure A.1 where a comparison of parabolic profile, high ratio $D/\theta_0 = 35$ and uniform velocity are showed.

The velocity profile at the exit $u^*_0(r)$ depends on the axisymmetric laminar flow along the tube. Density will be considered constant along the pipe as well as the temperature,

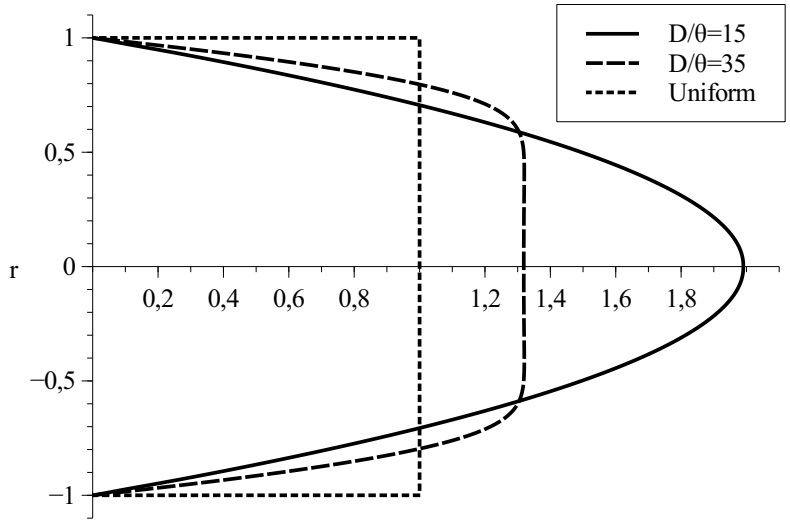

Figure A.1: Velocity profiles, uniform, top-hat-like ($D/\theta = 35$) and parabolic ($D/\theta = 15$).

see Nichols *et al.* (2007); Williams (1985), due to the low Mach number $Ma = U_m^*/c^*$ with c^* is the speed of the sound in the gas. This approximations consider that jet density variations only take into account changes in the molecular weight and not the pressure and can be consider isothermal jet.

With this assumptions, boundary layer approximation can be applied to solve the flow inside the pipe integrating the continuity and momentum equations

$$\frac{\partial}{\partial x}(ru) + \frac{\partial}{\partial r}(rv) = 0, \tag{A.1}$$

$$u\frac{\partial u}{\partial x} + v\frac{\partial u}{\partial r}(rv) = -P + \frac{1}{r}\frac{\partial}{\partial r}\left(r\frac{\partial u}{\partial r}\right), \tag{A.2}$$

with initial condition $u = 1$ at the origin and boundary conditions $\partial u/\partial r = v = 0$ at $r = 0$ and $u = v = 0$ on the pipe wall. P is the rescaled pressure gradient which is an unknown for the calculation. To integrate the problem numerically, the method of lines is followed as Holmes (2007) explained. A second order centered scheme discretization has been done in radial direction r and a system of ordinary differential equations has been written a long the axial direction x, integrated with a fourth order Runge-Kutta algorithm.

As Coenen *et al.* (2008) showed, based on Crabtree *et al.* (1963), short injectors with a $x_p = L^*_{\text{pipe}}/R \ll 1$ have nearly uniform velocity except on close to the walls, where a boundary layer is created of a characteristic length of $L^{1/2}_{\text{pipe}}R$. It is valid not only for straight pipes but also for nozzles.

In case of longer injector $L_{\text{pipe}} \approx 1$ the velocity profile approaches the parabolic Poiseuille profile that will be a $L_{\text{pipe}} \gg 1$. Parabolic profile follows the equation $u(r) = 2\left(1-r^2\right)$. Figure A.2 represents the variations of the momentum thickness along pipe length. This data was taken from Coenen (2010) and adapted to our variables. Notice the asymptotic behaviors at low and high Re/L_{pipe} corresponding to $D/\theta = 15$ and $D/\theta_0 = \left(1.328\left(Re/L_{\text{pipe}}\right)^{1/2}\right)^{-1}$

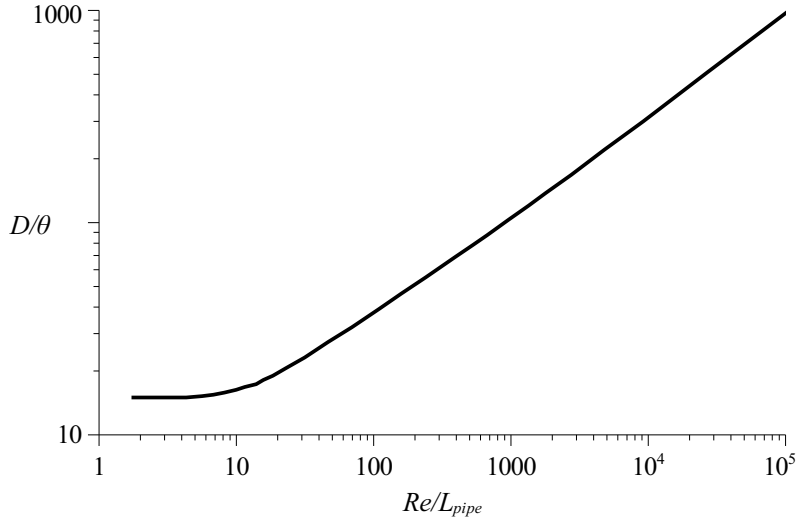

Figure A.2: Variation of D/θ_0 with Re/L_{pipe}. Data extracted from Coenen (2010).

References

COENEN, W. 2010 Absolute instability in the near field of low-density jets. *Universidad Carlos III de Madrid* .

COENEN, W., SEVILLA, A. & SÁNCHEZ, A. 2008 Absolute instability of light jets emerging from circular injector tubes. *Phys. Fluids* **20**, 074104.

CRABTREE, LF, KUCHEMANN, D & SOWERBY, L 1963 Three-dimensional boundary layers. *Laminar Boundary Layers* pp. 430–432.

HOLMES, M. H. 2007 *Introduction to Numerical Methods in Differential Equations*. Springer, New York.

LIDE, DAVID R 2001 Crc handbook of physics and chemistry. *CRC Press, Boca Raton, USA* **76**, 1995–1996.

NICHOLS, J. W., SCHMID, P. J. & RILEY, J. J. 2007 Self-sustained oscillations in variable-density round jets. *J. Fluid Mech.* **582**, 341–376.

WILLIAMS, F. A. 1985 Comment. *Combustion Science and Technology* **43** (5-6), 329–332.

APPENDIX

B

Global frequency response and critical Reynolds number for $S = 0.5$

This appendix is devoted to show the optimal and uniform gain for a mixed jet with density ratio $S = 0.5$ and Reynolds number $Re = 200$, in the same way than ones analyzed on chapter 3 for helium-nitrogen jets ($S = 0.14$) and constant density ($S = 1$). As has been seen in chapter 3 the minimum value converged for frequency is $St = 0.03$.

Figures B.1 and B.2 show the optimal (left panels) and uniform (right panels) for a parabolic outlet profile with $D/\theta_0 = 15$ in figure B.1, and for a top-hat profile with $D/\theta_0 = 35$ in figure B.2.

In figure B.1, it can be seen that the first helical mode $m = \pm 1$ (blue dashed line) has the maximum gain by 4 orders of magnitude compared with the maximum gain of the other two modes, both for optimal and uniform forcing. It is also deduced that the optimal gain is approximately 2 orders of magnitude larger than the uniform forcing. The axisymmetric mode (red solid line) presents a maximum at $St \approx 0.45$ only in optimal forcing, while non-axisymmetric modes have their maximum gains at smaller Strouhal numbers. Another interesting observation is that, for $m = 0$ and $m = \pm 2$ (green dotted lines), the jet is unstable under optimal forcing conditions, but stable for the uniform forcing, since the gain is smaller than one for all frequencies in the latter case.

The results of figure B.2 reveal that the gains of mode $m = \pm 1$ for top-hat-like outlet velocity profiles, $D/\theta_0 = 35$, are slightly smaller than those associated with the parabolic profile. In contrast, modes $m = 0$ and $m = \pm 2$ have much larger gains in the case of the top-hat profile for optimal forcing (figure B.2a), and slightly larger in the case of uniform forcing (figure B.2b). The axisymmetric mode, $m = 0$, presents a maximum at $St \approx 0.45$. Moreover, for $St > 0.6$ and optimal forcing, the modes $m = 0$ and $m = \pm 1$ have approximately the same gain, but for uniform forcing, are $m = 0$ and $m = \pm 2$.

As have been seen in figures B.1 and B.2, the modes $m = 0$ and $m = \pm 2$ have larger maximum gains for top-hat like profiles than for the parabolic profile, while the reverse is true for the helical $m = \pm 1$ mode, independently of the type of forcing.

In figure B.3 the maximum of the gain for each mode is represented at several Reynolds

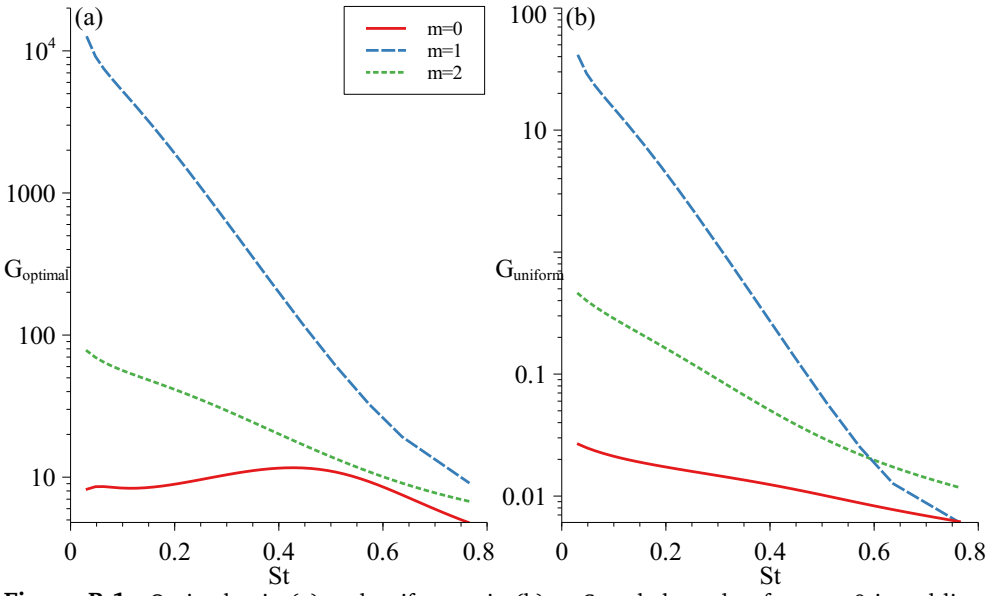

Figure B.1: Optimal gain (a) and uniform gain (b) vs Strouhal number for $m = 0$ in red line, $m = \pm 1$ in blue dashed line and $m = \pm 2$ in green dotted line at $D/\theta_0 = 15$, $Re = 200$ and $S = 0.5$

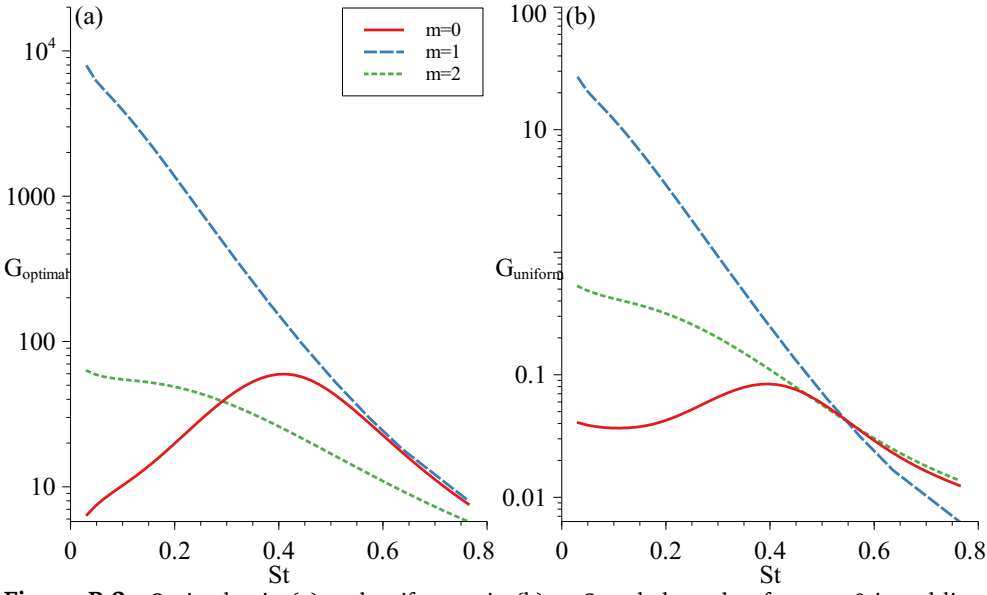

Figure B.2: Optimal gain (a) and uniform gain (b) vs Strouhal number for $m = 0$ in red line, $m = \pm 1$ in blue dashed line and $m = \pm 2$ in green dotted line at $D/\theta_0 = 35$, $Re = 200$ and $S = 0.5$

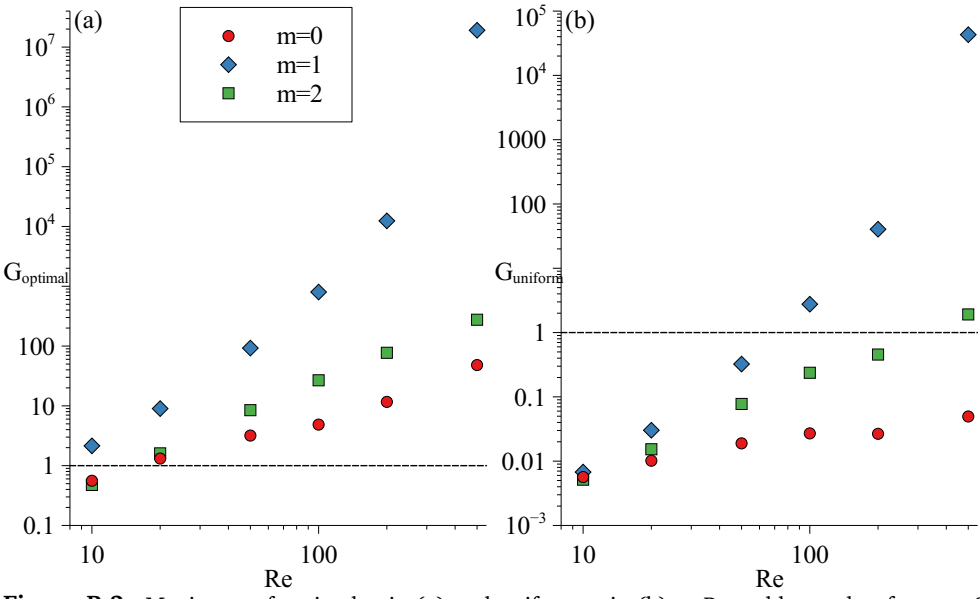

Figure B.3: Maximum of optimal gain (a) and uniform gain (b) vs Reynolds number for $m = 0$ on red dots, $m = \pm 1$ on blue diamonds and $m = \pm 2$ on green squares at $D/\theta_0 = 15$ and $S = 0.5$

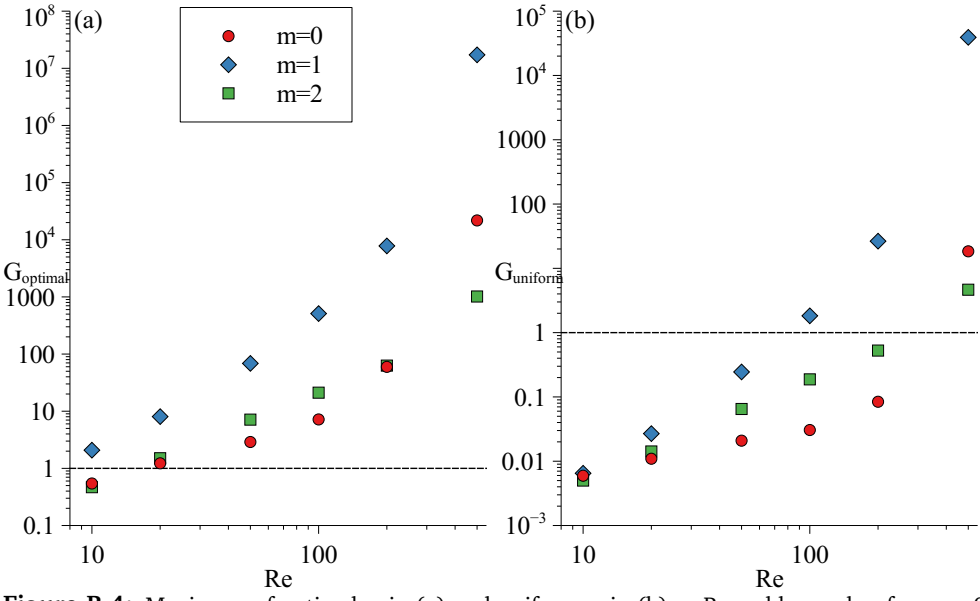

Figure B.4: Maximum of optimal gain (a) and uniform gain (b) vs Reynolds number for $m = 0$ on red dots, $m = \pm 1$ on blue diamonds and $m = \pm 2$ on green squares at $D/\theta_0 = 35$ and $S = 0.5$

numbers for parabolic profiles and density ratio, $S = 0.5$. The helical mode $m = \pm 1$ (blue diamonds) has larger gains than modes $m = 0$ (red dots) and $m = \pm 2$ (green squares), both for optimal (left panel) and uniform (right panel) types of forcing.

For the first helical mode, $m = \pm 1$, the transition from stable to unstable flow, associated with gains smaller and larger than one, respectively, takes place for a Reynolds number $Re \approx 8$ in the case of optimal forcing, and $Re \approx 70$ for uniform forcing. On the other hand, modes $m = 0$ and $m = \pm 2$ have the transition for optimal forcing at $Re \approx 15$ being the gain for $m = \pm 2$ slightly larger than that for $m = 0$ at low and moderate Reynolds numbers, while the opposite behavior is observer at high Reynolds numbers. A similar scenario takes place in the case of uniform forcing, but with larger values of the critical Reynolds number, namely $Re \approx 300$ for $m = \pm 2$, and for $m = 0$ it does not cross the limit of unity gain inside the analyzed range.

Figure B.4 shows the maximum gains for the same modes shown in figure B.3, but considering top-hat like profiles for optimal forcing (left panel) and uniform forcing (right panel). The results are similar to those of figure B.3. The dominant mode is always $m = \pm 1$, followed by the $m = \pm 2$ mode at low and moderate Reynolds numbers, and by $m = 0$ at high Reynolds numbers.

It is interesting to note that the critical Reynolds numbers computed with optimal forcing and top-hat-like profiles are similar to those associated with parabolic profiles, namely $Re \approx 8$ for $m = \pm 1$ and $Re \approx 15$ for $m = 0$ and $m = \pm 2$. For uniform forcing, the critical Reynolds numbers are $Re \approx 80$ for $m = \pm 1$, slightly larger than that associated with the parabolic outlet profile, and $Re \approx 300$ for $m = \pm 2$. The main difference between both kinds of outlet profiles is associated with the axisymmetric mode, $m = 0$, which has an associated critical Reynolds number $Re \approx 300$ for a top-hat-like outlet profile.

Summarizing the results of figures B.1 – B.4, it can be concluded that, for both types of forcing, top-hat-like profiles have smaller critical Reynolds numbers for modes $m = 0$ and $m = \pm 2$, and slightly larger critical Reynolds numbers for the first helical mode $m = \pm 1$.

APPENDIX

C

Spatial structures of the frequency response analysis for $S = 0.5$ and $S = 1$

This appendix is devoted to present and discuss the spatial structure of the optimal disturbances and the corresponding responses. Since the uniform forcing presents similar spatial structures as the optimal ones, only the latter will be presented to reader. The cases presented here are (density ratio $S = 0.5$ and $S = 1$) completed ones analyzed on chapter 3 ($S = 0.14$).

All the figures shown in this appendix share a common design as those on chapter 3: the optimal forcing and the corresponding response are shown in panels (a) and (b), respectively, with the isocontours of the axial velocity amplitude. Finally, the axial velocity amplitude is represented along the line $r = 0.5$ in panel (c). Notice that only a small part of the spatial domain is shown to aid visualizing panels (a) and (b), and that the colorbar scales in panels (a) and (b) are different. To compare the responses of the three leading azimuthal modes, fixed values of the Strouhal number, $St = 0.3$, and of the Reynolds number, $Re = 200$, were chosen in all cases.

C.1 Results for $S = 0.5$

Figure C.1 displays the forcing and response structures of a jet with Poiseuille outlet velocity profile, $D/\theta_0 = 15$, for the axisymmetric mode, $m = 0$. It is deduced that the response is contained within a distance of about 40 injector radii, presenting a maximum at an axial position of approximately 10.

On the other hand, figure C.2 which corresponds to the case for helical mode $m = \pm 1$ shows the optimal response contained within about 50 radii downstream from the injector outlet with a maximum in axial distance at 25 radii. Considering the axisymmetric case, the helical present almost doubled for same Reynolds and Strouhal numbers than mode $m = 0$.

However, figure C.3 presents the case for mode $m = \pm 2$ whose optimal response is contained within 20 radii and the maximum is found at approximately 5. It is then, closer

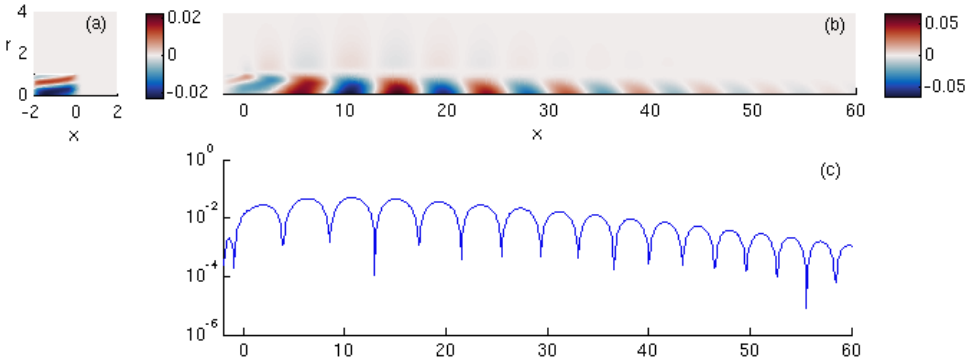

Figure C.1: (a) Contours of optimal forcing, (b) contours of optimal response and (c) optimal response profile at $r = 0.5$, for the axisymmetric mode, $m = 0$, and a jet with $S = 0.5$, $D/\theta_0 = 15$, $Re = 200$ and $St = 0.3$. The three panels show the amplitude of the axial velocity.

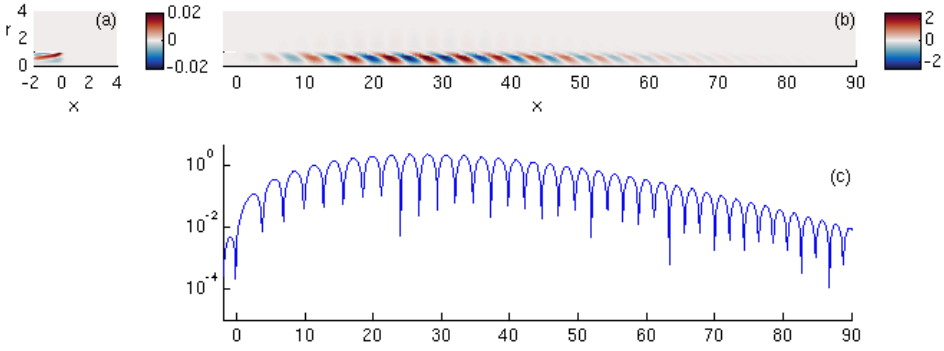

Figure C.2: (a) Contours of optimal forcing, (b) contours of optimal response and (c) optimal response profile at $r = 0.5$, for the axisymmetric mode, $m = \pm 1$, and a jet with $S = 0.5$, $D/\theta_0 = 15$, $Re = 200$ and $St = 0.3$. The three panels show the amplitude of the axial velocity.

to injector than previous modes $m = 0$ and $m = \pm 1$.

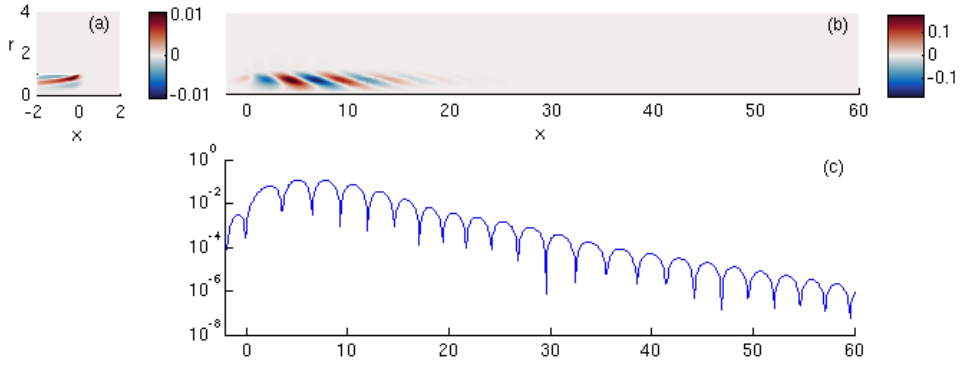

Figure C.3: (a) Contours of optimal forcing, (b) contours of optimal response and (c) optimal response profile at $r = 0.5$, for the axisymmetric mode, $m = \pm 2$, and a jet with $S = 0.5$, $D/\theta_0 = 15$, $Re = 200$ and $St = 0.3$. The three panels show the amplitude of the axial velocity.

Figure C.4 which represents the forcing and response structures of a jet with top-hat outlet velocity profile, $D/\theta_0 = 35$, for the axisymmetric mode. It is deduced that the response is contained within a distance of about 40 injector radii, presenting a maximum at an axial position of approximately 15.

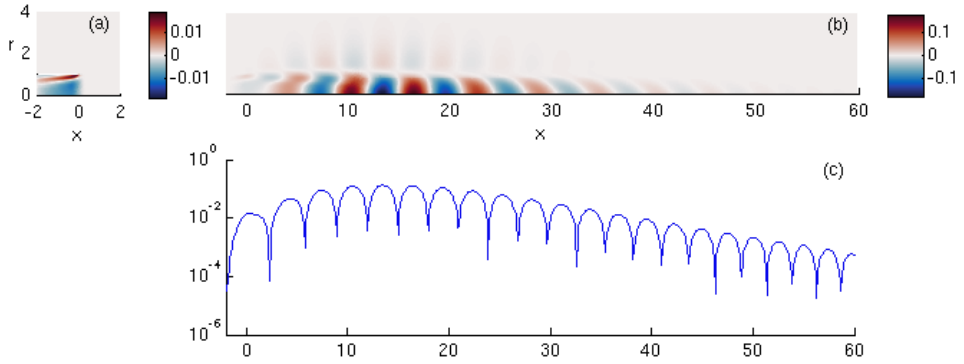

Figure C.4: (a) Contours of optimal forcing, (b) contours of optimal response and (c) optimal response profile at $r = 0.5$, for the axisymmetric mode, $m = 0$, and a jet with $S = 0.5$, $D/\theta_0 = 35$, $Re = 200$ and $St = 0.3$. The three panels show the amplitude of the axial velocity.

On contrary, figure C.5 corresponds to the case for helical mode $m = \pm 1$ shows the optimal response contained within about 60 radii downstream from the injector outlet with a maximum in axial distance at 20 radii.

Finally, figure C.6 presents the case for mode $m = \pm 2$ whose optimal response is contained within 30 radii and the maximum is found at approximately 10.

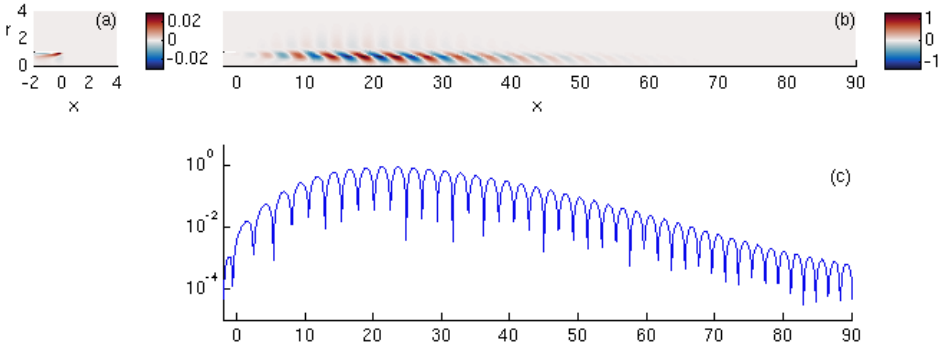

Figure C.5: (a) Contours of optimal forcing, (b) contours of optimal response and (c) optimal response profile at $r = 0.5$, for the axisymmetric mode, $m = \pm 1$, and a jet with $S = 0.5$, $D/\theta_0 = 35$, $Re = 200$ and $St = 0.3$. The three panels show the amplitude of the axial velocity.

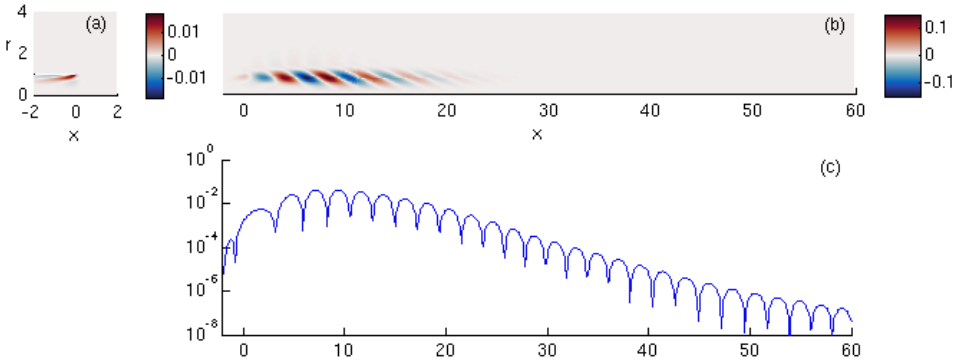

Figure C.6: (a) Contours of optimal forcing, (b) contours of optimal response and (c) optimal response profile at $r = 0.5$, for the axisymmetric mode, $m = \pm 2$, and a jet with $S = 0.5$, $D/\theta_0 = 35$, $Re = 200$ and $St = 0.3$. The three panels show the amplitude of the axial velocity.

As has been seen in Poiseuille profiles, for top-hat ones, the mode $m = \pm 2$ response is found closer to injector and the mode $m = \pm 1$ the farthest. However, top-hat kind $D/\theta_0 = 35$ with modes $m = 0$ and $m = 1$ are contained, and find the maximum closer to the nozzle exit comparing with smooth profiles. But in case of mode $m = 2$ parabolic profiles, the response is closer to injector.

C.2 Results for constant-density jets, $S = 1$

Next figures show now the spatial response structure for constant density jets with ratio $S = 1$. Figure C.7 represents the forcing and response structures of a jet with Poiseuille outlet velocity profile, $D/\theta_0 = 15$, for the axisymmetric mode, $m = 0$. As previous jets, Reynolds and Strouhal numbers will be $Re = 200$ and $St = 0.3$. It is deduced that the response is contained within a distance of about 60 injector radii, presenting a maximum at an axial position of approximately 15.

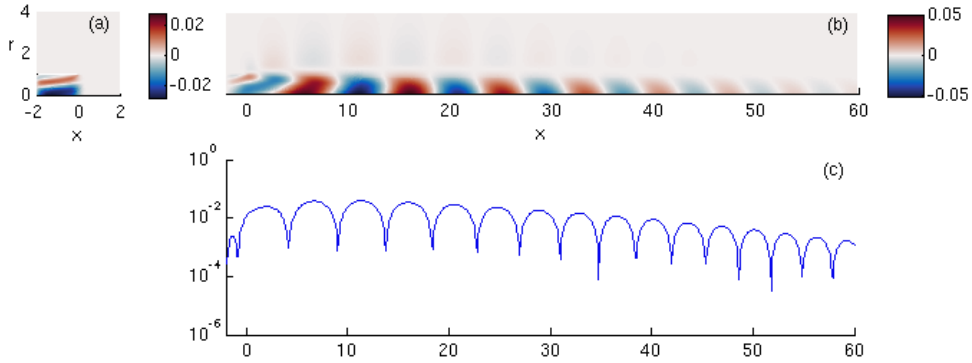

Figure C.7: (a) Contours of optimal forcing, (b) contours of optimal response and (c) optimal response profile at $r = 0.5$, for the axisymmetric mode, $m = 0$, and a jet with $S = 1$, $D/\theta_0 = 15$, $Re = 200$ and $St = 0.3$. The three panels show the amplitude of the axial velocity.

On the other hand, figure C.8 which shows the optimal response for the helical mode $m = \pm 1$ contained within about 80 radii downstream from the injector outlet with a maximum in axial distance at 30 radii.

However, figure C.9 presents the case for mode $m = \pm 2$ whose the optimal response contained within about 20 radii downstream from the injector outlet with a maximum in axial distance at 5 radii.

Figure C.10 which represents the forcing and response structures of a jet with top-hat outlet velocity profile, $D/\theta_0 = 35$, for the axisymmetric mode. It is deduced that the response is contained within a distance of about 50 injector radii, presenting a maximum at an axial position of approximately 15.

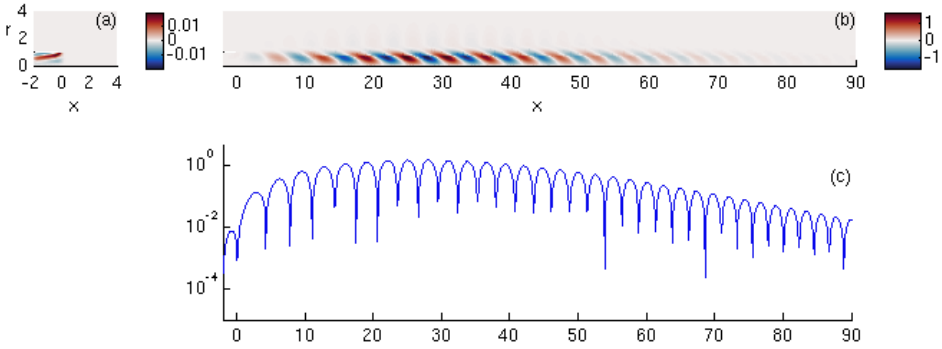

Figure C.8: (a) Contours of optimal forcing, (b) contours of optimal response and (c) optimal response profile at $r = 0.5$, for the axisymmetric mode, $m = \pm 1$, and a jet with $S = 1$, $D/\theta_0 = 15$, $Re = 200$ and $St = 0.3$. The three panels show the amplitude of the axial velocity.

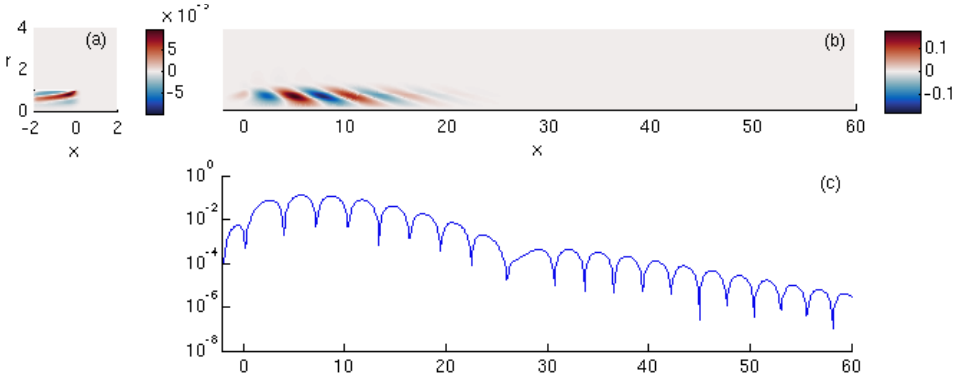

Figure C.9: (a) Contours of optimal forcing, (b) contours of optimal response and (c) optimal response profile at $r = 0.5$, for the axisymmetric mode, $m = \pm 2$, and a jet with $S = 1$, $D/\theta_0 = 15$, $Re = 200$ and $St = 0.3$. The three panels show the amplitude of the axial velocity.

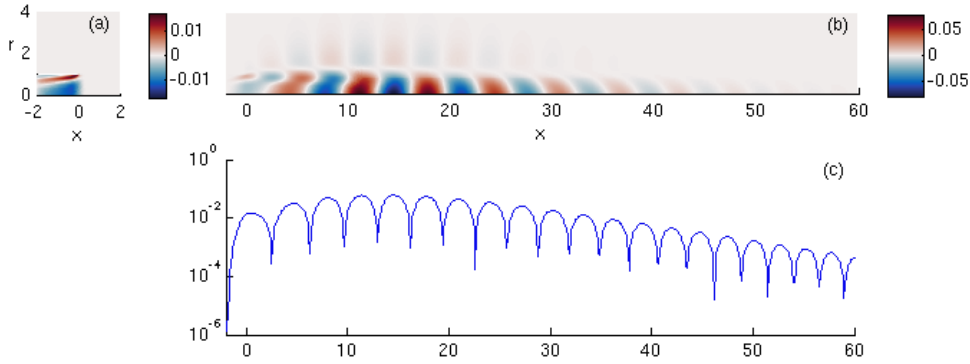

Figure C.10: (a) Contours of optimal forcing, (b) contours of optimal response and (c) optimal response profile at $r = 0.5$, for the axisymmetric mode, $m = 0$, and a jet with $S = 1$, $D/\theta_0 = 35$, $Re = 200$ and $St = 0.3$. The three panels show the amplitude of the axial velocity.

On contrary, figure C.11 shows the optimal response for the helical mode $m = \pm 1$ contained within about 60 radii downstream from the injector outlet with a maximum in axial distance at 25 radii.

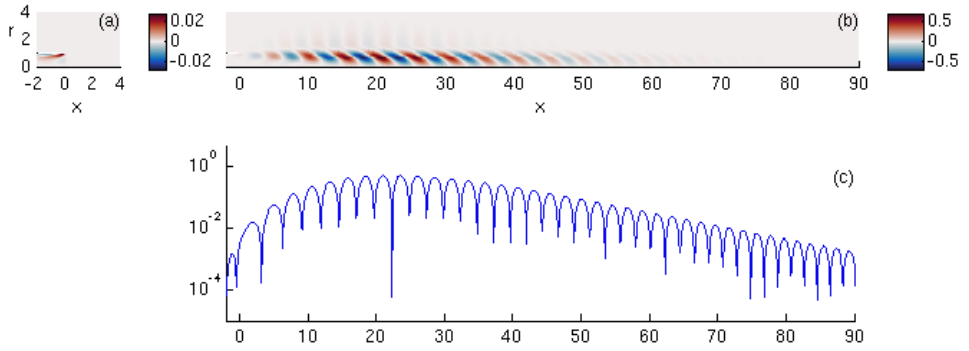

Figure C.11: (a) Contours of optimal forcing, (b) contours of optimal response and (c) optimal response profile at $r = 0.5$, for the axisymmetric mode, $m = \pm 1$, and a jet with $S = 1$, $D/\theta_0 = 35$, $Re = 200$ and $St = 0.3$. The three panels show the amplitude of the axial velocity.

And finally, figure C.12 presents the optimal response for mode $m = \pm 2$ contained within about 25 radii downstream from the injector outlet with a maximum in axial distance at 10 radii.

As mixed jet ($S = 0.5$) has already showed, helical modes presented the response structure concentrated in radial direction close to shear layer at $r = 1R$ and mode $m = 0$ close to the axis.

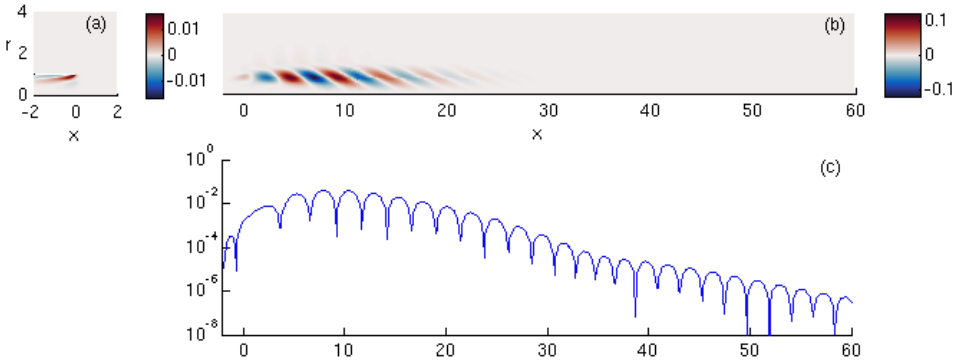

Figure C.12: (a) Contours of optimal forcing, (b) contours of optimal response and (c) optimal response profile at $r = 0.5$, for the axisymmetric mode, $m = \pm 2$, and a jet with $S = 1$, $D/\theta_0 = 35$, $Re = 200$ and $St = 0.3$. The three panels show the amplitude of the axial velocity.

Comparing smooth $D/\theta_0 = 15$ and top-hat kind $D/\theta_0 = 35$ profiles modes $m = 0$ and $m = \pm 1$ find the maximum and they are contained closer to the nozzle exit for top-hat ones. But in case of mode $m = \pm 2$ parabolic profiles the response is closer to injector.

Alphabetical list of references

AMESTOY, P.R., DUFF, I.S. & L'EXCELLENT, J.-Y. 2000 Multifrontal parallel distributed symmetric and unsymmetric solvers. *Computer Methods in Applied Mechanics and Engineering* **184** (2), 501 – 520.

ANDERSON, D. A., TANNEHILL, J. C. & PLETCHER, R. H. 1984 *Computational Fluid Mechanics and Heat Transfer*. Hemisphere, New York.

BAGHERI, S., HENNINGSON, D., HOEPFFNER, J. & SCHMID, P. 2009 Input-output analysis and control design applied to a linear model of spatially developing flows. *Applied Mechanics Reviews* **62**.

BARKLEY, D 2006 Linear analysis of the cylinder wake mean flow. *EPL (Europhysics Letters)* **75** (5), 750.

BATCHELOR, G. K. & GILL, A. E. 1962 Analysis of the stability of axisymmetric jets. *J. Fluid Mech.* **14**, 529–551.

BATTLES, ZACHARY & TREFETHEN, LLOYD N. 2004 An Extension of MATLAB to Continuous Functions and Operators. *SIAM Journal on Scientific Computing* **25** (5), 1743–1770.

BECKER, H. A. & MASSARO, T. A. 1968 Vortex evolution in a round jet. *Journal of Fluid Mechanics* **31** (3), 435–448.

BEN-ISRAEL, ADI 1966 A newton-raphson method for the solution of systems of equations. *Journal of Mathematical Analysis and Applications* **15** (2), 243 – 252.

BHATTACHARYYA, D & GAUVIN, WH 1975 Modeling of heterogeneous systems in a plasma jet reactor. *AIChE Journal* **21** (5), 879–885.

BÉNARD, H 1908 Formation périodique de centres de giration à l'arriére d'un obstacle en mouvement. *C. R. Acad. Sci.* (147), 839.

BREIDENTHAL, R. E. 1984 Structure and mixing of a transverse jet in incompressible flow. *Journal of Fluid Mechanics* **148**, 405–412.

BRIGGS, RICHARD J 1964 Electron-stream interaction with plasmas .

BROWN, GARRY L. & ROSHKO, ANATOL 1974 On density effects and large structure in turbulent mixing layers. *Journal of Fluid Mechanics* **64** (4), 775–816.

CARRARA, M.D. 2001 Hydrodynamic stability of periodically unsteady axisymmetric and swirling jets. *Faculty of the Virginia Polytechnic Institute* .

CHEN, T. S. & TZUOO, K. L. 1982 Vortex Instability of Free Convection Flow Over Horizontal and Inclined Surfaces. *J. Heat Transfer-ASME* **104**, 637–643.

CHOMAZ, JEAN-MARC 2005 Global instabilities in spatially developing flows: Non-Normality and Nonlinearity. *Annual Review of Fluid Mechanics* **37** (1), 357–392.

CHOMAZ, J. M., HUERRE, P. & REDEKOPP, L. G. 1988 Bifurcation to local and global modes in spatially developing flows. *Phys. Rev. Lett.* **60**, 25–.

CHUN, D. H. & SCHWARZ, W. H. 1967 Stability of the Plane Incompressible Viscous Wall Jet Subjected to Small Disturbances. *Physics of Fluids* **10** (5), 911.

CLARKE, J. F. & RILEY, N. 1976 Free convection and the burning of a horizontal fuel surface. *Journal of Fluid Mechanics* **74** (3), 415–431.

COENEN, W. 2010 Absolute instability in the near field of low-density jets. *Universidad Carlos III de Madrid* .

COENEN, W., LESSHAFFT, L., GARNAUD, X. & SEVILLA, A. 2017 Global instability of low-density jets. *J. Fluid Mech.* **820**, 187:207.

COENEN, W. & SEVILLA, A. 2012 The structure of the absolutely unstable regions in the near eld of low-density jets. *J. Fluid Mech.* **713**, 123–149.

COENEN, W., SEVILLA, A. & SÁNCHEZ, A. 2008 Absolute instability of light jets emerging from circular injector tubes. *Phys. Fluids* **20**, 074104.

COHEN, J. 1987 The evolution of instabilities in the axisymmetric jet. part 1. the linear growth of disturbances near the nozzle. *Journal of Fluid Mechanics* **176** (1987), 191–219.

COURANT, R., FRIEDRICHS, K. & LEWY, H. 1928 Über die partiellen differenzengleichungen der mathematischen physik. *Mathematische Annalen* **100** (1), 32–74.

CRABTREE, LF, KUCHEMANN, D & SOWERBY, L 1963 Three-dimensional boundary layers. *Laminar Boundary Layers* pp. 430–432.

CRIGHTON, D. G. & GASTER, M. 1976 Stability of slowly diverging jet flow. *Journal of Fluid Mechanics* **77** (2), 397–413.

CROW, S. C. & CHAMPAGNE, F. H. 1971 Orderly structure in jet turbulence. *Journal of Fluid Mechanics* **48** (3), 547–591.

DANAILA, IONUT, DUŠEK, JAN & ANSELMET, FABIEN 1997 Coherent structures in a round, spatially evolving, unforced, homogeneous jet at low Reynolds numbers. *Physics of Fluids* **9** (11), 3323–3342.

DARRIEUS, G 1938 Propagation d'un front de flamme. *La Technique Moderne* **30**, 18.

DEISSLER, R. J. 1987 The convective nature of instability in plane Poiseuille flow. *Phys. Fluids* **30** (8), 2303–2305.

DOYLE, JAMES D & SHAPIRO, MELVYN A 1999 Flow response to large-scale topography: The greenland tip jet. *Tellus A: Dynamic Meteorology and Oceanography* **51** (5), 728–748.

DRAZIN & REID 1981 Hydrodynamic stability.

DRAZIN, PHILIP G & REID, WILLIAM HILL 2004 *Hydrodynamic stability*. Cambridge university press.

DRYDEN, HUGH L 1947 Some recent contributions to the study of transition and turbulent boundary layers .

EAGLES, P. M. & WEISSMAN, M. A. 1975 On the stability of slowly varying flow: The divergent channel. *Journal of Fluid Mechanics* **69** (2), 241–262.

EMMONS, H. W. 1956 The film combustion of liquid fuel. *ZAMM - Journal of Applied Mathematics and Mechanics / Zeitschrift für Angewandte Mathematik und Mechanik* **36**.

FARADAY, MICHAEL 1861 The Chemical History of a Candle. *A course of lectures delivered before a juvenile audience at the Royal Institution* pp. 194–196.

FINNEY, MARK A., COHEN, JACK D., FORTHOFER, JASON M., MCALLISTER, SARA S., GOLLNER, MICHAEL J., GORHAM, DANIEL J., SAITO, KOZO, AKAFUAH, NELSON K., ADAM, BRITTANY A. & ENGLISH, JUSTIN D. 2015 Role of buoyant flame dynamics in wildfire spread. *Proceedings of the National Academy of Sciences* **112** (32), 9833–9838.

FLANNIGAN, M. D., AMIRO, B. D., LOGAN, K. A., STOCKS, B. J. & WOTTON, B. M. 2006 Forest fires and climate change in the 21st century. *Mitigation and Adaptation Strategies for Global Change* **11** (4), 847–859.

FOGLER, H. SCOTT 2006 *Elements of Reaction Engineering*. Prentice-Hall International London.

GARDINER, WILLIAM CECIL 2000 *Gas-phase combustion chemistry*. Springer New York.

GARNAUD, X., LESSHAFFT, L., SCHMID, P.J. & HUERRE, P. 2013 Modal and transient dynamics of jet flows. *Phys. Fluids* **25** (4), 044103.

GODWIN, PARKE 1844 *A popular view of the doctrines of Charles Fourier*. JS Redfield.

GOLDSTEIN, M EO 1985 Scattering of acoustic waves into tollmien-schlichting waves by small streamwise variations in surface geometry. *Journal of Fluid Mechanics* **154**, 509–529.

GOLLNER, MICHAEL J., SÁNCHEZ, ANTONIO L. & WILLIAMS, FORMAN A. 2013 On the heat transferred to the air surrounding a semi-infinite inclined hot plate. *Journal of Fluid Mechanics* **732**, 304–315.

GORTLER, HENRY 1954 On the three-dimensional instability of laminar boundary layers on concave walls .

HAALAND, S.E. & SPARROW, E.M. 1973*a* Vortex instability of natural convection flow on inclined surfaces. *International Journal of Heat and Mass Transfer* **16** (12), 2355 – 2367.

HAALAND, S. E. & SPARROW, E. M. 1973*b* Wave instability of natural convection on inclined surfaces accounting for nonparallelism of the basic flow. *Journal of Heat Transfer* **95**.

HALL, PHILIP 1983 The linear development of görtler vortices in growing boundary layers. *Journal of Fluid Mechanics* **130**, 41–58.

HALLBERG, M. P., SRINIVASAN, V., GORSE, P. & STRYKOWSKI, P. J. 2007 Suppression of global modes in low-density axisymmetric jets using coflow. *Phys. Fluids* **19** (1), 014102.

HALLBERG, M. P. & STRYKOWSKI, P. J. 2006 On the universality of global modes in low-density axisymmetric jets. *J. Fluid Mech.* **569**, 493–507.

HECHT, FRÉDÉRIC 2012 New development in freefem++. *Journal of numerical mathematics* **20** (3-4), 251–266.

VON HELMHOLTZ, HERMANN L F 1868 Discontinuirliche flüssigkeits-bewegungen .

HIRSCHFELDER, JOSEPH OAKLAND, BIRD, ROBERT BYRON & CURTISS, CHARLES FRANCIS 1954 *Molecular theory of gases and liquids*. John Wiley.

HOLMES, M. H. 2007 *Introduction to Numerical Methods in Differential Equations*. Springer, New York.

HUERRE, P. & MONKEWITZ, P. A. 1985 Absolute and convective instabilities in free shear layers. *J. Fluid Mech.* **159**, 151–168.

HUERRE, P. & MONKEWITZ, P. A. 1990 Local and global instabilities in spatially developing flows. *Annu. Rev. Fluid Mech.* **22**, 473–537.

HWANG, G J & CHENG, K C 1973 Thermal instability of laminar natural convection flow on inclined isothermal plates. *The Canadian Journal of Chemical Engineering* **51** (6), 659–666.

ITO, R. & SENO, T. 1979 Effect of exit geometry on jet behavior. *J. Chem. Eng. Jpn.* **12** (6), 430–435.

IYER, P. A. & KELLY, R. E. 1974 The stability of the laminar free convection flow induced by a heated inclined plate. *International Journal of Heat and Mass Transfer* **17** (4), 517–525.

JACKSON, C. P. 1987 A finite-element study of the onset of vortex shedding in flow past variously shaped bodies. *Journal of Fluid Mechanics* **182**, 23–45.

JENDOUBI, S. & STRYKOWSKI, P. J. 1994 Absolute and convective instability of axisymmetric jets with external flow. *Phys. Fluids* **6**, 3000–3009.

JONES, D R 1973 Free convection from a semi-infinite flat plate inclined at a small angle to the horizontal. *The Quarterly Journal of Mechanics and Applied Mathematics* **26** (1), 77–98.

JUNIPER, M. P. 2007 The full impulse response of two-dimensional jet/wake flows and implications for confinement. *J. Fluid Mech.* **590**, 163–185.

JUNIPER, M. P. 2008 The effect of confinement on the stability of non-swirling round jet/wake flows. *J. Fluid Mech.* **605**, 227–252.

KAHAWITA, RENÉ A. & MERONEY, ROBERT N. 1974 The vortex mode of instability in natural convection flow along inclined plates. *International Journal of Heat and Mass Transfer* **17** (5), 541–548.

KAMBE, TUTOMU 1969 The stability of an axisymmetric jet with parabolic profile. *Journal of the Physical Society of Japan* **26** (2), 566–575.

KHALIGHI, YASER, HAM, FRANK, NICHOLS, JOSEPH, LELE, SANJIVA & MOIN, PARVIZ 2011 Unstructured large eddy simulations for prediction of noise issued from turbulent jets in various configurations p. 2886.

KHORRAMI, MEHDI R, MALIK, MUJEEB R & ASH, ROBERT L 1989 Application of spectral collocation techniques to the stability of swirling flows. *Journal of Computational Physics* **81**.

KIM, J.S., DE RIS, J. & KROESSER, F. W. 1971 Laminar free-convective burning of fuel surfaces. *Symposium (International) on Combustion:* **13**.

KUO, KENNETH K 2005 *Principles of Combustion*.

KWON, SEOK JAE & SEO, IL WON 2005 Reynolds number effects on the behavior of a non-buoyant round jet. *Experiments in Fluids* **38** (6), 801–812.

KYLE, D. M. & SREENIVASAN, K. R. 1993 The instability and breakdown of a round variable-density jet. *J. Fluid Mech.* **249**, 619–664.

LANCZOS, CORNELIUS 1996 *Linear differential operators*. SIAM.

LANDAU, LD 1944 On the theory of slow combustion. *Acta physicochim. URSS* **19** (1), 77–85.

LANDAU, L. & LIFSCHITZ, E. M. 1959 *Fluid Mechanics*. London: Pergamon.

LECONTE, JOHN 1858 On the influence of musical sounds on the flame of a jet of coal-gas. *Philosophical Magazine* **15** (99), 235–239.

LEHOUCQ, RICHARD B, SORENSEN, DANNY C & YANG, CHAO 1998 *ARPACK users' guide: solution of large-scale eigenvalue problems with implicitly restarted Arnoldi methods*, , vol. 6. Siam.

LESSEN, MARTIN & SINGH, PAWAN JIT 1973 The stability of axisymmetric free shear layers. *Journal of Fluid Mechanics* **60** (3), 433–457.

LESSHAFFT, L. & HUERRE, P. 2007 Linear impulse response in hot round jets. *Phys. Fluids* **19** (2), 024102.

LESSHAFFT, L., HUERRE, P. & SAGAUT, P. 2007 Frequency selection in globally unstable round jets. *Phys. Fluids* **19** (5), 054108.

LESSHAFFT, L., HUERRE, P., SAGAUT, P. & TERRACOL, M. 2006 Nonlinear global modes in hot jets. *J. Fluid Mech.* **554**, 393–409.

LESSHAFFT, LUTZ & MARQUET, OLIVIER 2010 Optimal velocity and density profiles for the onset of absolute instability in jets. *Journal of Fluid Mechanics* **662**, 398–408.

LIÑÁN, A., MARTÍNEZ-RUIZ, D., VERA, M. & SÁNCHEZ, A. L. 2017 The large-activation-energy analysis of extinction of counterflow diffusion flames with non-unity lewis numbers of the fuel. *CF* **175**, 91–106.

LIDE, DAVID R 2001 Crc handbook of physics and chemistry. *CRC Press, Boca Raton, USA* **76**, 1995–1996.

LIÑÁN, AMABLE, VERA, MARCOS & SÁNCHEZ, ANTONIO L. 2015 Ignition, Liftoff, and Extinction of Gaseous Diffusion Flames. *Annual Review of Fluid Mechanics* **47** (1), 293–314.

LLOYD, JR & SPARROW, EM 1970 On the instability of natural convection flow on inclined plates. *Journal of Fluid Mechanics* **42** (3), 465–470.

MALLARD, ERNEST & LE CHATELIER, HENRI 1883 *Recherches expérimentales et théoriques sur la combustion des mélanges gazeux explosives*. H. Dunod et E. Pinat.

MATALON, MOSHE 2007 Intrinsic Flame Instabilities in Premixed and Nonpremixed Combustion. *Annual Review of Fluid Mechanics* **39** (1), 163–191.

MATTINGLY, G. E. & CHANG, C. C. 1974 Unstable waves on an axisymmetric jet column. *Journal of Fluid Mechanics* **65** (3), 541–560.

MATVEEV, IGOR, MATVEEVA, SVETLANA & GUTSOL, ALEXANDER 2005 Non-equilibrium plasma igniters and pilots for aerospace application. In *43rd AIAA Aerospace Sciences Meeting and Exhibit*, p. 1191.

MELIGA, P., SIPP, D. & CHOMAZ, J.-M. 2008 Absolute instability in axisymmetric wakes: compressible and density variation effects. *J. Fluid Mech.* **600**, 373–401.

MENDEZ, S., SHOEYBI, M., SHARMA, A., LELE, K. & MOIN, P. 2009 Post-processing of large-eddy simulations for jet noise predictions. *Center for Turbulence Research* .

MICHALKE, ALFONS 1970 A note on the spatial jet-instability of the compressible cylindrical vortex sheet. *Tech. Rep.*. Deutsche Forschungs-und Versuchsanstalt für Luft- und Raumfahrt.

MICHALKE, ALFONS 1984 Survey on jet instability theory. *Progress in Aerospace Sciences* **21**, 159–199.

MILLER, COLIN H., TANG, WEI, FINNEY, MARK A., MCALLISTER, SARA S., FORTHOFER, JASON M. & GOLLNER, MICHAEL J. 2017 An investigation of coherent structures in laminar boundary layer flames. *Combustion and Flame* **181**, 123–135.

MOLLENDORF, J. C. & GEBHART, B. 1973 An experimental and numerical study of the viscous stability of a round laminar vertical jet with and without thermal buoyancy for symmetric and asymmetric disturbances. *Journal of Fluid Mechanics* **61** (2), 367–399.

MONKEWITZ, PETER A. 1996 Modeling of self-excited wake oscillations by amplitude equationsz. *Experimental Thermal and Fluid Science* **12** (2), 175–183.

MONKEWITZ, P. A., BECHERT, D. W., BARSIKOW, B. & LEHMANN, B. 1990 Self-excited oscillations and mixing in a heated round jet. *J. Fluid Mech.* **213**, 611–639.

MONKEWITZ, P. A. & HUERRE, P. 1982 Influence of the velocity ratio on the spatial instability of mixing layer. *Phys. Fluids* **25**, 1137–1143.

MONKEWITZ, PETER A, HUERRE, PATRICK & CHOMAZ, JEAN-MARC 1993 Global linear stability analysis of weakly non-parallel shear flows. *Journal of Fluid Mechanics* **251**, 1–20.

MONKEWITZ, PETER A. & SOHN, KIHOD. 1988 Absolute instability in hot jets. *AIAA Journal* **26** (8), 911–916.

MORENO-BOZA, DANIEL, COENEN, WILFRIED, CARPIO, JAIME, SÁNCHEZ, ANTONIO L. & WILLIAMS, FORMAN A. 2018 On the critical conditions for pool-fire puffing. *Combustion and Flame* **192**, 426 – 438.

MORRIS, PHILIP J. 1976 The spatial viscous instability of axisymmetric jets. *Journal of Fluid Mechanics* **77** (3), 511–529.

NICHOLS, J & LELE, S 2010 Global mode analysis of turbulent high-speed jets. *Annual Research Briefs* .

NICHOLS, J. W., SCHMID, P. J. & RILEY, J. J. 2007 Self-sustained oscillations in variable-density round jets. *J. Fluid Mech.* **582**, 341–376.

OPPENHEIM, A. & WILLSKY, A. 1998 *Signals and Systems*. Prentice Hall.

OPPENHEIM, A K & I, SOLOUKHIN R 1973 Experiments in gasdynamics of explosions. *Annual Review of Fluid Mechanics* **5** (1), 31–58.

PAI, SI 1951 On the stability of two-dimensional laminar jet flow of gas. *Journal of the Aeronautical Sciences* **18** (11), 731–742.

PERA, LUCIANO & GEBHART, BENJAMIN 1973*a* Natural convection boundary layer flow over horizontal and slightly inclined surfaces. *International Journal of Heat and Mass Transfer* **16** (6), 1131–1146.

PERA, LUCIANO & GEBHART, BENJAMIN 1973*b* On the stability of natural convection boundary layer flow over horizontal and slightly inclined surfaces. *International Journal of Heat and Mass Transfer* **16** (6), 1147–1163.

PETERSEN, RUSSELL E. & EMMONS, HOWARD W. 1961 Stability of Laminar Flames. *Physics of Fluids* **4** (4), 456.

PICKART, ROBERT S, SPALL, MICHAEL A, RIBERGAARD, MADS HVID, MOORE, GWK & MILLIFF, RALPH F 2003 Deep convection in the irminger sea forced by the greenland tip jet. *Nature* **424** (6945), 152.

PROVANSAL, M, MATHIS, C & BOYER, L 1987 Bénard-von kármán instability: transient and forced regimes. *Journal of Fluid Mechanics* **182**, 1–22.

QADRI, UBAID ALI & SCHMID, PETER J. 2017 Effect of nonlinearities on the frequency response of a round jet. *Physical Review Fluids* **2** (4), 1–14.

RAJAMANICKAM, PRABAKARAN, COENEN, WILFRIED & SÁNCHEZ, ANTONIO L. 2017 Non-Boussinesq stability analysis of natural-convection gaseous flow on inclined hot plates. *International Journal of Heat and Mass Transfer* **109**, 949–957.

RAVIER, S., ABID, M., AMIELH, M. & ANSELMET, F. 2006 Direct numerical simulation of variable-density plane jets. *J. Fluid Mech.* **546**, 153–191.

RAYLEIGH, LORD 1879 On the stability, or instability, of certain fluid motions. *Proceedings of the London Mathematical Society* **s1-11** (1), 57–72.

RAYNAL, L., J.-L., HARION, FAVRE-MARINET, M. & BINDER, G. 1996 The oscillatory instability of plane variable-density jets. *Phys. Fluids* **8**, 993–1006.

REYNOLDS, A J 1962 Observations of a liquid-into-liquid jet. *Journal of Fluid Mechanics* **14** (4), 552–556.

ROTEM, ZEEV & CLAASSEN, LUTZ 1969 Natural convection above unconfined horizontal surfaces. *Journal of Fluid Mechanics* **39** (1), 173–192.

SÁNCHEZ, ANTONIO L, LIÑÁN, AMABLE & WILLIAMS, FORMAN A 1997 A generalized burke-schumann formulation for hydrogen-oxygen diffusion flames maintaining partial equilibrium of the shuffle reactions. *Combustion science and technology* **123** (1-6), 317–345.

SÁNCHEZ-SANZ, M., ROSALES, M. & SÁNCHEZ, A.L. 2010 The hydrogen laminar jet. *Int. J. Hydrogen Energy* **35**, 3919–3927.

SÁNCHEZ-SANZ, M., SÁNCHEZ, A.L. & LIÑÁN, A. 2006 Fronts in high-temperature laminar gas jets. *J. Fluid Mech.* **547**, 257–266.

SCHMIDT, ERNST & BECKMANN, WILHELM 1930 Das temperatur-und geschwindigkeitsfeld vor einer wärme abgebenden senkrechten platte bei natürlicher konvektion. *Technische Mechanik und Thermodynamik* **1** (11), 391–406.

SCHUBAUER, GB 1947 Laminar boundary-layer oscillations and stability of laminar flow. *Journal of the Aeronautical Sciences* **14** (2), 69–78.

SEVILLA, A., GORDILLO, J. M. & MARTÍNEZ-BAZÁN, C. 2002 The effect of the diameter ratio on the absolute and convective instability of free coflowing jets. *Phys. Fluids* **14**, 3028–3038.

SEVILLA, A. & MARTÍNEZ-BAZÁN, C. 2004 Vortex shedding in high Reynolds number axisymmetric bluff-body wakes: Local linear instability and global bleed control. *Phys. Fluids* **16**, 3460.

SEVILLA, A. & MARTÍNEZ-BAZÁN, C. 2006 A note on the stabilization of bluff-body wakes by low density base bleed. *Phys. Fluids* **18**, 098102.

SIPP, DENIS & MARQUET, OLIVIER 2013 Characterization of noise amplifiers with global singular modes: The case of the leading-edge flat-plate boundary layer. *Theoretical and Computational Fluid Dynamics* **27** (5), 617–635.

SIVASHINSKY, G I 1983 Instabilities, Pattern Formation, and Turbulence in Flames. *Annual Review of Fluid Mechanics* **15** (1), 179–199.

SODERBERG, D. 1999 Hydrodynamics of plane liquid jets aimed at applications in paper manufacturing. *Royal Institute of Technology Stockholm, Sweden* .

SPARROW, EM & HUSAR, RB 1969 Longitudinal vortices in natural convection flow on inclined plates. *Journal of Fluid Mechanics* **37** (2), 251–255.

SREENIVASAN, KR, STRYKOWSKI, PJ & OLINGER, DJ 1987*a* Hopf bifurcation, landau equation, and vortex shedding behind circular cylinders. In *Forum on unsteady flow*

separation, , vol. 1, pp. 1–13. American Society for Mechanical Engineers, Fluids Engineering Division New York.

SREENIVASAN, K. R., RAGHU, S. & KYLE, D. 1989 Absolute instability in variable density round jets. *Exps. Fluids* **7**, 309–317.

SREENIVASAN, K. R., STRYKOWSKI, P. J. & OLINGER, D. J. 1987*b* Hopf bifurcation, Landau equation, and vortex shedding behind circular cylinders.

SRINIVASAN, K., HALLBERG, M. P. & STRYKOWSKI, P. J. 2010 Viscous linear stability of axisymmetric low-density jets: Parameters influencing absolute instability. *Phys. Fluids* **22**, 024103.

STEWARTSON, K. 1974 Multistructured Boundary Layers on Flat Plates and Related Bodies. *Advances in Applied Mechanics* **14** (C), 145–239.

STRYKOWSKI, P. J. & NICCUM, D. L. 1991 The stability of countercurrent mixing layers in circular jets. *Journal of Fluid Mechanics* **227**, 309–343.

TATSUMI, T. & KAKUTANI, T. 1958 The stability of a two dimensional laminar jet .

THEOFILIS, VASSILIOS 2011 Global Linear Instability. *Annual Review of Fluid Mechanics* **43** (1), 319–352.

TREFETHEN, LLOYD N 2013 *Approximation theory and approximation practice*, , vol. 128. Siam.

TREFETHEN, L. N., TREFETHEN, A. E., REDDY, S. C. & DRISCOLL, T. A. 1993 Hydrodynamic Stability Without Eigenvalues. *Science* **261** (5121), 578–584.

TYNDALL, F.R.S. 1867*a* On the action of sonorous vibrations on gaseous and liquid jets. *The London, Edinburgh, and Dublin Philosophical Magazine and Journal of Science* **33** (224), 375–391.

TYNDALL, JOHN 1867*b* On sounding and sensitive flames. *Philosophical Magazine* **33** (221), 92–99.

VIILU, ANDRUS 1962 An Experimental Determination of the Minimum Reynolds Number for Instability in a Free Jet. *J. Appl. Mech.* **29** (5), 506–508.

VON KARMAN, T 1908 Ueber den mechanismus des widerstandes, den ein bewegter körper in einer flüssigkeit erfährt. *Gottingen Nachr. Math. Phys. Kl.* (12), 509.

WILLIAMS, F. A. 1985 Comment. *Combustion Science and Technology* **43** (5-6), 329–332.

YU, M.-H. & MONKEWITZ, P. A. 1990 The effect of nonuniform density on the absolute instability of two-dimensional inertial wakes and jets. *Phys. Fluids A* **2**, 611–639.

YU, M.-H. & MONKEWITZ, P. A. 1993 Oscillations in the near field of a heated two-dimensional jet. *J. Fluid Mech.* **25**, 323–347.

ZAMAN, K. B. M. Q. & SEINER, J. M. 1990 Viscous effects on the instability of an axisymmetric jet. *Tech. Rep.* NASA-TM-102396. NASA Glenn Research Center.

ZEBIB, A. 1987 Stability of viscous flow past a circular cylinder. *Journal of Engineering Mathematics* **21** (2), 155–165.

ZELDOVICH, YA B 1951 On the theory of combustion of initially unmixed gases. *NASA* .

List of Publications

Conference Presentations

1. Gomez-Lendinez, D., Coenen, W., Sevilla, A. (2015) Numerical analysis of the hydrodynamic stability of low-density jets. Workshop in Fluid Mechanics, Jaen, Spain.

2. Gomez-Lendinez, D., Coenen, W., Sanchez, A.L. (2016) Linear stability analysis of Clarke-Riley diffusion flames. American Physical Society: Division of Fluid Dynamics, Portland, USA.

3. Gomez-Lendinez, D., Coenen, W., Sevilla, A. (2017) Numerical study of the stability of laminar low-density jets. Challenges in Nonlinear Systems: A meeting to celebrate the 60th birthday of Prof. L.L. Bonilla, Madrid, Spain.

4. Gomez-Lendinez, D., Sevilla, A, Coenen, W. (2017) Numerical study of the stability of submerged laminar light jets. Workshop in Fluid Mechanics, Tarragona, Spain.

5. Gomez-Lendínez, D., Almenara-Rescalvo, J., Herranz-Sanz, C., Martinez, J. E., Martin-Fuente, E. (2017) High Downforce devices for Formula Students cars: a numerical study. European Automotive Engineers Conference, Madrid, Spain.

6. Gomez-Lendinez, D., Coenen, W., Sevilla, A. (2017) Direct numerical simulation of axisymmetric laminar low-density jets. American Physical Society: Division of Fluid Dynamics, Denver, USA.

Agradecimientos

Me gustaría acordarme ...

de Wil y Alejandro, por su paciencia infinita conmigo y su gran apoyo durante estos años,

de Antonio, por darme la oportunidad de hacer la estancia en San Diego, y vivir la experiencia allí, y conocer a estupendas personas como Jose, Raquel, Brenda, Adam, Prava, Forman y Amable entre otros,

de Patri y Alejandro, mis compis de despacho por compartir buenos momentos, y mis otros compis como Imma, Eduardo, Javi, Marcos, Mario, Juan, César, Dani, y Dani, Alex, Fer, Desi, Paula, Pablo, Rafa, Marta, Carol, Sergio, Antonio, Alberto, Jesús, Kike, entre otros, por mantener un estupendo ambiente y echar una mano cuando hacía falta,

de Cristina, por facilitar muchísimo el trabajo de todos y todos los días,

de Carlos, Jorge, Olalla, Carrillo, Vega, Cris, Nieves, Vir, Javi y Dani por estar ahí siempre y pasar momentos divertidos juntos durante muchos años,

de Trini, por hacerme feliz y apoyarme en estos últimos meses,

y finalmente, de mis padres, por los años de apoyo, ayuda y cariño que me han dado.

y de muchos otros que no están en esta lista.

Gracias por vuestro apoyo.